Measuring Aerosol Nanoparticles by Ultraviolet Photoionisation

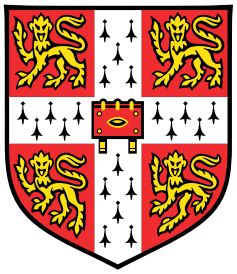

Robert Takeo Nishida

Department of Engineering
University of Cambridge

This dissertation is submitted for the degree of
Doctor of Philosophy

Clare Hall

September 2018

This thesis is dedicated to my mother.

Declaration

I hereby declare that this dissertation is the result of my own work and includes nothing which is the outcome of work done in collaboration except as declared in the Acknowledgements and specified in the text. This dissertation is not substantially the same as any other that I have submitted, or, is being concurrently submitted for any degree, diploma or other qualification at the University of Cambridge or any other University or similar institution. I further state that no substantial part of this dissertation has already been submitted, or, is being concurrently submitted for any degree, diploma or other qualification at the University of Cambridge or any other University or similar institution. This dissertation does not exceed the prescribed word limit.

Robert Takeo Nishida
September 2018

Acknowledgements

I would like to express my sincere gratitude to my supervisor, Prof. Simone Hochgreb, for her steady guidance and contributions to the scientific quality of this work, and my advisor, Dr Adam Boies, for his ideas and inspiration. Their complementary expertise and the stimulating research environment they have created are invaluable to the contributions of this work, my career and my personal development.

I would like to thank John Saffell for his continued and unwavering support of this project. I gratefully acknowledge Alphasense Ltd., Cambridge Trust, Natural Sciences and Engineering Research Council of Canada (NSERC), and the UK Aerosol Society for financial support.

I have had the pleasure of working with academic collaborators at Cambustion Ltd., University of Alberta, TU Graz, Imperial College and the University of Cambridge and I thank them for sharing ideas, expertise and equipment in the spirit of academic advancement. In particular, I thank Tyler Johnson for sharing his extensive experimental expertise. I look forward to further collaborations.

I would like to acknowledge the departmental and divisional staff including the electronics and machine shops for their support and expertise, particularly Mick Underwood and Peter Benie for their exemplary technical skill. Many thanks to the members of Clare Hall for creating an enriching academic environment.

I am grateful for the efforts of project students Rebecca Baker, Greg Ghahramani, Nene Yamasaki, Xi Shern Tan, Robin Platts, Glen Chua, and Rory Geeson, from each of whom I learned something new. I would like to thank my friends and colleagues Marc, Christian, Richard, Jean, Brian, Tyler and Mario for valuable discussions both in the lab and enriching experiences outside.

I thank my family for their enduring love and support and for valuing education; especially my mother, Carol, who I miss dearly. Finally, I thank my wife, Rachel, and daughter, Lillian, for, above all, bringing me great joy.

Abstract

Aerosol particulate matter adversely affects the climate, environment and human health. Mechanistic studies have indicated that ultrafine aerosol nanoparticles, those under 100 nm in diameter, may have significant health impacts due to their relatively high number concentration, surface area and potential for deep penetration into the human lung. However, epidemiological evidence remains limited due to the lack of measurement networks that monitor local concentrations of ultrafine particles.

Direct ultraviolet (UV) photoionisation electrically charges aerosol nanoparticles for subsequent detection by a mechanism distinct from the ion-particle collisions of conventional methods. The aim of this work is to evaluate photoionisation theory in order to understand and interpret measurements from a low-cost aerosol particle sensor. To accomplish this, theoretical equations are analysed, modelled and compared with experimental results for validation. The photoelectric yield of aerosol particles is explored in terms of particle size, concentration, material, and morphology giving insight into the interaction of light and particles.

This thesis introduces the first analysis of photoionisation, recombination, convection/diffusion and transport of particles in an electric field using analytical, numerical, and computational fluid dynamics (CFD) techniques. Characteristic times and dimensionless parameters are defined to determine regimes under which the measurement system is dominated by each of the charging or transport mechanisms. The level of modelling detail required for accurate prediction of aerosol charging and capture methods is demonstrated over a range of conditions.

In a continuous flow of aerosol particles, an electric field is applied to capture charge as it is photoemitted from particles and before the emitted charge and particles can recombine. This method yields a novel current measurement directly representative of photoemission. The CFD model agrees well with electrical current measurements demonstrating that the physics of the problem is suitably represented. It is demonstrated that photoemission is linearly proportional to total (mobility) surface area for a large range of sizes and concentrations of particles of self-similar material and morphology, with agglomerated silver particles having $5\times$ yield of agglomerated carbon from a propane flame. It is shown for the first time that

agglomerated particles have a significantly higher photoelectric yield (2.6×) than sintered, close-packed spheres of the same mobility diameter and material, directly contradicting two of the three previous relevant studies. Close-packed spheres have less material exposed to both the photon flux and the particle's surroundings than an agglomerate of the same particle mobility diameter, thereby reducing photoelectric activity. The photoelectrically active area is defined explicitly in this work to reflect the effect of a particle's morphology; the revised definition produces good agreement with experimental results.

Table of contents

List of figures

List of tables

Nomenclature

Roman Symbols

A	surface area concentration, $nm^2\ cm^{-3}$; dimensionless effect of recombination
a	ion-ion collision coefficient, $cm^3\ s^{-1}$
D_α	agglomerate structure power law exponent
B	mobility, $s\ kg^{-1}$; dimensionless effect of diffusion loss
C	dimensionless effect of E-field loss
c	mean molecular velocity, $m\ s^{-1}$; operation constant
C_c	Cunningham slip correction factor
D	diffusion coefficient, $m^2\ s^{-1}$
d	particle diameter, nm
e	electron charge, 1.602×10^{-19} C
$\vec{E}$	electric field, $V\ m^{-1}$
$f(d)$	probability distribution function
h	Planck's constant, $6.626068 \times 10^{-34}\ kg\ m^2\ s^{-1}$
$h\nu$	specific photon energy, eV
I	radiative energy flux, $W\ m^{-2}$
i	current, A; number and polarity of particle charges
K	particle conductivity parameter
k_a	agglomerate structure pre-exponential term
k_B	Boltzmann constant, $1.38\times10^{-23}\ m^2\ kg\ s^{-2}\ K^{-1}$
K_c	photoemission constant, J^{-2}
L	length of irradiated region, m

m	mass, kg; empirically determined constant
N	particle number concentration, cm^{-3}
n	ion concentration, cm^{-3}
p	pressure, Pa
Q	volumetric flow rate, std L/min
q	particle charge level
R	tube radius, m
r	distance from particle centre, m
S	ion/particle source/sink term, $m^{-3}\ s^{-1}$; shape factor
T	temperature, K
t	time, s
U	bulk flow speed, $m\ s^{-1}$
$\vec{u}$	velocity, $m\ s^{-1}$
ν	photon frequency, s^{-1}
V	chamber volume, m^3, voltage, V
V_e	elementary electron potential
Y	quantum yield per incident photon
Z	particle electric mobility, $m^2\ V^{-1}\ s^{-1}$

Greek Symbols

$\alpha^{q\rightarrow q+1}$	combination coefficient for photoionisation, s^{-1}
α_C	ion-particle collision probability
β	ion-particle collision coefficient, $cm^3\ s^{-1}$
χ	dynamic shape factor
δ	limiting sphere radius, m; power fit concentration exponent
ε	power fit diameter exponent
ε_0	vacuum dielectric constant $F\ m^{-1}$
γ	power fit pre-factor
μ	gas viscosity, $kg\ m^{-1}\ s^{-1}$
Φ	work function, eV

ϕ	filling factor
ρ	density, kg m^{-3}
ρ_0	unit density, 1000 kg m^{-3}
σ_{ph}	photoelectrically active area
τ	characteristic time, s
ε_0	vacuum dielectric constant, 8.854×10^{-12} F m^{-1}
φ	particle intermolecular potential, V

Superscripts

$\hat{}$	dimensionless parameter
M	number of monodisperse size bins
-	mean

Subscripts

a	aerodynamic
ae	aerodynamic equivalent
α	photoionisation
b	size bin index
β	ion-particle collision
c	convection; cylinder
cl	close-packed
d	diffusional wall loss
e	electrode; electric field; exposed
eff	effective
i	ion
∞	flat surface
irr	irradiation
j	ion charge level
max	maximum
min	minimum
m	mobility

n	number of primary particles
ν	photon
o	outlet
p	particle, photoelectric
ph	photoelectric
pp	primary particle
q	charge level index
r	relaxation; recombination; chamber radius, m
S	source/sink
s	charge saturation; surface
ε	photoelectric activity
va	volume-surface equivalent
V_e	elementary electron potential, eV m
ve	volume equivalent
z	direction of flow

Acronyms / Abbreviations

AAC	Aerodynamic Aerosol Classifier
APM	Aerosol Particle Mass
CFD	Computational Fluid Dynamics
CMD	Count Median Diameter
CPC	Condensation Particle Counter
CPMA	Centrifugal Particle Mass Analyzer
CS	Catalytic Stripper
CSV	Comma Separated Variable
DC	Diffusion Charging; Direct Current
DMA	Differential Mobility Analyzer
DMS	Differential Mobility Spectrometer
DOS	Di-Octyl Sebacate
EEPS	Engine Exhaust Particle Sizer

ELPI	Electrical Low Pressure Impactor
FCE	Faraday Cup Electrometer
FMPS	Fast Mobility Particle Sizer
GB	Gigabytes
HEPA	High Efficiency Particulate Air
LDSA	Lung Deposited Surface Area
MOUDI	Micro-Orifice Uniform Deposit Impactor
NTP	Normal Temperature and Pressure
PAH	Polycyclic Aromatic Hydrocarbon
PAS	Photoelectric Aerosol Sensor
$PM_{2.5}$	Particulate Matter $\leq 2.5\mu$m
PTFE	Polytetrafluoroethylene
RAM	Random Access Memory
SMPS	Scanning Mobility Particle Size Spectrometer
UV	Ultraviolet

Chapter 1

Introduction

1.1 Motivation

Aerosols consist of solid or liquid particles suspended in a gaseous medium [1]. Aerosols can adversely affect the climate [2], environment [3] and human health [4] and are commonly emitted as a by-product of combustion or industrial processes. Aerosol particles may also be engineered for the production of materials with unique properties [5]. The study of aerosols including their behaviour and effects requires accurate characterisation and measurement of a range of particle properties [6].

One of the primary concerns involving aerosols is the direct health impacts from local air pollution [4]. Multiple large-scale air pollution studies have shown a direct relationship between sub-2.5 μm aerosol particulate matter ($PM_{2.5}$) concentrations and all-cause mortality [7, 8]. The World Health Organization International Agency for Research on Cancer has classified outdoor air pollution and particulate matter from outdoor air pollution as a Group I carcinogen [9]. In addition to concerns over the health impacts of $PM_{2.5}$, mechanistic studies have indicated that nanoparticles or ultrafine particles (particles smaller than 100 nm in aerodynamic diameter, which are a subset of $PM_{2.5}$ [10, 6]) may have health impacts beyond $PM_{2.5}$ due to their relatively high number concentration, surface area and potential for deeper penetration into the human lung [11]. Epidemiological evidence remains limited due to the small number of measurement networks that monitor local concentrations of ultrafine particles [10]. Accurate quantification of aerosols is necessary to regulate and control particle emission sources, such as automotive [12] and turbine engine exhaust [13], and air pollution in urban areas [14] and industrial workplaces [15]. Furthermore, the metrics by which aerosols are measured should be representative of the emission source, environmental impacts and/or health impacts depending on the application [16].

Conventional light-scattering methods are only effective for particles in the optically active size range (particles larger than 300 nm diameter) [6]. Existing methods for detection of ultrafines are often prohibitively expensive, require full bench-top systems, have low time resolution, or are accurate only in idealised conditions [17]. A network of low-cost, distributable sensors for ultrafine particles could be used in urban areas or transport centres to carry out source attribution [18, 19], inform policy [20] and provide information for epidemiological studies [10]. Other applications of such sensors include workplace hazard and exposure identification [21] and engine and vehicle emissions monitoring [22].

The physical principles of photoelectric charging and particle transport are explored in this work with the aim of improving the theoretical understanding and the interpretation of measurements. A sensor for aerosol nanoparticles is developed based on the principles explored in this work.

1.2 Background information

1.2.1 Conventional aerosol measurement systems

Conventional measurement systems used for measurements of aerosol nanoparticles commonly involve three stages in a range of configurations which yield information on particle size and number concentration independent of particle chemistry: electrical charge conditioning, particle classification, and particle counting [6]. Particles are electrically charged in the electrical charge conditioning stage in order to be classified and/or counted in the subsequent stages, though the charge conditioning stage is not always necessary. The classification stage selects particles by a characteristic parameter involving a balance of forces on the particle in continuous flow. After classification, the particles are subsequently counted by a particle counter. The measurement systems range in the type of particle information, accuracy and cost.

In this section, the Scanning Mobility Particle Size Spectrometer (SMPS) and Aerodynamic Aerosol Classifier (AAC) are discussed in detail both to demonstrate examples of high-resolution aerosol size measurement systems and to describe the measurement principles, as both devices are used extensively in this work. Low-cost nanoparticle sensors are discussed to provide context for photoelectric charging and charge counting as a method for measuring particles.

Scanning Mobility Particle Sizer (SMPS)

A Scanning Mobility Particle Size Spectrometer (SMPS) is regarded as a standard measurement system to measure size distributions of aerosol particles [23, 24]. It combines a neutraliser, Differential Mobility Analyzer (DMA) and a Condensation Particle Counter (CPC). The charge conditioning stage is made up of a neutraliser which is commonly operated using an alpha or beta radioactive [24] or X-ray ionisation source [6]. The neutraliser first ionises gas molecules into positively and negatively charged gaseous ions, which subsequently transfer charge to the sampled particles by diffusive and electrostatic forces, resulting in a known bipolar charge distribution of positive, negative and neutral particles [25, 26]. If the particles are exposed to a sufficient number of ions within the neutraliser, the particles are charged to known charge states dependent on the particle size, but independent of the particle concentration [24]. In the classifier stage, the charged particles flow between two concentric electrodes making up a DMA column. When an electric field is applied, particles of one polarity pass through a sheath flow, resisted by a drag force, towards a slit at the end of the DMA and are then counted by the CPC. By varying the electric field strength for known sample and sheath flow rates, only particles of a known electrical mobility are classified and therefore counted. The DMA allows the selection of particles by their electrical mobility diameter, d_{m}, defined in Table 1.1. By accounting for the expected charge states from the neutraliser as a function of the classified particle mobility, the mobility size distribution of the polydisperse aerosol may be measured. The CPC uses the particles as nucleation sites for condensing a vapour such as butanol into droplets sufficiently large to be counted by optical methods [6]. The CPC measures the concentration of particles, but cannot distinguish particle size when operating alone. A Faraday Cup Electrometer (FCE) or other electrometry methods may also be used to count charged particles at the outlet of the classifier in the form of an electrical current if the charge states are known [27]. A FCE captures charged particles in a filter and induces a measured electrical current equal to the amount of charge captured in the filter per unit time.

Aerodynamic Aerosol Classifier (AAC)

The Aerodynamic Aerosol Classifier (AAC) selects particles by aerodynamic equivalent diameter or aerodynamic diameter, d_{ae} (Table 1.1), by balancing drag and centrifugal forces independently of electrical charging [28]. The AAC selects particles of a given aerodynamic diameter by inducing a centrifugal force using rotating concentric cylinders, while controlling the particle residence time using a sheath flow. Only particles within a narrow range of selected terminal velocity or particle relaxation time, τ_{r}, follow the correct trajectory to

Table 1.1 Particle diameter definitions and classifiers used for measurement in this work [6].

Symbol	Name	Definition	Classifier
d_{ve}	Volume equivalent diameter	Diameter of a spherical particle of the same volume as the particle under consideration	AAC-DMA
d_{ae}	Aerodynamic equivalent diameter	Diameter of a spherical particle with unit density, $\rho_0 = 1000$ kg m^{-3}, that has the same settling velocity as the particle under consideration	AAC
d_m	Electrical mobility diameter	Diameter of a spherical particle with the same electrical mobility (migration rate in an electric field) as the particle under consideration	DMA

pass through the classifier. The AAC allows the resolution of particle aerodynamic size distributions when used with a particle counter.

Tandem AAC-SMPS

When the AAC is used to classify particles by aerodynamic diameter, d_{ae}, in tandem with other aerosol measurement equipment such as an SMPS system (which quantifies mobility diameter, d_m), other metrics for particle morphology may be measured such as the volume equivalent diameter, d_{ve}, dynamic shape factor, χ, or particle effective density, ρ_{eff}, using the following relationship for equal particle relaxation time, τ_r, [29, 30]

$$\tau_r = m_p B = \frac{C_c(d_{ae})\rho_0 d_{ae}^2}{18\mu} = \frac{C_c(d_m)\rho_{eff} d_m^2}{18\mu} = \frac{C_c(d_{ve})\rho_p d_{ve}^2}{18\mu\chi} \tag{1.1}$$

for particle mass, m_p, mobility, B, gas viscosity, μ, unit density, $\rho_0 = 1000$ kg m^{-3}, and particle material density, ρ_p. The Cunningham slip correction factor, C_c, is a function of the size of the particle under consideration. The effective density, ρ_{eff}, is defined as the density of the particle including voids: $\rho_{eff} = \frac{m_p}{\pi d_m^3/6}$ [30]. Both the AAC and SMPS enable highly resolved measurements of particle properties for detailed particle characterisation and reference measurements for evaluation of other instruments.

Other particle classifiers and sizers

Other measurement systems for mobility size distributions include the EEPS, FMPS [31], and DMS500 [32]. Each of these devices uses a unipolar diffusion charge conditioner which

charges particles with high extrinsic charging efficiency in one polarity. The particles are classified by electrical mobility in an electric field, similar to the DMA. However, they are detected using an array of parallel electrometer detectors. The parallel detection stages enable high time resolution measurements of mobility size distributions. Other aerodynamic diameter measurement systems include the Electrical Low Pressure Impactor (ELPI) [33] or Micro-Orifice Uniform Deposit Impactor (MOUDI) [34] which allows classification of particles by aerodynamic diameter by using a series of impactor stages in which particles with sufficient inertia are deposited on plates by inertial impaction. Particles may be classified by mass-to-charge ratio using, for example, a Centrifugal Particle Mass Analyzer (CPMA) [35] or Aerosol Particle Mass (APM) analyser [36] which balance electrostatic and centrifugal forces, and if the charge state is known, the mass of the particle, m_{p}, may be measured. Details of alternative techniques and other operating principles for measuring aerosols are available in *Aerosol Measurement* [6].

The conventional aerosol measurement systems can yield highly resolved size, concentration, mass, and morphology[1] parameters for a wide range of particle sizes and types. However the devices require large, bench-top systems, high power, long sampling times, complex flow control, high maintenance and/or costly charge conditioners [6, 17]. More recently, smaller, lower cost and portable alternatives which operate on similar principles to conventional methods have gained interest for particle measurements.

Low-cost nanoparticle sensors

Compact, low-cost sensors for environmental or personal exposure monitoring of ultrafine particles combine charging, classification and detection into smaller, sometimes hand-held, devices [37]. The devices each include a charging stage in which aerosol particles acquire discrete charge states. After the charging stage, an ion trap captures highly mobile, excess ions using an electric field and the remaining charged particles are sensed via electrical currents with sensitive electrometers. The conventional classification stage is often removed such that all available particles are charged and measured. Therefore, the devices yield averaged size and concentration measurements rather than resolved size distributions.

Several low-cost sensors use corona discharge to generate ions of one polarity which subsequently transfer charge to particles via diffusional charging [38]. The integrated electrical current resulting from unipolar diffusion charging is linearly dependent on concentration, N, and nearly linearly dependent on particle diameter, d: $i \sim Nd$ for the NanoTracer [39], $i \sim Nd^{1.13}$ for the NSAM [40], and $i \sim Nd^{1.1}$ for the Naneos Partector and DiSCmini [41, 17, 42]. The human lung deposition curve has nearly a d^{-1} dependence [43]

[1] when using measurement systems in tandem or parallel

which, multiplied with a surface area metric d^2, yields what has been described as a lung deposited surface area (LDSA), or the fraction of airborne particle surface area concentration that would deposit in a human lung. Therefore, by applying a calibration constant, each of the low-cost devices measures LDSA by measuring $i \sim Nd^1$ [37].

The NanoTracer and DiSCmini give an additional estimates of size and concentration as well as LDSA. The NanoTracer operates a low-efficiency electrostatic precipitator which alternately captures more electrically mobile particles with a square wave voltage, yielding two signals [37]. In the DiSCmini, there are two consecutive filter stages in which particles are preferentially deposited based on size. In both devices, two signals are used to derive mean particle size and concentration, assuming a standard deviation of a lognormal distribution [41].

Alternative low-cost photoelectric charging devices ionise particles directly with ultraviolet (UV) light rather than by diffusional charging. Ions emitted during the photoionisation process are captured in an ion trap and the remaining positively charged particles are collected on a filter and measured using a Faraday cup electrometer. The Photoelectric Aerosol Sensor (PAS) was developed using these principles and was originally intended to selectively measure the masses of polycyclic aromatic hydrocarbons (PAH) [44]. Site-specific calibration can be used to quantify amounts of photoelectrically active particles. Measurements from PAS sensors are often correlated with carbon mass [45], inverse of particle mobility [46–49], or total mobility surface area [50, 22, 51] and the true metric of particle measurement resulting from photoelectric charging and charge capture is not well defined.

1.2.2 Charging mechanisms

In all of the low-cost devices and most of the high resolution measurement systems, it is necessary to electrically charge the particles for classification and/or detection. The advantage of bipolar charging techniques is that a well defined charge equilibrium can be established even for different ion sources allowing accurate measurements of particle size distributions [52]. The cost and practicality of conventional neutraliser ionisation sources (e.g. radioactive and soft X-ray) makes them less desirable for low-cost sensors [6]. The intrinsic charge efficiency of bipolar chargers is limited by diffusional charge transfer and electrostatic attraction between particles and ions of opposite charge where smaller particles have low fractions of charged particles. For example, approximately 10% of total particles at $d_{\mathrm{m}} = 20$ nm have +1 charge at the bipolar charge equilibrium [26]. Since the net charge of a bipolar charger is nearly neutral, a classification stage would be necessary prior to an electrometer stage adding to the cost [26, 6].

Unipolar charging methods such as corona discharge achieve higher intrinsic charge efficiencies, but introduce more multiply charged particles and less clearly defined charge states as there is no equilibrium charge state equivalent to the bipolar charging methods [53]. Therefore, the rate of ion transfer to particles must be known or calibrated for [54, 41, 55]. Corona discharge is used in fast mobility analysers (e.g. ELPI, EEPS, FMPS, DMS500) where parallel measurement requires an efficient charging technique. Corona chargers are generally reliable and charging depends weakly on the material of a particle [6]. However, they require high voltage power converters (of order 3 kV), always produce some ozone and, depending on the carrier gas, undesired species or particles may result [56]. The charging efficiency of corona based chargers is a function of the ion-particle collisions and is limited by electrostatic repulsion between like-charged ions and particles. The measurements of low-cost sensors which operate using diffusional charging are linearly proportional to concentration and diameter, $i \sim Nd^1$ which is arguably relevant to health impacts when presented as LDSA [41].

Direct particle photoionisation using ultraviolet (UV) light presents an alternative charging mechanism to both unipolar and bipolar diffusion charging. Ultraviolet light charges particles with higher intrinsic charging efficiency than diffusion based methods for some particle materials depending on the intensity and wavelength of the UV light, since the particles are ionised directly, rather than relying on ion-particle charge transfer [57, 58]. Photoionisation of nanoparticles can occur without producing ozone and without the need for high voltage sources. However, lamps and driving circuits for UV light are often costly and require further optical conditioning, and design considerations such as photoemission from housing walls must be considered [57]. The mechanisms and rates of photoelectric charging of aerosol particles are not completely understood in terms of particle size, concentration, chemistry, surface properties, and morphology making it difficult to interpret measurements from photoelectric charging-based devices, particularly for ambient measurements where particle sources vary.

1.2.3 Photoemission theory and governing equations

The photoelectric effect has been studied extensively for photoelectric emission from flat surfaces [59] and has been used as a basis for important scientific discoveries such as the quantum theory of radiation [60]. The study of the photoelectric effect applied to aerosol particles has developed over the past several decades after it was discovered that ultraviolet light could provide high efficiency electric charging of aerosol particles [61]. Direct ultraviolet (UV) photoionisation enables increased charging of some nanoparticle materials over alternative charging mechanisms such as diffusion charging by directly charging parti-

cles using sufficiently high energy photons [62–64]. The higher states of particle charging, collision free charging mechanism and material dependency provide opportunities for improvements in environmental and emissions measurement [65, 40], particle classification [66], capture [58, 67, 68], controlled deposition [69], and fundamental studies of nanoparticle material and surface properties [70–73].

Photoemission theory

There are three steps involved in photoemission from surfaces in a vacuum [74] and a fourth step is included for particles in a carrier gas [46]:

1. absorption of a photon and excitation of an electron;
2. movement of the electron to the surface;
3. overcoming of the surface potential; and
4. removal of the electron from the vicinity of the particle.

Step 1 requires that the photoemitting material is exposed to the photon flux and step 4 requires that photoemitting material is located externally-to rather than shielded inside the particle. Electrons emitted from the particle interior may be reabsorbed by material within the same particle and never escape [72].

When photons of sufficient energy are absorbed, the particles emit electrons, which in turn collide with the surrounding air and form gaseous ions [46]. The remaining particle retains a positive charge which increases the photon energy required to release additional electrons due to electrostatic attraction. Photoelectric emissions occur when the energy of an irradiating photon is higher than the work function of the particle surface. The original Fowler-Nordheim equation for flat surfaces is extended to solve for the probability of photoelectric charging spherical particles from charge level q to $q+1$, called a combination coefficient [59, 75], $\alpha^{q\to q+1}$,

$$\alpha^{q\to q+1} = Y\frac{I}{4h\nu}\sigma_{\text{ph}} \tag{1.2}$$

$$Y = K_c\left(h\nu - \Phi^{q\to q+1}\right)^m \tag{1.3}$$

where I is radiative energy flux, σ_{ph} is the photoelectrically active area, $h\nu$ is the photon's energy, where ν is the photon's frequency and h is Planck's constant. The photon's energy, $h\nu$, must be greater than the particle surface work function, $\Phi^{q\to q+1}$, to result in a positive emission probability, and the proportionality function increases with the excess specific energy raised to a power m [57]. The value of the exponent, m, has been determined

as around 2 for metals and a few non-metals [76–78], while one study has shown that $m = 3$ for diesel particles [79]. The proportionality constant, K_c, is material dependent and empirically determined as a fitting parameter for the quantum yield per incident photon, Y. The photoelectrically active area is defined only qualitatively as the part of the surface which contributes to photoemission [46], though it is defined explicitly as $\sigma_{\text{ph}} = \pi d^2$ for perfect spheres in some literature which is appropriate for modelling purposes [75, 80, 58]. The factor of 4 in the denominator of Eq. 1.2 represents the difference between the total surface area and cross-sectional area of a sphere, and is included here for consistency.

Once an electron is emitted, the work function, Φ, increases [81] according to:

$$\begin{aligned} \Phi^{q \to q+1} &= \Phi_\infty + \frac{2V_e}{d}\left(q + 1 - \frac{5}{8}\right) \\ V_e &= \frac{e^2}{4\pi\varepsilon_0} \end{aligned} \tag{1.4}$$

where Φ_∞ is the work function of a flat surface of the same material and V_e is the elementary electron potential for electron charge, e, and vacuum permittivity, ε_0. The $q+1$ term represents the Coulomb force between a released electron and the remaining charged particle which must be overcome by the photon energy to emit the electron. After each electron is released, the Coulomb force increases and opposes further release. The $\frac{5}{8}$ term represents a reduction in the work required to move an electron to infinity from outside a sphere compared with that of a flat surface [81]. Michaelson [82] compiled work functions for flat surfaces of a variety of elements and the results range from ≈2 eV to ≈5 eV depending on the atomic structure. For example, the work functions, Φ_∞, of polycrystalline silver (Ag) and pure carbon (C) are 4.26 eV and 5 eV, respectively.

As long as the incident photon energy, $h\nu$, is greater than the work function, the particle continues to charge to a maximum level of charges per particle, $q_{\max}$, given by:

$$q_{\max} = \frac{2d}{V_e}\left(h\nu - \Phi_\infty\right) - \frac{3}{8}. \tag{1.5}$$

The $\frac{3}{8}$ term represents the image charge effect on $q_{\max}$ and may be neglected for $q_{\max} \gg 1$. The maximum charging is further limited by ion-particle recombination, deglomeration or in extreme cases, Coulomb explosion [62].

Ion-particle collision

The emitted electrons of photoionisation attach to gas molecules (e.g. oxygen) or impurities within $\sim 10^{-5}$ s, creating gaseous ions, referred to henceforth as ions [61, 83]. The electrical mobility of the resulting ions is on the order of 100 times greater than the remaining charged particles in the size range of interest (10-300 nm diameter), depending on particle size and charge level. The gaseous ions may diffuse back to and transfer charge to the charged particles, thereby neutralising them, as illustrated in Fig. 1.1. If ions are removed due to diffusional losses to walls or by capture in a low-strength electric field, ions are less likely to recombine with the charged particles, thereby increasing the charge on the particles. In an irradiated region, both photoionisation and ion-particle recombination take place, whereas in a UV irradiation free region, only recombination is possible.

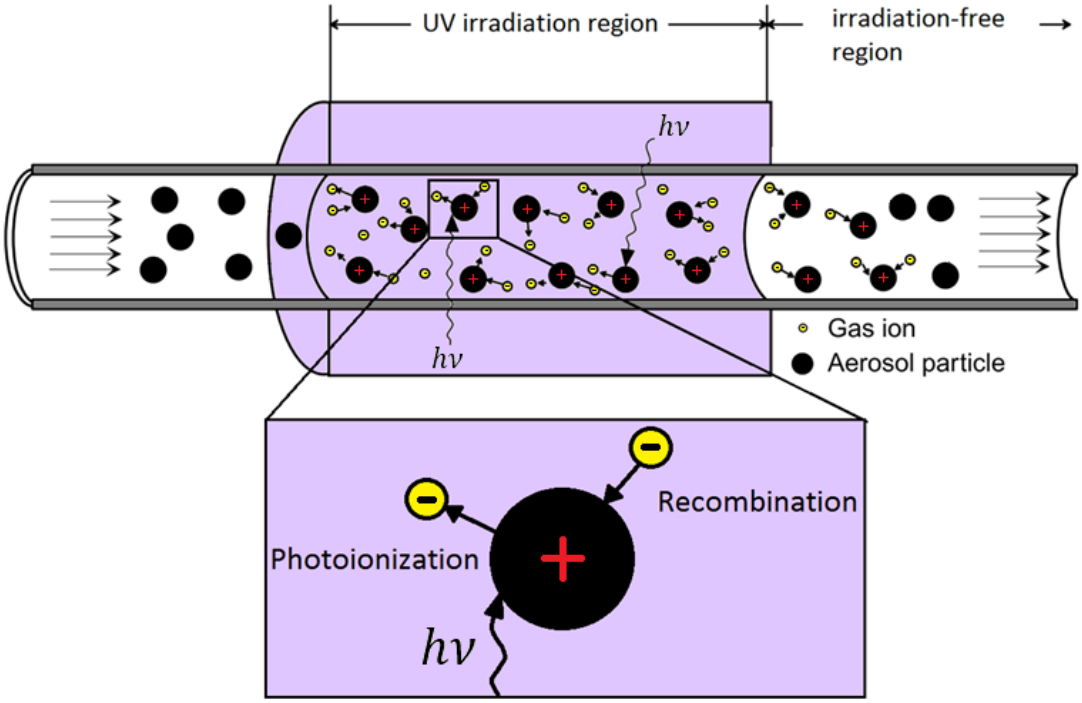

Fig. 1.1 Photoionisation and recombination of particles entrained in flow.

Recombination proceeds according to the same collision processes between ions and particles associated with diffusional charging or neutralisation. The collision rate coefficient, β, is defined to quantify the rate of collision between ions and particles. In this work, β is calculated using the method of Hoppel and Frick [84] and Fuchs [25], which accounts for diffusive and electrostatic forces. Efforts have been made to develop improved expressions for β to supplant or extend the range of validity this method [85, 86], sometimes including ion mobility distributions [87]. For details of the collision coefficient calculation used in this

work, see Reischl et al. [88] which contains a useful summary of Hoppel and Frick's [84] method which is summarised as

$$\beta = \frac{\pi\delta^2 c\ \alpha_C(q)}{\exp(\frac{\varphi(i(q),\delta)}{k_B T}) + \frac{\delta c\ \alpha_C(q)}{4D_\mathrm{i}} \int_0^1 \exp(\frac{\varphi(i(q),\delta/x)}{k_B T})\, dx} \tag{1.6}$$

where

$$\varphi(i,r) = V_e \left(\frac{i}{r} - K \frac{(d/2)^3}{2r^2(r^2-(d/2)^2)} \right). \tag{1.7}$$

The collision rate coefficient includes the mean molecular velocity, c, and collisional cross sectional area, $\pi\delta^2$, where δ is the limiting sphere radius. The collision rate also includes ion diffusivity, D_i, Boltzmann's constant, k_B, and temperature, T. The ion-particle collision probability, α_C, depends on charge and distance [88]. The electrostatic potential, φ, is a function of particle material, diameter, d, and distance from the centre of the particle, r, where $K = 1$ for a perfectly conducting particle. The number and polarity of particle charges, i, is positive if the ion and particle are of the same polarity.

Governing transport equations

In-situ measurements using the conventional principles of charge conditioning, classification, and particle counting require a continuous flow of particles in which electrical charging and transport of particles and ions affect measurements. By accounting for the populations of charged particles and ions, the net effects of photoelectric charging and ion-particle recombination are quantified in analytical or numerical models of aerosol particle charging and transport.

Photoionisation changes ion and particle charge states, acting as a source or sink for ions and charged particles, which can be recombined or transported by convection, diffusion or electric forces. The general steady-state conservation equations for the number of particles of a given charge, q, and size, b, and ions of charge, j, in a differential control volume are given as:

$$\nabla \cdot \left(\vec{u} N_{q,b}\right) = \nabla \cdot \left(D_p \nabla N_{q,b}\right) + \nabla \cdot \left(Z_{q,b} \vec{E} N_{q,b}\right) + S_{q,b,\alpha} + S_{q,b,\beta} \tag{1.8a}$$

$$\nabla \cdot \left(\vec{u} n_j\right) = \nabla \cdot \left(D_i \nabla n_j\right) + \nabla \cdot \left(Z_j \vec{E} n_j\right) + S_{j,\alpha} + S_{j,\beta} \tag{1.8b}$$

where N is the concentration of particles of a given material, and n is the concentration of ions. The transport of particles and ions is described by the local carrier gas velocity, $\vec{u}$, in the convection term, particle diffusivity, D, in the diffusion term, and electrical mobility, Z, multiplied by the electric field vector, $\vec{E}$, representing the electrical transport term.

The source/sink terms, S, represent the rate of increase or decrease in the number concentration of the particles or ions owing to either photoionisation or recombination via ion-particle collisions involving Eqs. 1.2 and 1.6, respectively. For example, if a negative ion, n_{-1}, attaches to a particle with a single positive charge, N_{+1}, the particle reduces to a neutral charge level, N_0, and the ion returns to a neutral gas molecule. It is assumed here that the concentrations of neutral gas molecules greatly exceed those of ions or charged particles, so that their concentrations remain unchanged.

1.3 Problem statement

The study of aerosol behaviour and its effects requires measurement of a range of particle properties for each intended application [6]. Small, low-cost field sensors are required for regulation and control of ultrafine particle emissions and epidemiological studies of the health impacts of local air pollution [10]. As health effects are better understood, measurements of ultrafine particles in particular are increasingly of interest [16]. Conventional methods for detailed particle measurements are prohibitively expensive for highly spatially-resolved air pollution monitoring [17]. Direct ultraviolet aerosol photoionisation offers an alternative charging mechanism to diffusional charging with a different dependence of charging rate on particle size and concentration [46]. Ultraviolet photoemission is material dependent and could be valuable for source-apportionment studies and/or studies of exposure to specific, harmful aerosols within heterogeneous aerosol mixtures [19]. However, any practical measurement device or diagnostic technique must be accompanied by sufficient understanding and interpretation of measurements using validated particle photoemission theory.

Validation of photoemission theory requires assessing which mechanisms of electrical charging and transport are dominant and/or affect measurements in combination with others. It is necessary to ensure measurements accurately represent the physical mechanisms being considered such that they are not conflated or implicitly neglected for a given set of conditions. In some cases, analytical models are adequate, however, often sophisticated numerical models which account for a range of physical effects are required to properly interpret measurements. Only with sufficient understanding of each of the possible contributions to measurements, the core photoemission theory may be evaluated and particle-light interactions may be better understood.

The processes involved in nanoparticle photoionisation are not well characterised for different particle types or larger sizes from the free-molecular to continuum regimes. Photoemission theory includes empirical constants which vary with a particle's size and material. Mechanisms of ion-particle collisions are well understood, at least for spherical and electrically conductive particles, but charging models often neglect significant ion and particle transport effects. In this work, comprehensive theoretical, modelling and experimental techniques are developed to investigate photoionisation, particle-ion interactions and transport. Developments in understanding are used to inform design decisions towards a method for accurate and quantitative classification and detection of particles.

1.4 Scope

The aim of this work is to understand the fundamental photoionisation mechanisms, particle-ion interactions and transport of nanoparticles in the free molecular and continuum regimes as a means to evaluate photoionisation theory in order to correctly interpret measurements from a low-cost aerosol particle sensor. To accomplish this, theoretical equations are analysed, applied in numerical and computational fluid dynamics models and compared with experimental results for validation. The photoelectric yield of aerosol particles is explored in terms of particle size, concentration, material, and morphology giving insight into the interaction of light and particles.

A non-dimensional analysis is performed to indicate regimes under which the photoelectric charging process is dominated by diffusion, transport in an electric field, convection, photoionisation, or recombination. In particular, the ratio of characteristic irradiation to recombination time defines the regime when charge saturation is reached, which is a function of particle size, concentration, material, and radiation wavelength and intensity.

The physical processes of photoionisation and recombination of ions and particles are modelled in three-dimensional (3D) computational fluid dynamics (CFD) for the first time. The transport equations of upwards of one hundred species are solved to allow the resolution of local, discrete charge states of polydisperse particle distributions. The detailed terms obtained in the charge balance equations are analysed to understand the range of validity of assumptions made for diffusional losses at walls, transport in an electric field, and particle polydispersity in zero-dimensional (0D) analytical and numerical models. Recommendations are made regarding the level of detail required for the prediction of aerosol charging and capture methods over a range of conditions used in experiments or the predictive design of photoelectric charging-based devices.

An experimental photoionisation chamber with a fixed-wavelength UV light source and detection system is outfitted with a low strength electric field (of order 10 V cm^{-1}) in order to capture ions, reduce recombination, and increase the particle charge state in a continuous flow of aerosol nanoparticles. The electric field enables measurement of two distinct currents: the first from ions captured in the photoionisation chamber, and the second from the remaining charged particles. Measurements of electrical currents resulting from photoemission from soot particles are compared with those calculated from the 3D computational fluid dynamics model to validate the model. A single empirical constant and particle work function are used in the photoionisation equations. The novel approach of using an electric field to yield two distinct electrical current measurements is demonstrated to be useful for measurements of size and concentration parameters of a known aerosol material.

The experimental photoionisation chamber is used to measure photoemission from agglomerated silver and sintered close-packed spheres in order to determine the effect of particle size and morphology on photo-emission yield. Direct and catalytically oxidised agglomerates of carbon from a propane flame are measured to demonstrate the effect of different particle material types and surface properties. The photoelectrically active area is defined explicitly to reflect the effect of a particle's morphology on total photoelectric yield.

1.5 Organisation of thesis

After the introduction, Chapter 2 contains a review of the relevant literature on UV photionisation of aerosol particles in the context of sensor design. The numerical and experimental methods are described in Chapter 3. In Chapter 4, the dominant processes in photoelectric charging and particle and ion transport are assessed using analytical modelling techniques. Then, the range of validity of assumptions made for diffusional wall losses, external electric field, and particle polydispersity in 0D analytical and numerical models are evaluated. In Chapter 5, the numerical modelling techniques are validated by comparison with experimental measurements for photoelectric yield of soot from a propane flame for a range of parameters. The dependence of photoelectric yield on particle size and concentration are demonstrated. In Chapter 6, the effect of particle morphology is shown by comparing photoelectric yield from agglomerated silver and sintered close-packed spheres. The definition of photoelectrically active area is defined to include particle morphology. Finally, Chapter 7 concludes the work with a summary of key contributions.

Chapter 2

Literature Review

2.1 Introduction

To develop aerosol sensor technology and correctly interpret measurements, the underlying physical principles of operation should be understood and the effects of design and operating parameters should be considered. The following describes the advancement of theory, modelling, experimentation and applications of aerosol photoionisation and other processes fundamental to this work.

The foundations of understanding of aerosol photoemission were provided by the research of Schmidt-Ott, Burtscher, Niessner, Matter and Mohr of Switzerland through the 1980s and 1990s. They demonstrated high efficiencies of particle electric charging by photoionisation which provides opportunities for improvements in sensing, capture and control of aerosol particles [61, 89]. This chapter first discusses their early contributions to the development and applications of aerosol photoemission in chronological order where possible. Then, the effects of particle material, size, concentration, and morphology on aerosol photoemission are discussed by reviewing more recent literature on photoemission measurements. Development of modelling techniques and experimental validation of the theory of photoemission from particles are discussed. Finally, the outcomes of the literature review are summarised and the research opportunities are presented in the context of aerosol photoemission measurements.

2.2 Development and applications of aerosol photoionisation

2.2.1 Photoionisation theory

The study of aerosol particle photoionisation began to gain traction in 1978 when Schmidt-Ott and Siegmann [61] found that photoionisation could be used to obtain information on the concentration and size of a stationary suspension of aerosol particles. They use an oscillating electric field to measure the concentration of gaseous ions formed from emitted electrons. They presented a simple model for photoionisation and ion-particle recombination. In 1980, the same group theorised and demonstrated that the Fowler-Nordheim law, which is valid for metal surfaces, could be extended to apply to aerosols [59, 89]. However, the authors found that a material-dependent, photoemission pre-factor, is on the order of 100$\times$ higher than a flat surface for nanometer sized particles, an enhancement which is not fully explained by classical physics theory to date [90, 51]. The yield represented by the Fowler-Nordheim law is known to be a function of material type, an important concern in any application of photoionisation.

In 1981, based on a proof from Wood [81], Schmidt-Ott and Federer [77] extended the Fowler-Nordheim theory to include the effect of Coulomb and image forces of the remaining positively charged particles after photoelectric emission of electrons. They provided a set of equations which represent photoionisation, ion-particle recombination and decay rate to walls. They proposed that the exponential decay rates of ions and particles are separable by subtraction leaving a measure of particle size based on diffusional losses; however, their experimental evidence was limited. In 1982, Burtscher et al. [70] developed an apparatus to demonstrate photoelectric charging efficiency as a function of particle size and flow rate. They described a charge saturation limit, or the maximum photoionisation for a given particle using the Fowler-Nordheim equation. The authors qualitatively demonstrated that they reached a charge saturation limit by using low flow rates and high lamp intensity with both silver aerosol particles and garage exhaust. They captured the charged particles to demonstrate extrinsic charging efficiency of 65-85% for 100-200 nm diameter particles using a 9 W mercury lamp. The demonstrated high charging efficiencies and early theoretical understanding led to further applications.

2.2.2 Polycyclic Aromatic Hydrocarbons (PAHs)

In 1984, the group of Burtscher and Schmidt-Ott of Switzerland found that particles coated with polycyclic aromatic hydrocarbons (PAHs) had high photoelectric yield, or the yield of

electrons from photoemitting aerosol particles, compared with uncoated particles or those coated with aliphatic hydrocarbons [91, 44]. Niessner [50] determined that photoelectric activity is a linear function of adsorbed PAH surface area for each PAH type which led to the development of sensors for a range of applications including industrial hygiene, combustion control, diesel engine control, or in-situ measurements of PAH adsorption/desorption [92]. However, the authors found that different PAH types gave different levels of photoelectric yield without signal selectivity. Therefore they found it difficult to discern if the aerosol photoemission signal were due to PAH quantity, type or both quantity and type. McDow et al. [93] found the aerosol photoemission signal was correlated to the mass of PAH adsorbed (from stove exhaust and garage aerosol) on particles.

Rosatzin and Burtscher [94] showed that 254 nm light can selectively ionise PAHs while pure carbon will not be ionised at that wavelength, however, both will be ionised at 185 nm. Therefore, the ratio of signals from the two wavelengths may give a measure of PAH adsorbates on emitted carbon particles. This would give a measure of combustion completion or stoichiometry. Using only 254 nm light, they used a similar principle to demonstrate the use of an aerosol photoelectric sensor (APE) for feedback control of a furnace [95].

Matter et al. [57] demonstrated that diesel particles and carbon aerosol show different numbers of charges per particle for the same mobility diameter due to differences in adsorbed PAHs and volatile compounds at large particle sizes. Diesel particles have larger amounts of adsorbed PAH and therefore higher yield. However, the peaks of charge levels are broadened due to the effect of desorbing volatile organic compounds found in diesel. The results demonstrate the importance of particle surface properties on photoionisation.

2.2.3 Ultrafines

In 1988, Jung et al. [62] demonstrated high photoionisation efficiency of ultrafine particles ($d < 20$ nm), an enhancement which is beneficial for a range of applications involving ultrafine particles. They developed a device with a wire mesh inside a quartz tube to avoid an electrostatic charge at the walls while still allowing UV light transmission from an external light source. The method allowed multiple charging of ultrafine particles up to 3 and 4 charges per 7.3 nm diameter particle using 15 W low pressure mercury lamps. Müller et al. [76] demonstrated an enhanced photo-electric yield of 200$\times$ for silver particles over a flat surface of the same material. They confirmed that the extended Fowler-Nordheim equation from Wood [81] is accurate for the effect of image and Coulomb potentials for small spheres near the threshold. Both Müller et al. [96] and Schleicher et al. [90] showed enhanced charging up to 9 eV light energy greater than the work function ($\approx$4.5 eV), but did not account for gas ionisation or photochemical reactions which can all occur when using light

of high intensity and wavelengths lower than about 190 nm [57]. Schleicher et al. [90] gathered more detailed work functions for nanoparticles of a few different metals. They demonstrated that metals other than silver also exhibit approximately 100× enhancement in yield compared to a bulk material. Ultrafines are charged more effectively by photoionisation than by conventional diffusional charging methods such as corona discharge for some particle materials, depending on the wavelength and intensity of light, thereby creating the opportunity for enhancements in applications such as aerosol sensing and electrostatic precipitation [70, 57, 97].

2.2.4 Detection of aerosol material

In a book chapter, Burtscher [46] summarised the two regimes for photo-charging: first, the linear regime in which charging for a given material depends on UV light intensity, residence time and an empirical constant and, second, the charge saturation limit regime in which the aerosol is saturated and will not photoionise further with higher intensity or longer residence time. The author showed experimental results which demonstrated the transition from the linear charging regime to the charge saturation limit. Using these principles, Matter et al. [57] characterised aerosol particles of carbon, metals and exhaust particles from a diesel engine. Using the equation for yield at the charge saturation limit, they hypothesised that particle diameter and work function could be estimated by alternating two wavelengths of light. Particles of 60, 90 and 120 nm diameter were charged to the theoretical maximum, $q_{\max}$, under high intensity lamp conditions. For a KrCl lamp (222 nm, 5.6 eV) at high intensity, they reached charge saturation with an average of 29.5 charges per particle at 120 nm monosized particles matching the theoretical maximum of 29-33. They demonstrated that different materials yield different enough responses to distinguish work function, however, they could not reach the Coulomb limit with their lower intensity lamp, thereby limiting their experimental conclusions. Mohr et al. [63] obtained similar results for charging efficiency of diesel particles at two wavelengths. They noted that particles in the flue gas from burning coal could not be photoelectrically charged with reasonable efficiency, limiting the applications of their method.

2.2.5 Photoelectric Aerosol Sensor (PAS)

The early demonstrations of photoelectric yield from small particles and PAHs, and potential for sensors which can differentiate aerosol materials, led to the design and commercialisation of a Photoelectric Aerosol Sensor (PAS) [98].

The PAS sensor was originally intended to selectively measure PAH concentration due to its high photoelectric yield [44], but was found to respond to elemental carbon at a lower yield [45]. Dahmann et al. [45] demonstrated that the PAS signal tracks the mass concentration of elemental carbon. Matter et al. [99] demonstrated that the PAS is adequate to track sub-micron particle concentration from diesel exhaust emissions.

Bukowiecki et al. [65] demonstrated the diffusion charging (DC) and PAS response to diesel and ambient aerosols. They found that when large nucleation mode particles are present, the PAS signal reduces compared with diffusional charging methods. Kittelson et al. [22] confirmed these results by studying the effect of a catalytic stripper (CS) which selectively removed volatile compounds and nuclei mode particles in diesel exhaust. They found that PAS signal increased when the CS was used, whereas DC measurements and total mobility surface area from SMPS measurements both showed a sharp decrease due to the lost nuclei mode particles. They concluded that a large nuclei mode and/or presence of a volatile layer on the surface of solid agglomerates suppressed the PAS response. Later that year, Jung and Kittelson [40] and Burtscher [98] found further chemical dependent responses of the PAS sensor to diesel engine load. At lower engine load, a higher volatile organic fraction was emitted which is not as responsive to photoelectric charging.

Without sufficient understanding of the chemical and surface dependent nature of photoemission, the applicability of the PAS sensor is limited despite the high yield for carbonaceous particles and particles of size below 30 nm diameter. The most recent version of the sensor is still commercially available (PAS 2200CE; EcoChem Analytics, League City, TX, USA).

2.3 Effect of aerosol characteristics on photoelectric emission

2.3.1 Material type

The dependence of photoelectric yield on material and surface properties introduces the opportunity for sensing aerosol material type when the other operating parameters are known such as the photoelectrically active particle surface area, σ_{ph}. Photoelectric yield is found to be a strong function of material, with relatively high yields for silver, polycyclic aromatic hydrocarbons (PAHs) and elemental carbon, whereas aerosols such as NaCl [40], di-octyl sebacate (DOS), and secondary organic aerosols are weak photoemitters in the UV spectrum. Conversely, the presence of adsorbates such as water on photoemitting particles are found to reduce or eliminate photoemission [100, 65].

It has been proposed that by combining material-dependent (photoemission) and material-independent (unipolar diffusion charging) measurements adjusted for particle size and concentration, a chemical fingerprint of surface properties of an aerosol could be determined [46, 48]. The ratio of photoelectric charging (PC) to diffusion charging (DC) has been used to investigate a range of indoor and outdoor aerosols [19, 99, 65, 22, 98]. However, the aerosol must have a homogeneous surface material composition, both the PC and DC signal must be dominated by the aerosol material of interest, and the DC signal must scale with the same particle geometric and concentration parameters as the PC signal to generate a strictly material-dependent chemical fingerprint. Corona-charged DC sensors yield signals linear in both particle concentration and particle diameter, $i \propto Nd$ [39–41, 37], for ultrafine particles ($20 < d < 200$ nm), which is a different set of size and concentration parameters from the photoelectrically active surface area measured by PC sensors.

2.3.2 Particle size and concentration

Total photoelectric yield is defined as a linear function of the photoelectrically active surface area, σ_{ph}. The latter is not explicitly defined, though it is demonstrated as proportional to total (mobility) surface area, A_{m}, where, for monodisperse particles, $A_{\mathrm{m}} = Nd_{\mathrm{m}}^2$. In the free molecular regime, the inverse of particle mobility is largely proportional to the square of mobility diameter, d_{m}^2. Photoemission yield has been demonstrated to be proportional to total mobility surface area or inverse particle mobility in the free molecular regime ($20 < d < 100$ nm) for sintered spheres and fractal-like silver agglomerates [47, 101, 51], recrystallised Ag and Au [48], PAH coated graphite aerosols (measured by diffusion battery) [50], carbon agglomerates [46], and denuded diesel exhaust particles at five representative engine modes [49, 22]. Measurements of the aerosol total active surface area are of interest for emissions, environmental or exposure monitoring, particularly for materials such as elemental carbon and diesel soot, however, the dependence of particle material and morphology on photoemission must be understood.

2.3.3 Particle morphology

The photoelectric quantum yield has been found to vary between different morphologies of the same pure material. Three studies which discuss morphology effects on aerosol photoemission in detail seemingly contradict one another [51, 48, 101].

Zhou et al. [51] studied the charging dynamics of spheres and aggregates using the same experimental set-up as a previous study in which particle work functions were measured [102]. Aerosol particles were drawn through a neutraliser and DMA to measure the true size

distribution, then the same aerosol was drawn through a photoionisation chamber and DMA to measure the effect of photoelectric charging. This was a single DMA system rather than a tandem DMA system and therefore the process could not distinguish between single or multiply charged particle states other than by a direct comparison they made for 30 and 60 nm particles. Single charged states could not be confirmed for the whole range of particle sizes used. A process with dominant photoionisation will likely produce multiply charged particles thereby affecting the measurements of the distribution of electrical mobility as well any calculation of charging efficiency. A condensation particle counter alone is insufficient to account for the increased charge states of multiply charged particles. Charging efficiency normalised by light intensity was found to be proportional to d_{m}^2 for both spheres and aggregates where d_{m} is the mobility diameter. However, the authors found the overall charging efficiency of silver aggregates to be 0.4-0.8 times that of silver spheres of the same mobility diameter. This result disagrees with an existing photoemission theory which suggests that particles of the same material and mobility should have the same photoelectric charging efficiency regardless of their morphology [48]. Further, Schmidt-Ott [101] demonstrated that sintering agglomerates into close-packed spheres reduced the photoelectric charging efficiency, though the effects of changes in particle mobility and morphology were treated together as a function of sintering temperature. The author explained that the reduced photoelectric efficiency of the sintered particles was due to the reduced number of primary particles exposed to the surrounding gas molecules. Schmidt-Ott [101] proposed photoelectric charging as an *in situ* measure of particle shape factors. The analysis suggests the charging efficiency of agglomerates should be higher than that of spheres with the same mobility diameter, but such results have not been directly compared.

2.3.4 Modelling and experimental validation

Validation of photoemission theory requires that models represent the physical processes which contribute significantly to the experimental measurements used for comparison. Mohr and Burtscher [97] used experimental and modelling techniques to show the influence of particle concentration on photoionisation. At higher concentrations of 10^5-10^6 cm^{-3}, they observe reduced charging efficiency due to an increasing role of ion-particle recombination. They assumed a charge distribution and modelled a set of equations for the recombination process which occurs after the outlet of the irradiation chamber.

Maisels et al. [75] derived an analytical solution from a set of differential equations for photoelectric charging and ion-particle recombination of a polydisperse, multi-component aerosol. They are among the first to apply both charging and recombination equations in an irradiated region. They compared analytical results with a one dimensional numerical

solution which showed good agreement for multiply charged particles. They included some limited experimental validation. Maisels et al. [80] continued the work by incorporating a wall loss term. They assumed that losses of ions to a cylinder wall could be represented by a time of diffusion to the wall. However, the wall losses are not separable from local effects of charging/discharging which requires spatial resolution of charge transport as well as time.

Van der Zwaag et al. [103] developed a CFD model which includes coupled fluid flow, ion and particle transport, electric field, and particle charging due to thermo-emission and photoemission using the CFD solver, FLUENT. They used an analytical equation which assumes only large, positive charges per particle are present. To date, the results are limited to a numerical comparison with Maisels et al. [75] for photoemission and recombination with good agreement in one dimension.

Further studies have evaluated photoemission theory by measuring the capture efficiency of photoionised particles in a high voltage electrostatic precipitator. Jiang et al. [58] presented a model for direct photoionisation, diffusional charging (recombination) and thermionic charging. Using their model, Jiang et al. [78] compared direct and indirect photoionisation of nanoparticles in a soft X-ray enhanced electrostatic precipitator. They found that direct photoelectric charging dominates over diffusional charging at high irradiation intensity, high photoemission constant and lower ion concentrations. They concluded that the photoemission constant increases by a factor of two as particle size is decreased from 15 to 6 nm based on experimental data, supported by claims of enhanced yield at low particle sizes [76]. The models and existing theory do not reflect any dependency of photoemission constant on particle size, therefore the model was altered to fit experimental data. Measuring capture efficiency in a high-voltage electrostatic precipitator implicitly neglects the effect of multiply charged particles on charge efficiency as all charged particles are captured regardless of charge state. They concluded based on previous research that the Fowler-Nordheim equation is valid for organic particles (sucrose) as well as metal particles (silver) in the 6-15 nm range.

Hontañón and Kruis [66] investigated the feasibility of using UV photoionisation for single-charging of nanoparticles at high flow rates up to 100 L min^{-1} for size selection as an alternative to diffusional charging methods. They showed that a UV photoelectric charger is effective in yielding singly charged particles when light intensity is optimised for flow rate, concentration and particle size. They introduced a model which neglects diffusional losses at walls and 3D effects and fitted a different photoemission constant for each different light intensity and flow rate. They did not quantitatively measure changes in light intensity for each measurement, therefore say very little about the experimental constant used.

Li and Chen [64] investigated the effect of UV light intensity on photoionisation of silver nanoparticles. They found that at low flow rates, while the intrinsic charging efficiency

increases due to a longer residence time, the extrinsic charging efficiency decreases due to increased particle losses to the walls and the ion trap. They quantitatively demonstrated an increase in intrinsic and extrinsic charging efficiency for their photoelectric charger over Twin Hewitt and mixing-type corona discharge diffusion chargers. For a range of light intensities, the photoemission constant showed no size dependence for 7-30 nm silver particles agreeing with photoemission theory and calculations and in contrast with previous research [58, 66].

Zhou and Zachariah [102] ionised 28.5 nm particles with collimated UV light of wavelengths between 200-280 nm using a monochromator. The authors demonstrated an increase in photoelectric yield as incident photon energy increases within the Fowler-Nordheim regime ($h\nu - \Phi \leq\sim 1.5$ eV). They demonstrated a decrease in photoelectric yield outside the Fowler-Nordheim regime when correcting for multiply charged particles and normalising by intensity. They ensured primarily single charging conditions by limiting the energy bandpass between 0.7 nm and 3 nm which reduces intensity for a given wavelength. They confirmed single-charging conditions with tandem DMA, however, it is not clear whether they ensured single charge states for every particle size used. In the same discussion, the authors concluded that the Fowler-Nordheim law, with classical image and Coulomb potentials, applies to aggregates as well as spheres. They found that the relevant size metric for aggregate work function is the primary particle size rather than mobility size of the whole aggregate.

2.4 Research opportunity

After a review of relevant literature, it was found that researchers recognise the benefits of aerosol photoionisation for electric charging with a range of applications including aerosol measurement devices. Researchers often cite the high efficiency of charging over conventional diffusional charging methods, particularly for aerosol particles smaller than 50 nm in diameter [64, 70, 57, 97]. It is also often cited that the material and surface dependency of photoelectric yield was a major consideration in the applicability of photoionisation as a particle charging technique [56, 61, 70]. There is room for improvement in theory, modelling and experimentation of the photoionisation, ion-particle recombination, transport and charge capture processes. The photoelectric charging theory should be critically analysed for its applicability in terms of the effect of particle size, concentration, material and morphology in order to understand better the physical processes and evaluate photoelectric charging as a technique for aerosol measurement.

Photoelectric yield has been shown to be a function of seemingly disparate measurements such as elemental carbon mass concentration [45], PAH surface area [50], and sub-micron diesel particle concentration [99]. Photoelectric yield has also been demonstrated as linearly

proportional to the inverse of electrical mobility [46–49] and total mobility surface area [50, 22, 51] for a range of particle types. However, the effects of particle size and concentration on photoemission measurements have not been evaluated in detail in the literature to date.

Further experimental work is needed to explore the photoelectric effect of material type, surface adsorbates and particle morphology. The measurement of a 'chemical fingerprint' based on the difference in photoelectric yield of different materials would be valuable for source-apportionment studies and/or studies of exposure to specific, harmful aerosols within heterogeneous aerosol mixtures [19, 99, 65, 22, 98]. Surface effects on photoemission from heterogeneous particles should be understood to inform measurements of the adsorbate itself [50] or ensure the particle samples are adequately conditioned [22]. The effect of particle morphology on photoemission is not well understood and should be clarified as the three studies which discuss morphology effects in detail seemingly contradict one another [51, 48, 101]. The individual effects of particle size, concentration, material, surface conditions and morphology must be understood such that measurements of any one parameter are not misinterpreted.

The modelling of photoionisation has not seen significant improvement since the application of the Fowler-Nordheim equation in a one-dimensional case with ion-particle recombination by Maisels et al. [75, 80]. More recent studies have evaluated photoemission theory by comparing modelling results with experimental capture efficiencies of photoionised particles in high voltage electrostatic precipitators [78, 58, 66, 64]; a method which implicitly neglects the effect of multiply charged particles. The equation for photoionisation yield includes an empirical constant which has been incorrectly applied as a fitting parameter for changes in particle size, light intensity, or flow rate [58, 66]. The photoionisation yield and ion-particle recombination equations must be complemented with transport effects to be accurately validated with experimental measurements which account for multiply charged particles.

The theory, models and experiments outlined in the following chapters aim to improve the fundamental understanding of the photoionisation and recombination mechanisms and to aid in the evaluation of sensor measurements.

Chapter 3

Methods

In this chapter, the operating method of an aerosol measurement device is presented which uses photoelectric charging and particle/ion transport to yield measurements of particle size and concentration. Then, the modelling and experimental techniques are presented; they are applied in subsequent chapters to understand the underlying physics of photoionisation and inform the design of a commercial sensor of particles.

3.1 Photoionisation measurement methods

In the direct photoionisation of particles, energy from ultraviolet light causes emission of electrons, yielding positively charged particles and negatively charged ions. Measurements of photoionisation may come from the electrical charge from either the charged particles or ions or both. Since positively charged particles and negatively charged ions are likely to recombine, it is important to understand, account for, and control the relative rates of ionisation and recombination in order to correctly interpret measurements. An ion trap is referenced in Hontañón and Kruis [66] as a potential method to increase charge levels by removing ions as they are produced during photoionisation. Burtscher et al. [95] applied a high frequency AC voltage to remove ions without largely affecting the charged particles.

In this work, a photoionisation chamber is designed with an externally applied electric field such that a continuous flow of particles and ions may be charged, captured, and measured in a controlled manner. An electric field from an externally applied DC voltage at two electrodes is used in a region irradiated with UV light in order to trap highly mobile ions as they are formed and before they have an opportunity to recombine with the particles as seen in Fig. 3.1. The positively charged particles and negatively charged ions are generated in a continuous flow chamber, where they are allowed to partly recombine, while influenced by an applied electric field (Figure 3.1). The net ionic flux to the electrode surfaces creates a

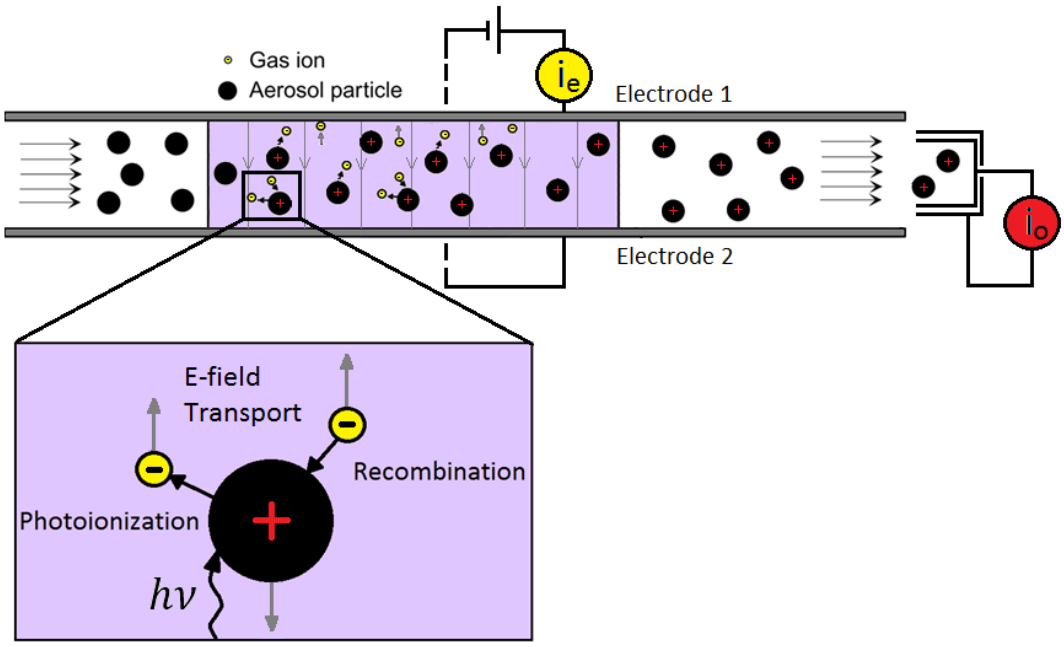

Fig. 3.1 Diagram of photoionisation chamber. Highly mobile ions and a fraction of the charged particles are transported by the electric field and captured, yielding an electrode current, i_e, which is generally net negative polarity. The remaining charged particles and ions are captured at the outlet yielding outlet current, i_o, which is generally net positive polarity.

current which can be detected at different locations. Negatively charged ions are transported to the positive electrode, while positively charged particles migrate to the negative electrode, both contributing to electrode current, i_e, which are measured by an electrometer in an external circuit. Negatively charged ions are gaseous and thus have electric mobilities of around 100 times greater than positively particles in the size range of interest (10-300 nm), so in general the corresponding negative ion flux is much higher than that created by the motion of positively charged particles and the electric current, i_e, is generally net negative in polarity. The remaining positively charged particles and negatively charged ions are transported through the chamber outlet to yield an outlet current, i_o, which is generally net positive in polarity.

In an idealised case, assuming there are no particle losses or external ion sources, every charge from a trapped ion should have an equal and opposite charge on the particles remaining in the flow. Therefore, the trapped ion current, i_e, and outlet particle current, i_o, should be of equal magnitude. Each current is, in the idealised case, directly related to the rate and efficiency of particle charging, so they contain information about the particle number and photoelectrically active area as described by Eq. 1.2 in the charging regime, before the Coulomb limit is reached and without dominant ion-particle recombination. The current is also a linear function of the number of ionised particles which may be quantified by the particle concentration and flux of particles.

By changing from a low voltage at the ion trap stage to a higher voltage, some of the most electrically mobile particles are captured along with the ions, thereby acting as a low-efficiency electrostatic precipitator similar to that found in low-cost unipolar diffusion chargers [39]. When the smallest, most mobile particles are captured, the remaining signal is a distinct function of concentration and particle diameter. By understanding the effect of the electric field strength as a function of measured particle properties and operating conditions, measurements which provide more particle information may be correctly interpreted.

To the best of the author's knowledge, the measurement of two distinct but equivalent currents for trapped ions and charged particles as described by i_e and i_o above has not previously been accomplished in a continuous flow device. The comprehensive modelling techniques described in this chapter are validated with experimental results in order to ensure that the photoionisation measurements are interpreted with the correct theoretical understanding.

3.2 Three-dimensional numerical model

Equations for three-dimensional (3D), steady-state convection/diffusion, photoionisation, recombination, and electric field transport of particles and ions are solved in three dimensions using computational fluid dynamics. The solutions of the particle and ion charging and transport equations are used to predict measured electrical currents from experiments.

3.2.1 Governing equations

The governing equations of continuity and momentum are solved for local carrier gas velocity and Gauss' equation is solved for the local electric field which, along with Brownian diffusion, dictate the transport of particles and ions in the photoelectric charger.

Continuity and momentum

The velocity and pressure fields are solved in the form of the steady-state Navier-Stokes equations in three dimensions. Mass conservation is given as the continuity equation for a unit volume in the form

$$\nabla \cdot (\rho \vec{u}) = 0 \tag{3.1}$$

where ρ is the carrier gas density and $\vec{u}$ is the three dimensional local velocity vector.

The momentum equation is applied as

$$\nabla \cdot (\rho \vec{u}\vec{u}) = -\nabla p + \nabla \cdot (\mu \nabla \vec{u}) \tag{3.2}$$

where p is pressure and μ is viscosity of the carrier gas, which is in this case air at NTP. The charged particles and ions are assumed not to affect the conservation equations of the carrier gas, that is, constant air density and viscosity, and negligible electro-hydrodynamic effects. The solved flow field is imposed in the advective term of the particle and ion concentration equations.

Electric field

An electric field is applied to influence the trajectory of particles and ions between two electrodes during photoionisation. A Laplacian equation is solved for an applied voltage, V, at the electrodes to generate a potential field. The local electric field, $\vec{E}$, is the gradient of the potential field according to

$$\begin{aligned} \nabla^2 (\varepsilon_0 V) &= 0 \\ \vec{E} &= -\nabla V. \end{aligned} \tag{3.3}$$

where it is assumed that the electric field distribution generated by the local distribution of particles and ions is negligible compared with the electric field generated by the externally applied potential. The space charge generated by high concentrations of unipolar charged ions or particles may cause non-uniform particle or ion losses due to significant electrostatic repulsion. Space charge effects are only significant for single charged particle concentrations of order 10^6 cm^{-3} and higher [104].

Particle and ion charging and transport

The particle and ion charge conservation equations may be generalised for the operation of bipolar and unipolar diffusion chargers and photoelectric chargers. The general form of the particle and ion conservation equations for particles are found in Appendix A.1. The dominant terms of the equations relevant to photoelectric charging are presented here.

The simultaneous equations for conserving the charge on particles account for the concentration of particles, N, at each charge level, q, and size bin, b, where a polydisperse distribution of particle sizes is made up of M monodisperse size bins. The particle and ion conservation equations are coupled through the source/sink terms for photoionisation and ion-particle collisions. Ionised gas molecules of monodisperse mobility and a single negative charge are represented by the number concentration n_{-1}: the photoionisation process causes the emission of (negative) electrons, which are assumed to immediately collide with gaseous molecules, generating negative ions. There is no significant source of positive molecular ions. The conservation equation for negative ions is shown Eq. 3.4b. The transport of particles and ions is described by the velocity, $\vec{u}$ in the advection term, diffusivity, D, in the diffusion term, and electrical mobility, Z, in the electric field transport term where $\vec{E}$ is the electric field. Assuming particles of a single material type and surface properties, the conservation equations for particles and ions are given as follows

$$\begin{aligned}\nabla \cdot \left(\vec{u} N_{b,q}\right) = \nabla \cdot \left(D_{b,q} \nabla N_{b,q}\right) + \nabla \cdot \left(Z_{b,q} \vec{E} N_{b,q}\right) \\ + \alpha_b^{q-1 \to q} N_{b,q-1} - \alpha_b^{q \to q+1} N_{b,q} \\ + \beta_b^{q+1 \to q} N_{b,q+1} n_{-1} - \beta_b^{q \to q-1} N_{b,q} n_{-1}\end{aligned} \tag{3.4a}$$

$$\begin{aligned}\nabla \cdot \left(\vec{u} n_{-1}\right) = \nabla \cdot \left(D_{\text{i,-1}} \nabla n_{-1}\right) + \nabla \cdot \left(Z_{\text{i,-1}} \vec{E} n_{-1}\right) \\ + \sum_{b=1}^{M} \sum_{q=q_{\min}}^{q_{\max}} \left(\alpha_b^{q \to q+1} N_{b,q} - \beta_b^{q \to q-1} N_{b,q} n_{-1}\right)\end{aligned} \tag{3.4b}$$

where the concentration of particles with charge q is changed by the net rate of particles acquiring or losing an extra charge due to photoemission and ion-particle recombination. The concentration of ions of a single negative charge is changed by the net rate of electron photoemission and ion-particle recombination at all particle charge states. The photoionisation combination coefficient $\alpha^{q \to q+1}$ is found in Eq. 1.2, and the ion-particle collision coefficient, $\beta^{q \to q-1}$, quantifies the rate of collision of a negative ion with a particle of charge, q. The ion-particle collision coefficient is a function of particle diffusivity and inter-particle potential, and is found in Eq. 1.6.

The three-dimensional equations may be solved in their zero-dimensional (0D) form assuming steady-state, plug flow and linear electric field and diffusion loss terms, and/or for monodisperse particle size as summarised in Table A.1.

3.2.2 Geometry and mesh

The geometry under consideration for a particle charger and detector is a 200 mm long cylinder of internal diameter 25 mm. For the electric field transport of particles, the outer cylinder makes up one electrode and the second electrode is a concentric rod of 1.5 mm in diameter and the full length of the cylinder. The computational mesh consists of a 45° section of a cylinder due to the axi-symmetric nature of the solution. Therefore, although the governing equations are solved in 3D, they could be optimised for an axi-symmetric solution. However, by solving in 3D, the model may be readily adapted to geometries with 3D effects. Unless otherwise specified, the mesh consists of six blocks of $10 \times 20 \times 50$ cells making up a total of 6×10^4 cells determined from a grid independence study. Simple linear grading towards the walls was applied where the highest concentration gradients occur.

Figure 3.2 shows a distribution of charges per particle and illustrates the geometry of the case under consideration. The flow proceeds from the circular inlet to the outlet, along the

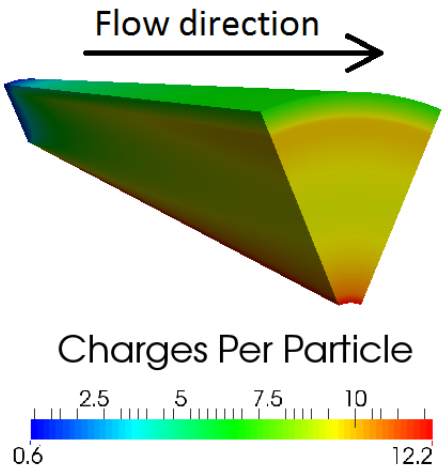

Fig. 3.2 Sample distribution of charges per particle during convective flow under irradiation. The charge level increases in the axial flow direction due to photoionisation.

axial direction. The light intensity properties are tailored to specific geometric configurations or operating conditions depending on the application. An electric field is applied which transports charged particles towards the centre rod, thereby increasing the concentration of highly charged particles near the rod. The bias voltage may be reversed to drive positively charged particles towards the outer cylinder electrode and attract negatively charged ions towards the centre rod electrodde.

3.2.3 Properties and boundary conditions

Initially neutral particles are entrained in a flow of air at NTP. A uniform velocity profile and fixed, neutral nanoparticle concentration is prescribed at the inlet. Boundary conditions of zero gradient are applied for velocity of air and ion/particle concentrations at the outlet and set to zero (or no-slip) at the walls. The boundary conditions for the conservation equations are summarised in Table 3.1. Diffusion of ions and particles in the direction of flow, the axial direction, is neglected.

The effect of UV light is represented by intensity, I (coupled with K_c), light energy, $h\nu$, particle work function, Φ_∞, and particle size as defined by Eqs. 1.2 and 1.4 applied in the photoionisation source terms. The radiation is modeled as from a 185 nm (6.69 eV) wavelength source, greater than the work function of most solids. The particle diffusion coefficient is a function of particle diameter using the mechanical mobility and Cunningham slip correction factor as outlined in Kulkarni et al. [6] for air at NTP. The particle electrical mobility is a linear function of the diffusion coefficients for a given temperature [6]. A uniform ion mobility distribution is assumed using properties gathered from Wiedensohler

Table 3.1 Boundary conditions for the conservation equations in three-dimensional model of particle and ion charging and transport.

Type	Momentum	Concentration	Voltage
Inlet	$u = U$, $\frac{\partial p}{\partial n} = 0$	$N_0 = N_{0,in}$, $N_{q\neq 0} = 0$, $n_i = 0$	$\frac{\partial V}{\partial n} = 0$
Outlet	$\frac{\partial u}{\partial n} = 0$, $p = 1$ bar	$\frac{\partial N_q}{\partial n} = 0$, $\frac{\partial n_i}{\partial n} = 0$	$\frac{\partial V}{\partial n} = 0$
Rod Electrode	$u = 0$, $\frac{\partial p}{\partial n} = 0$	$N_q = 0$, $n_i = 0$	$V = V_\mathrm{r}$
Cylinder Electrode	$u = 0$, $\frac{\partial p}{\partial n} = 0$	$N_q = 0$, $n_i = 0$	$V = V_\mathrm{c}$
Angular Symmetry	cyclic	cyclic	cyclic

et al. [105] (1.6×10^{-4} m^2 V^{-1} s^{-1}) which is within the range of more recent ion mobility distribution measurements from Maißer et al. [83] (1.5-1.9$\times10^{-4}$ m^2 V^{-1} s^{-1}) and Steiner et al. [106] (0.9-2.5$\times10^{-4}$ m^2 V^{-1} s^{-1}).

3.2.4 Solution procedure

The governing equations are converted to steady-state linear algebraic equations using OpenFOAM v.5. The operating parameters such as light wavelength, intensity, and particle size distribution can be selected at runtime. The solution algorithm proceeds as follows:

1. initialise the mesh, constants, solution fields, boundary conditions and other parameters;
2. calculate the photoionisation coefficients, $\alpha^{q\rightarrow q+1}$, of Eq. 1.2 based on input parameters;
3. initialise the attachment coefficients, $\beta^{q\rightarrow q-1}$, previously calculated in a separate MATLAB code for each monodisperse particle size bin from 1-300 nm and each charge level, q;

4. solve for the velocity and pressure fields using the PISO algorithm until convergence is obtained;
5. calculate the electric field using a Laplacian equation; and
6. calculate the ion, then particle concentration distributions until convergence is obtained between iterations for ion and particle charge distributions.

The steady conservation equations for particle and ion concentrations are solved, as shown in Eqs. 3.4a and 3.4b for negatively charged ions, all particle size bins, b[1], and all expected particle charge levels, q, between $q_{\min}$ and $q_{\max}$. The iteration of the concentration equations is enabled by the objected-oriented nature of C++ and user access to the source code and solvers of the CFD package used, OpenFOAM. In all simulations in this work, the minimum charge level, $q_{\min}$, is set as -5 charges per particle, which is sufficiently low such that the concentrations of all neutral and negatively charged particles in the system are calculated. The maximum possible charge level from Eq. 1.5 is calculated at runtime to determine $q_{\max}$ from Eq. 3.4b and the necessary number of simultaneous, coupled concentration transport equations (Eq. 3.4a) solved for each charge level. Solution time is a function of the number of simultaneous equations to be solved, which is determined by the range of charge states and the number of particle size bins; this time ranged from $\sim$1 min for monodisperse simulations to $\sim$1 h for polydisperse simulations with 16 particle size bins. All calculations are performed using a desktop computer (Intel® Core™ i7 3.40 GHz) with 16 GB of RAM running on openSUSE 13.1.

3.2.5 Post-processing

The total current measured is a linear sum of the particle charge flux from each size bin, b, and charge state, q, and the ion charge flux. The total contributions to electrical current are shown in general form in Eq. A.1d of Appendix A and are shown in simplified form here:

$$i_{\mathrm{o}} = \sum^{\mathrm{A}} \left(\sum_{b=1}^{M} \sum_{q=q_{\min}}^{q_{\max}} (qe\vec{u}N_{b,q}) - e\vec{u}n_{-1} \right) \cdot \mathrm{d}A, \tag{3.5a}$$

$$i_{\mathrm{e}} = \sum^{\mathrm{A}} \left(\sum_{b=1}^{M} \sum_{q=q_{\min}}^{q_{\max}} qeD_{b,q}\nabla N_{b,q} - eD_{\mathrm{i,-1}}\nabla n_{-1} \right) \cdot \mathrm{d}A. \tag{3.5b}$$

At the outlet boundary, the total outlet current, i_{o}, is calculated as the net advective flux of both charged particles and ions. The advective flux of ions at the outlet is negligible for the

[1] Loop through array of size bins for polydisperse distributions coded by Nene Yamasaki (U. of Cambridge)

conditions discussed in this work, therefore Eq. 3.5a shows only the charged particle flux. At the ion trap electrodes, no advection occurs, so the total electrode current, i_e, is largely made up of diffusive flux of ion charge enhanced by electric field transport as shown in Eq. 3.5b.

Local concentrations of ions and particles are calculated along with a range of variables such as pressure, velocity, and electrical potential. Visualisations are gathered using ParaView v5.4 and are exported to CSV format tables for further analysis.

3.2.6 Numerical verification

The model charging and transport equations are generalised to unipolar and bipolar diffusional charging along with photoelectric charging in Appendix A. In order to ensure that the equations are implemented correctly, 0D numerical results are compared to the existing 0D analytical and numerical results where available from literature for bipolar diffusional charging and [84] and photoelectric charging [75, 80] in Appendix B. Excellent agreement with literature results is obtained for the 0D numerical implementation in a MATLAB code as well as OpenFOAM. The code verification provides confidence in the 3D numerical implementation in OpenFOAM, where there are no previously existing literature results with which to compare directly.

3.3 Experimental methods

The experimental methods described in this section are used to validate the implementation of the 3D model charging and transport equations to ensure the physics of the processes are adequately understood. The understanding of the underlying physical principles is used to help explain a theoretical basis for new experimental results.

Firstly, the design of the photoionisation chamber used for photoemission measurements is described in detail. Secondly, an experimental apparatus is described which delivers high concentrations of a polydisperse soot aerosol with high signal-to-noise ratios used for experimental validation of the modelling techniques. Finally, an experimental apparatus is described which uses a particle size classifier to get detailed, size-resolved measurements of monodisperse aerosol particles used to re-evaluate the definition of an aerosol's photoelectrically active surface area.

3.3.1 Photoionisation chamber

The experimental photoionisation chamber provides a volume in which aerosol particles are irradiated with UV light and subjected to an electric field between two electrodes while in

continuous flow. The sample aerosol flows from a sample inlet at the side of a cylindrical chamber, through the volume between the two electrodes, and through a sample outlet at the side of the chamber. The first electrode is a 200 mm long aluminium cylinder of 25 mm internal diameter. A concentrically located silver steel rod (functioning as the second electrode) of 200 mm in length and 1.5 mm in diameter is mounted at the end of the photoionisation chamber nearest the outlet, extending co-axially along the entire length of the photoionisation chamber and electrically isolated with polytetrafluoroethylene (PTFE). A UV-extended fused silica optical window of 25 mm diameter and 3 mm thickness makes up one circular side of the cylindrical chamber. A 3 W UV lamp (Dinies Technologies GmbH, Germany: Model Mini3W-52ozon) is located externally, 20 mm from the window. The UV source and window are located nearest the sample inlet such that the flow direction is away from the light source. The lamp outputs narrow lines of ultraviolet light 185 nm and 254 nm. A high-pass UV filter was used to demonstrate that the 254 nm line yielded negligible photoelectric emission for carbon particles, therefore the 185 nm light was considered dominant for particle photo-emission. A voltage is applied between the electrodes in series with the electrometer current measurement, both using a Keithley electrometer (Keithley Instruments Inc., Cleveland, OH, USA: Model 6517B). The photoionisation chamber is enclosed in an electrically-isolated, aluminium box which acts as a Faraday cage and is grounded with the electrometer triaxial measurement cable. The electrometer provides electrode current, i_e, with a noise level less than ± 1 fA [107]. However, significant electrical noise from other sources increased the signal's uncertainty. Flow through the photoionisation chamber was sampled by the aerosol electrometer (TSI Inc., Shoreview, MN, USA: Model 3068B). A flow rate of 1.5 std L min^{-1} through the photoionisation chamber was provided by the aerosol electrometer which measured the electrical current due to particle filtration in a Faraday cup electrometer, i_o, with a noise level lower than 1 fA at one second averaging time [108].

3.3.2 Polydisperse soot measurement apparatus

The experimental apparatus described here provides a polydisperse sample of neutrally charged, carbonaceous soot particles to both a photoionisation chamber and a reference instrument.

The experimental apparatus used is shown in Fig. 3.3. Stable, carbonaceous soot particles were produced by burning propane (65-105 std cm^3 min^{-1}) with air (1.2 std L min^{-1}) in a co-flow inverse diffusion flame using N_2 (3 std L min^{-1}) as a sheath flow, followed by an ageing chamber as described in section 2.1 of Stettler et al. [109]. An electrostatic precipitator operated at 9 kV captured particles with any residual charge from the combustion process,

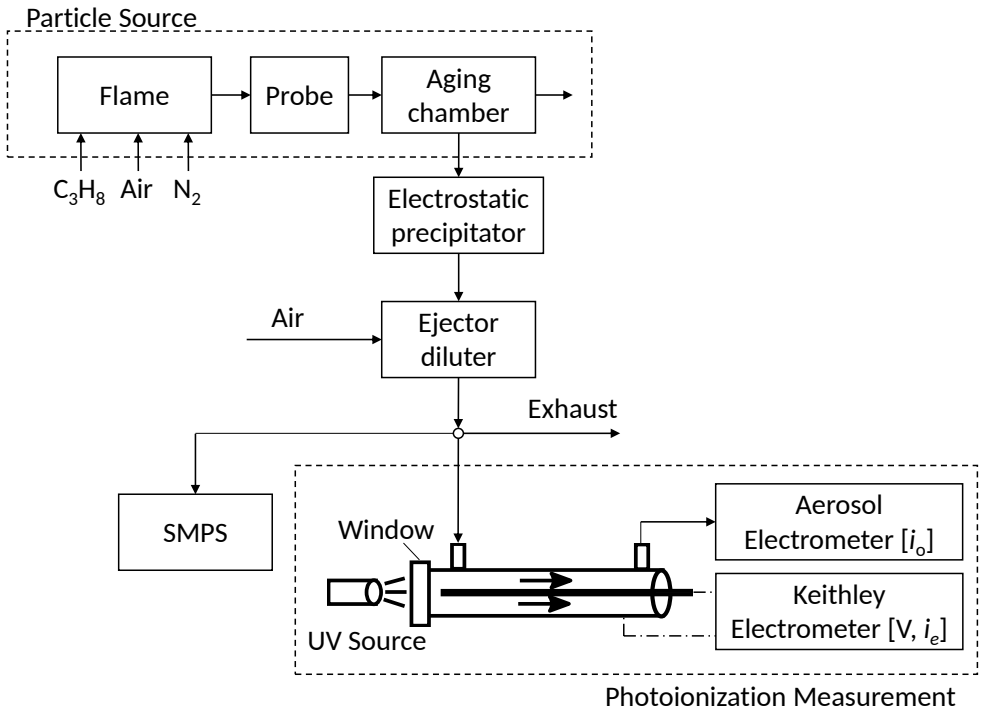

Fig. 3.3 Schematic of experimental apparatus for polydisperse soot photoionisation measurements.

confirmed using an aerosol electrometer (TSI Inc., Shoreview, MN, USA: Model 3068B). An ejector diluter with filtered compressed air provided a vacuum to draw the sample through the ageing chamber and electrostatic precipitator.

The concentration was varied by changing the diameter of the critical orifice in the diluter and the flow rate of dilution air. The particle size was varied by changing the flow rate of propane into the flame. Higher flow rates of propane yielded larger particles. The number-weighted particle mobility diameter, d_{m}, distribution was measured with a Scanning Mobility Particle Sizer (SMPS; TSI Inc.: 3080 Electrostatic Classifier, 3081 Differential Mobility Analyzer [DMA], 3025 Condensation Particle Counter [CPC]). In parallel with the SMPS, the UV photoionisation chamber described in section 3.3.1 provided photoionisation measurements. Stainless steel and conductive silicone tubing were used to minimise particle losses in the sampling lines.

3.3.3 Size-resolved particle measurement apparatus using Aerodynamic Aerosol Classifier

The experimental method described here allows measurements of photoelectric yield for a range of resolved particle sizes of monodisperse, initially neutral particles. Charge efficiencies of bipolar chargers significantly reduce the throughput of classifiers which depend on particle charge, for example, the Differential Mobility Analyzer (DMA) (Sec. 1.2.2) [26]. For this reason, the Aerodynamic Aerosol Classifier provides relatively high concentrations of monodisperse, neutral particles[2] compared with particle classification via a DMA and subsequent charge conditioning (Sec. 1.2.1) [29].

The experimental apparatus is shown in Fig. 3.4. The aerosol source was either carbonaceous soot or silver (Ag) particles. Carbonaceous soot particles were produced by burning propane (flow rate of 105 std cm^3 min^{-1}) with air (1.2 std L min^{-1}) in a co-flow inverse diffusion flame using N_2 (3 std L min^{-1}) as a sheath flow, followed by ageing in an ageing chamber as described in section 2.1 of Stettler et al. [109]. The aerosol sample flow either bypassed or passed through a catalytic stripper operated with an internal gas temperature of 350°C (Catalytic Instruments GmbH & Co.KG, Rosenheim, Germany: Model CS015) to remove semi-volatile organic carbon, confirmed with a Horiba gas analyser (Horiba Ltd.: Model MEXA-584L). A vacuum pump (Edwards, Burgess Hill, UK: Model Speedivac 2) and mass flow controller (Alicat Scientific, Tucson, AZ, USA) were used to draw the sample flow through the ageing chamber and catalytic stripper at a constant flow rate of 1.5 std L min^{-1}. Silver agglomerate particles were produced by evaporation and subsequent condensation using a tube furnace operated at 1200°C (Lenton, Hope, UK: Model LTF 12/25/500). Inside the furnace, a flow of HEPA-filtered, dry N_2 at 2 std L min^{-1} carried evaporated silver from three evenly distributed combustion boats containing pure silver. The aerosol sample flow either bypassed or passed through a second furnace (Elite Thermal Systems Ltd., Market Harborough, UK: Model THH12/90/305) operated at 600°C to sinter the agglomerate particles into close-packed structures [101, 51].

From either aerosol source, the sample was drawn through an electrostatic precipitator operated at 8 kV to capture particles with any residual charge from generation, confirmed using an aerosol electrometer (TSI Inc., Shoreview, MN, USA: Model 3068B). The particles were then passed through an Aerodynamic Aerosol Classifier (AAC; Cambustion Ltd., Cambridge, UK) which classifies particles based on aerodynamic diameter (Sec. 1.2.1). To control the sample flow rate through the AAC and resulting dilution ratio, HEPA filtered air was added downstream of the AAC to balance the flows. Three dilution ratios (0.3, 1.65, and

[2] when used in series with a electrostatic precipitator

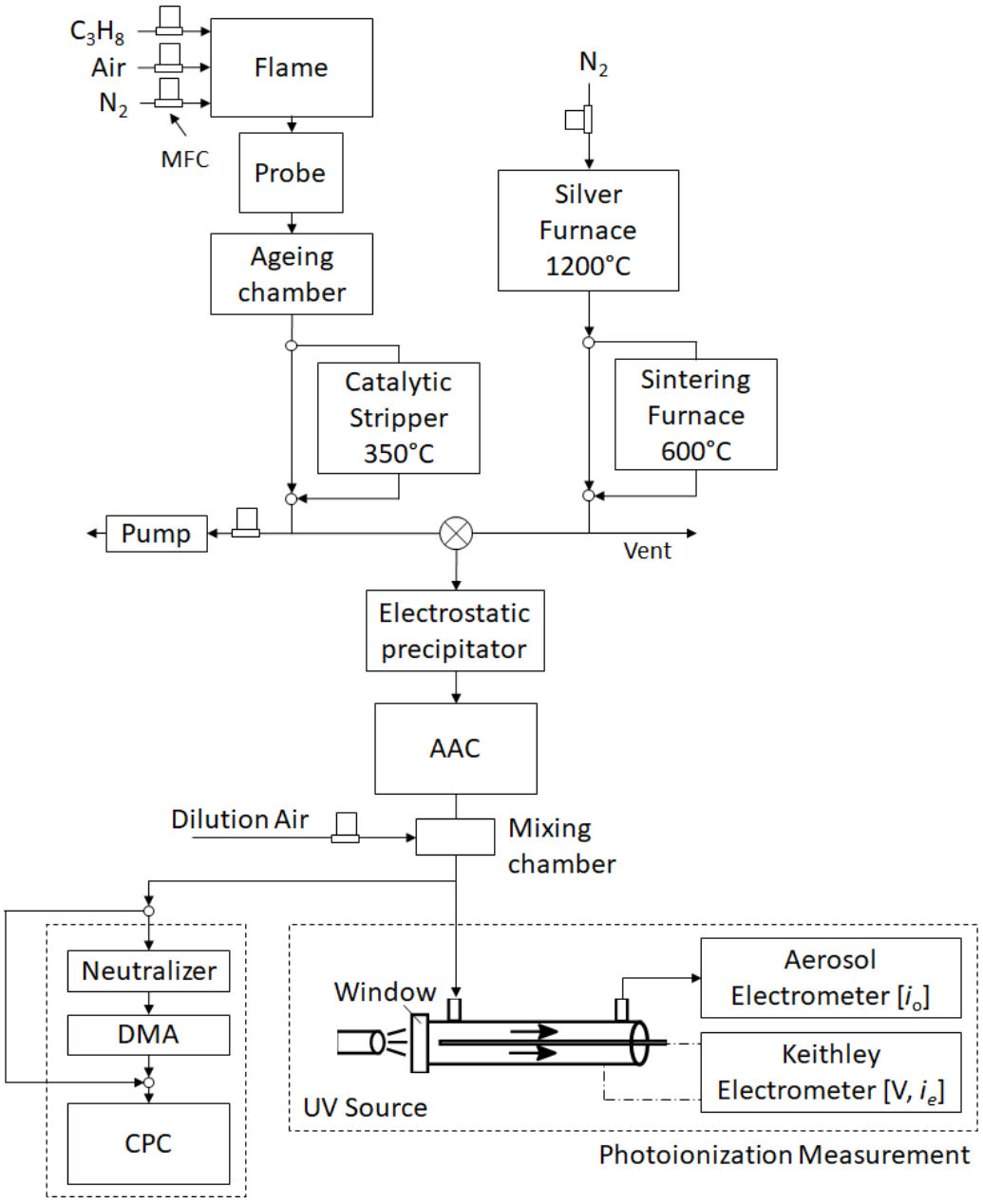

Fig. 3.4 Schematic of experimental apparatus for size-resolved photoionisation measurements using Aerodynamic Aerosol Classifier.

4.4) were used for both aerosol sources to provide a range of particle concentrations at each classified size, which was determined by the AAC setpoint. A mixing chamber was used to ensure the dilution air and sample flow were thoroughly mixed before entering the parallel measurement equipment.

The number-weighted particle mobility diameter distribution, allowing the particle Count Median Diameter (CMD) to be estimated, was measured with a Scanning Mobility Particle Sizer (SMPS; TSI Inc.: 3080 Electrostatic Classifier, Kr-85 Neutraliser, 3081 DMA, 3776 Condensation Particle Counter [CPC]) with two scans per AAC setpoint. Before and after the SMPS scans at each AAC setpoint, the neutraliser-DMA was bypassed and the total particle number concentration, N, was measured using the CPC. In parallel with the SMPS, the UV photoionisation chamber described in section 3.3.1 provided photoionisation measurements. A constant applied voltage of 30 V (24 V cm^{-1}) was chosen as it allows capture of highly mobile ions which are created from the photoemission process without significantly capturing the charged particles for the geometry and operating conditions.

Throughout the experimental set-up, stainless steel and conductive silicon tubing were used to minimise particle electrostatic losses in the sampling lines. System flow rates were verified using a bubble flow meter (Gilibrator 2, Sensidyne, LP, Clearwater, FL, USA).

3.3.4 Measurement uncertainty

Uncertainty in aerodynamic diameter for an AAC set-point is 4.7% based on the maximum average disagreement for spherical particles [110]. Uncertainty of the count median (mobility) diameter from the SMPS is 1% [111]. Concentrations were measured using the CPC with an uncertainty of 10% [112]. For data points where the direct CPC measurement was in photometric mode, the number concentration from the SMPS was used with an uncertainty of 10%, consistent with published values [113]. Vertical error bars were not included, because the standard error in measuring a current, i_o, was less than 1.5% for all but two data points using averages of measurements collected at 1 Hz for 30 s.

3.4 Closure

In this chapter, a novel photoionisation measurement design was described, followed by the numerical and experimental methods used to test the design under a range of conditions. The modelling techniques are applied in Chapter 4 to explore the dominant physical processes in ion and particle photoelectric charging and transport. The models are experimentally validated in Chapter 5 using the techniques described here. Then, the understanding gained

from modelling and experimental results are used to justify a re-evaluation of the concept of photoelectrically active area in Chapter 6.

Chapter 4

Evaluation of Modelling Techniques

4.1 Introduction

In this chapter, photoelectric charging, subsequent transport and collection of particles and ions in continuous flow are modelled as a means to evaluate photoionisation theory and provide tools for quantitatively evaluating charges carried by ultrafine particles.

4.1.1 Context

After the initial development of particle photoemission theory [59, 70, 81, 77], aerosol photoemission studies to date have largely focused on the experimental development of polycyclic aromatic hydrocarbon (PAH) sensors for industrial hygiene or combustion control [91, 93, 50, 94, 95, 99] or to study enhanced charging of nanoparticles below 20 nm diameter [62, 76, 96, 90, 64, 58, 66]. Modelling of the photoionisation process has not seen significant improvement since the application of the Fowler-Nordheim equation in a 0D case with recombination considered by Maisels et al. in 2003 [75, 80, 103].

4.1.2 Outline of chapter

In this chapter, a non-dimensional analysis is performed first to indicate regimes under which the photoionisation process is dominated by diffusion, electric field transport, convection, photoionisation, or recombination. In particular, the ratio of characteristic irradiation to recombination time defines the regime when charge saturation is reached. This is a function of particle size, concentration, material, and radiation wavelength and intensity. The physical processes of photoionisation and recombination of ions and particles are then modelled in 3D computational fluid dynamics (CFD) for the first time. The detailed terms obtained

in the 3D model in the charge balance equation are analysed to understand the range of validity of assumptions made for diffusional wall losses and external electric field in 0D analytical models. The effect of particle polydispersity on particle charging and transport is then explored to provide a simpler interpretation of ultrafine measurements. In each case, recommendations are made regarding the level of detail required for the prediction of aerosol charging and capture methods over a range of conditions used in experiments or the predictive design of photoemission-based devices.

4.2 Analytical modelling

The dominant physical processes in a photoionisation device may be explored with analytical modelling by simplifying the charging and transport equations. Part of the difficulty in solving the conservation equations comes from the non-linearity in the source terms. In the present work, a limiting case, first considered by Maisels et al. [75] is dealt with by again assuming that the charges per particle are large and positive. In that case, it is possible to neglect the image terms, and the combination coefficients of Eqs. 1.2 and 1.6 can be expressed, respectively, as:

$$\alpha^{q\to q+1} = \frac{K_c I}{h\nu}\frac{\pi d^2}{4}\left(h\nu - \Phi_\infty - \frac{2qV_e}{d}\right)^m \tag{4.1}$$

$$\beta^{q\to q-1} = 4\pi D_i \frac{V_e}{k_B T} q. \tag{4.2}$$

Further, the source terms of the conservation equations (Eqs. 3.4) can be approximated as moments in the charge distribution, in the limit of large number of charges per particle, so that the sums are replaced by a function of mean charge per particle $\overline{q}$, and total number of particles N, that is, $\overline{S}_\alpha = \sum_q \alpha^{q\to q+1} N_q = \overline{\alpha} N$, and $\overline{S}_\beta = -\sum_q \beta^{q\to q-1} N_q n_{-1} = -\overline{\beta} N n_{-1}$. An analytical solution can be obtained for the mean charge $\overline{q}N = \sum_q qN_q = n_{-1}$ for steady plug flow conditions with a constant total number concentration of particles N, where $\vec{u} = U\vec{e}_z$:

$$U\frac{\mathrm{d}n_{-1}}{\mathrm{d}z} = \overline{S}_\alpha + \overline{S}_\beta. \tag{4.3}$$

Maisels et al. [75] considered the limits to Eq. 4.3 for (a) zero recombination losses, so that $\overline{S}_\beta = 0$, and (b) steady-state conditions after a sufficient convection length (or time) under irradiation, where $\dfrac{\mathrm{d}n_{-1}}{\mathrm{d}z} = 0$. For the zero recombination case, the following applies

$$\begin{aligned} \overline{q}_{z\to 0} &= \frac{z}{U\tau_\alpha} = \frac{t}{\tau_\alpha} \\ \tau_\alpha &= \left[\frac{K_c I}{h\nu}\frac{\pi d^2}{4}\left(h\nu - \Phi_\infty\right)^m\right]^{-1} \end{aligned} \tag{4.4}$$

where the residence time is defined as $t = z/U$. The irradiation time, $\tau_\alpha = (\overline{S}_{\alpha,z\to 0})^{-1}$, is the inverse of the characteristic rate of photon generation, which is the product of the rate of absorption of photons by the particles, $\frac{1}{\tau_\nu} = \frac{I\pi d^2}{4h\nu}$, and the quantum yield at zero mean charge, $Y = K_c\left(h\nu - \Phi_\infty\right)^m$, where $\tau_\alpha = \tau_\nu / Y$. After a sufficient residence time under irradiation, τ_s, a steady-state mean charge state, $\overline{q}_s$, is found when either the extent of recombination equals that of photoionisation, as obtained from setting the left hand side of Eq. 4.3 to zero, so that $\overline{S}_\alpha + \overline{S}_\beta = 0$, or when the Coulomb limit is reached. Using $m = 2$ and expanding the brackets in Eq. 4.1, the mean steady-state charge can be obtained as:

$$\begin{aligned} \overline{q}_{t\to\infty} = \overline{q}_s &= q_{\max}\left(1 + \sqrt{\hat{A}_\nu}\right)^{-1} \\ \hat{A}_\nu &= \frac{4h\nu D_i N}{K_c I V_e k_{\mathrm{B}} T} \end{aligned} \tag{4.5}$$

where $q_{\max}$ is defined in Eq. 1.5. The term $\hat{A}_\nu$ represents the ratio of recombination over photoionisation and recombination must be considered when $\hat{A}_\nu \gg 0$. The full equation for the mean charge has been derived by Maisels et al. [75] as:

$$\overline{q} = q_{\max}\frac{\tanh\left(\dfrac{\sqrt{\hat{A}_\nu}}{q_{\max}\tau_\alpha}t\right)}{\tanh\left(\dfrac{\sqrt{\hat{A}_\nu}}{q_{\max}\tau_\alpha}t\right) + \sqrt{\hat{A}_\nu}}. \tag{4.6}$$

The square root term arises due to the factor $m = 2$, which leads to an expansion of the quadratic term in the solution of the differential equation.

4.2.1 Characteristic saturation time

By equating Eqs. 4.4 and 4.5 with each other, a characteristic charge saturation time is defined, τ_{s}, after which the photoionisation rate matches the recombination rate and maximum charging occurs:

Table 4.1 Characteristic times of the dominant physical processes in particle and ion charging and transport.

	Characteristic times (ions)	Characteristic times (particles)
Photoionisation	$\tau_{\mathrm{p,i}} = \dfrac{n_{-1}/N}{\overline{\alpha}}$	
Recombination	$\tau_{\mathrm{r,i}} = \dfrac{1}{\overline{\beta}N}$	
Diffusion	$\tau_{\mathrm{d,i}} = \dfrac{R^2}{4D_i}$	$\tau_{\mathrm{d,p}} = \dfrac{R^2}{4D_p}$
Electric field	$\tau_{\mathrm{e,i}} = \dfrac{R}{Z_i E}$	$\tau_{\mathrm{e,p}} = \dfrac{R}{Z_p E}$
Convection	$\tau_{\mathrm{c,i}} = \dfrac{L}{U}$	$\tau_{\mathrm{c,p}} = \dfrac{L}{U}$

$$\tau_{\mathrm{s}} = \frac{q_{\max}\tau_{\alpha}}{\left(1+\sqrt{\hat{A}_v}\right)}. \tag{4.7}$$

The characteristic time, τ_{s}, therefore represents a minimum residence time to reach maximum particle charging. In a steady plug flow situation with volumetric flow rate across an area, $Q = UA$, this implies a minimum volume $V_{\min} = Q\tau_s$ to reach maximum particle charging. The dimensionless mean charge per particle, $\overline{q}$, of Eq. 4.6 relative to the steady-state level, $\overline{q_s}$, of Eq. 4.5 is shown as a function of the relative charging time, t/τ_s, in Fig. 4.1, along with the limits from Eqs. 4.4 and 4.5 for the conditions outlined in Maisels et al. [75] and Table B.1[1]. The dimensionless mean charge level during the transition to steady-state does not differ significantly for concentrations $10^4 - 10^7$ cm^{-3}, when recombination is significant.

The mean charge is shown as a function of dimensional time and particle concentration in Fig. 4.2 for typical atmospheric particle concentrations. The mean charge per particle decreases with increasing concentration of particles due to the increased likelihood of recombination. The dashed lines in Figs. 4.1 and 4.2 are from Eqs. 4.4 and 4.5.

[1]Properties and operating conditions are summarised with the numerical verification section of Appendix B as specific conditions are more relevant to higher order modelling.

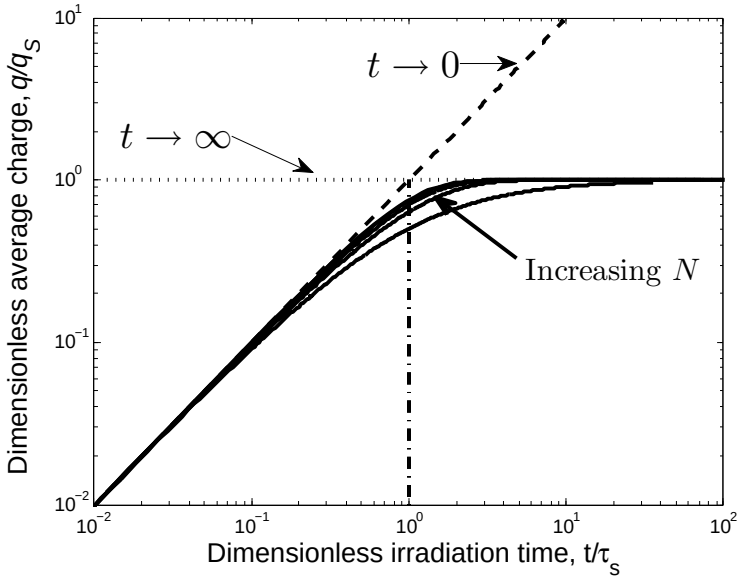

Fig. 4.1 Dimensionless mean charge per particle, $\overline{q}/\overline{q}_s$, as a function of dimensionless time, τ_c/τ_s for a range of concentrations.

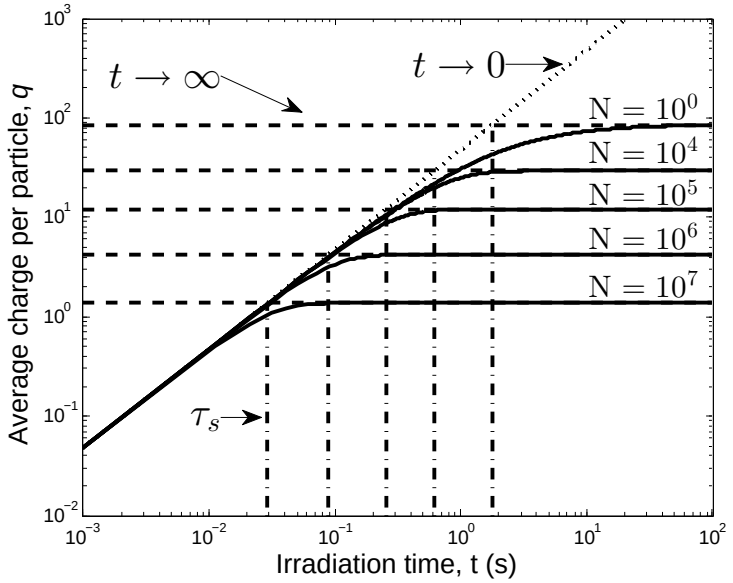

Fig. 4.2 Mean charge per particle, $\overline{q}$, as a function of time for a range of concentrations using Eqs. 4.4 and 4.5. Characteristic time to charge saturation, τ_s, is indicated by the vertical lines. The curved lines are generated from Eq. 4.6. Concentrations, N, given in [cm^{-3}].

4.2.2 Characteristic times and dimensionless parameters

The processes in this work are significantly influenced not only convection, charging and recombination, but also electric field transport and wall losses via diffusion. Therefore, it is useful to consider the characteristic times associated with the effect of each of the charging and transport mechanisms to identify which mechanisms are fast or slow for any given set of parameters. Characteristic times are defined for convection, τ_{c}, photoionisation, τ_{p}, recombination, τ_{r}, wall loss, τ_{w}, and electric field transport, τ_e, and are summarized in Table 4.1. For example, the ratio of characteristic times for ion wall loss due to electric field relative to the diffusional wall loss is:

$$\hat{\tau}_{\mathrm{ed,i}} = \frac{\tau_{\mathrm{d,i}}}{\tau_{\mathrm{e,i}}} = \frac{Z_{\mathrm{i}} E R}{4 D_{\mathrm{i}}}. \tag{4.8}$$

For $\hat{\tau}_{\mathrm{ed,i}} \ll 1$, ion capture at the walls due to electric field transport is slow relative to diffusional ion loss. For $\hat{\tau}_{\mathrm{ed,i}} \gg 1$, electric field transport is fastest and dominant. Similar relations can be used to determine the relative effect of diffusional loss of ions and particles, for example, crucial in determining operating conditions of a given device.

The total charge flow can be estimated by ratios of the different characteristic times at the limits of, for example, full charging, where $\tau_c > \tau_s$. The number rates and electric currents are shown in Table 4.2. For example, $i_{\mathrm{o,p}} = QN\overline{q}e$ gives the analytical limit estimate of the electric current available due to the flux of particles through the outlet, useful for a particle measurement device, while $i_{\mathrm{e,i}} = Q\overline{q}Ne\dfrac{\tau_{\mathrm{c,i}}}{\tau_{\mathrm{e,i}}}$ gives the corresponding magnitude of current due to the flux of trapped ions in an electric field during the photoionisation process. The effect of electric field strength on both currents, $i_{\mathrm{o,p}}$ and $i_{\mathrm{e,i}}$, is discussed in the next section using 0D numerical and 3D CFD models.

The dimensionless parameters give insight into the relative effects of particle and ion charging and transport mechanisms. They allow a simple estimation of particle and ion flux and electrical current due to the relative effects of convection, diffusional wall loss, and capture in an electric field. However, these estimates do not directly give the exact solutions for a given flow situation.

4.2.3 Effect of ion loss on particle charge state

Ions are less likely to recombine with particles if they are removed due to diffusional wall losses or electric field capture. Removing ions can significantly enhance particle charging [66]. The following describes a simplified analytical method for calculating diffusional

Table 4.2 Analytical estimates of particle and ion number rate and electrical current.[2]

	Ion		Particle	
	Number Rate $\left(\frac{\#}{s}\right)$	Electric Current [A]	Number Rate $\left(\frac{\#}{s}\right)$	Electric Current [A]
Outlet	$j_{\mathrm{o,i}} = Q\bar{q}N$	$i_{\mathrm{o,i}} = j_{\mathrm{o,i}}e$	$j_{\mathrm{o,p}} = QN$	$i_{\mathrm{o,p}} = j_{\mathrm{o,p}}\bar{q}e$
Diffusion	$j_{\mathrm{d,i}} = j_{\mathrm{o,i}}\frac{\tau_{\mathrm{c,i}}}{\tau_{\mathrm{d,i}}}$	$i_{\mathrm{d,i}} = i_{\mathrm{o,i}}\frac{\tau_{\mathrm{c,i}}}{\tau_{\mathrm{d,i}}}$	$j_{\mathrm{d,p}} = j_{\mathrm{o,p}}\frac{\tau_{\mathrm{c,p}}}{\tau_{\mathrm{d,p}}}$	$i_{\mathrm{d,p}} = i_{\mathrm{o,p}}\frac{\tau_{\mathrm{c,p}}}{\tau_{\mathrm{d,p}}}$
Elec. field	$j_{\mathrm{e,i}} = j_{\mathrm{o,i}}\frac{\tau_{\mathrm{c,i}}}{\tau_{\mathrm{e,i}}}$	$i_{\mathrm{e,i}} = i_{\mathrm{o,i}}\frac{\tau_{\mathrm{c,i}}}{\tau_{\mathrm{e,i}}}$	$j_{\mathrm{e,p}} = j_{\mathrm{o,p}}\frac{\tau_{\mathrm{c,p}}}{\tau_{\mathrm{e,p}}}$	$i_{\mathrm{e,p}} = i_{\mathrm{o,p}}\frac{\tau_{\mathrm{c,p}}}{\tau_{\mathrm{e,p}}}$

wall loss or electric field capture of ions to determine if ion loss has a significant effect on particle charge state.

Equations 1.8a and 1.8b may be rearranged assuming no particle wall losses and plug flow conditions, where $\vec{u} = U\vec{e}_z$:

$$U\frac{\mathrm{d}}{\mathrm{d}z}\left(\bar{q}N - n_{-1}\right) = +\frac{4D_i}{R^2}n_{-1} + \frac{Z_j E}{R}n_{-1}. \tag{4.9}$$

Integration of Eq. 4.9 followed by linearisation, due to small diffusion and electric field terms, yields $\bar{q}N = n_{-1}\left(1 + \hat{B}_v + \hat{C}_v\right)$, where the terms $\hat{B}_v$ and $\hat{C}_v$ are given as

$$\hat{B}_v = \frac{\tau_c}{\tau_{\mathrm{d,i}}} = \frac{4D_i}{R^2}\tau_c, \tag{4.10a}$$

$$\hat{C}_v = \frac{\tau_c}{\tau_{\mathrm{e,i}}} = \frac{Z_{-1}E}{R}\tau_c \tag{4.10b}$$

where $\tau_{\mathrm{d,i}}$ and $\tau_{\mathrm{e,i}}$ are the characteristic times for diffusional wall loss and electric field loss, respectively. Parameters $\hat{B}_v$ and $\hat{C}_v$ represent the fraction of ions lost due to diffusion and electric field transport over time, respectively, valid for Poiseuille flow in a cylindrical geometry. The diffusion and electric field loss terms are assumed to be small, so that n_{-1} is taken as identical to that of the steady-state solution $n_{-1,0} = \bar{q}_0 N$ obtained in Eq. 4.5. The corrected mean particle charge is obtained for $\tau_c > \tau_s$, assuming τ_s is small:

[2]Number rate defined as a particle or ion number flux multiplied by area through which flux occurs. Flux defined as per unit area according to Bird et al. [114]

$$\overline{q} = q_{\max} \left(1 + \sqrt{\frac{\hat{A}_v}{1 + \hat{B}_v + \hat{C}_v}} \right)^{-1} . \tag{4.11}$$

The assumption of small ion losses and no particle losses is valid for low levels of wall loss relative to the number of remaining ions, n_{-1}.

If diffusional loss or electric field capture of ions is significant, that is $\hat{B}_v \gg 0$ or $\hat{C}_v \gg 0$, a numerical model is recommended. If $\hat{B}_v \approx 1$ or $\hat{C}_v \approx 1$ or higher, ion capture is of the same order as the remaining ion flux, therefore the present linear approximation breaks down and a numerical or CFD model must be implemented. To determine if wall loss has a significant effect on the particle charge level, Eq. 4.11 may be solved with and without the effect of wall loss. For example, the ratio of mean particle charge with wall losses relative to recombination, $\hat{B}_r$, is defined as follows:

$$\hat{B}_r = \frac{1 + \sqrt{\hat{A}_v}}{1 + \sqrt{\dfrac{\hat{A}_v}{1 + \hat{B}_v}}} = \frac{\overline{q}\ \text{(recomb + wall loss)}}{\overline{q}\ \text{(recomb)}} \tag{4.12}$$

where the total residence time is a function of flow rate and geometry. Analogous parameters are summarized in Table 4.3 for the effects of electric field loss and photoionisation on the mean particle charge level, $\overline{q}$. For $\hat{A}_r \approx 1$, recombination may be neglected, for $\hat{B}_r \approx 1$, wall loss may be neglected, and for $\hat{C}_r \approx 1$, electric field losses may be neglected. The effects of recombination, diffusional wall loss, and electric field capture relative to photoionisation can be estimated by the ratio of $\hat{B}_r$ or $\hat{C}_r$ to $\hat{A}_r$.

A comparison of the analytical model described above with the solution of the numerical, 0D equations is shown in Figure 4.3. The mean steady-state charge per particle in Eq. 4.11 decreases with increasing concentration of particles owing to an increase in recombination. The 0D numerical model follows the work by Maisels et al. [75, 80] and from Appendix B, and does not require the assumption of large charges for the mean charge approximation, instead solving for the concentration of each discrete charge state, q. The analytical model described begins to deviate from the 0D numerical model when recombination is high enough to reduce mean charge per particle to +1 mean charge per particle. However, for charge levels above +1 mean charge per particle, the analytical and numerical models agree. Recombination must be included at concentrations above around $N = 1 \times 10^2$ cm^{-3} for the present conditions. Figure 4.3 also shows an increase in steady-state charges per particle with logarithmically increasing electric field strength ($0.008 < E < 0.8$ V cm^{-1}) according to

Table 4.3 Dimensionless parameters for the effect of photoionisation and ion loss on mean charge state.

	Parameter	Effect on charge state relative to recombination
Photoionisation	$\hat{A}_v = \dfrac{4h\nu D_i N}{K_c I V_e k_\mathrm{B} T}$	$\hat{A}_r = 1 + \sqrt{\hat{A}_v}$
Diffusion	$\hat{B}_v = \dfrac{\tau_{\mathrm{c,i}}}{\tau_{d,i}}$	$\hat{B}_r = \dfrac{1 + \sqrt{\hat{A}_v}}{1 + \sqrt{\dfrac{\hat{A}_v}{1+\hat{B}_v}}}$
Electric field	$\hat{C}_v = \dfrac{\tau_{\mathrm{c,i}}}{\tau_{\mathrm{e,i}}}$	$\hat{C}_r = \dfrac{1 + \sqrt{\hat{A}_v}}{1 + \sqrt{\dfrac{\hat{A}_v}{1+\hat{C}_v}}}$

Eq. 4.11. While Fig. 4.3 shows the increasing effect of the electric field on q, the assumptions in the analytical solution for the electric field are no longer valid for electric fields stronger than $E \approx 0.15$ V cm^{-1} which corresponds with $\hat{C}_v = 0.75$ in this case.

4.2.4 Limitations of analytical model

The formulations of the analytical equations and dimensionless parameters assume a large, positive number of charges per particle and low ion wall losses relative to ion concentration. The main assumption within the charging equation (Eq. 4.1) is that the image charge has a negligible effect. This is true during the low charging regime $\overline{q} \gg 1$, otherwise the effect of image charge is significant and must be included. The main assumption in the recombination equation (Eq. 4.2) is that the charge level of the particle dominates the electrostatic attraction and the image force can be neglected. This is true for $\overline{q} > 1$. In reducing the governing equations of Eq. 1.8 to the ion conservation in Eq. 4.3, large, positive charges per particle must be assumed. The assumptions that n_{-1} is constant in the integration of Eq. 4.9 and that the ion losses are small in the formulation of Eq. 4.11 are no longer valid at high levels of wall loss relative to the remaining ions.

Although the analytical model is useful in thinking through the processes involved, and in quick calculations, numerical models are necessary to solve the conservation equations whenever the assumptions used in their derivation are violated, and losses are no longer linear.

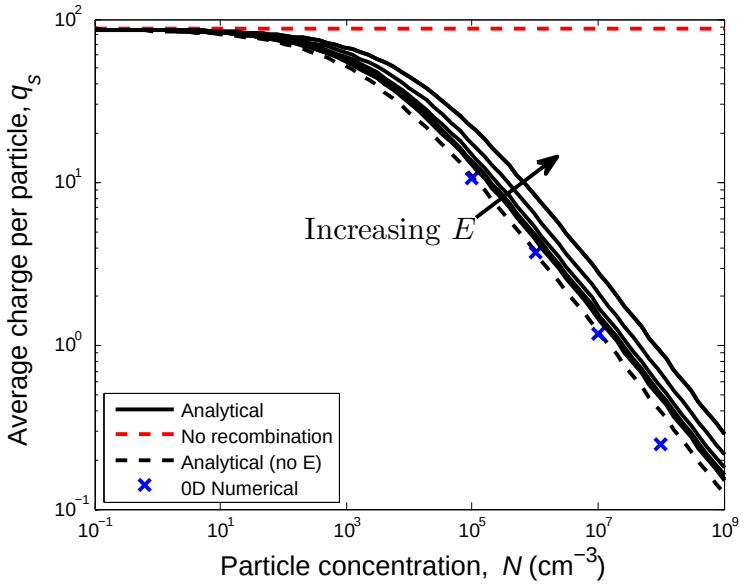

Fig. 4.3 Steady-state charge for a monodisperse, single-component aerosol as a function of concentration. Logarithmically increasing electric field strength ($0.008 < E < 0.8$ V cm^{-1}).

4.3 Numerical modelling an aerosol's transport in an electric field

Equations for UV photoionisation and ion-particle recombination are coupled with ion/particle convection and diffusion and electric field transport in three-dimensional CFD as described in Section 3.2. Upwards of one hundred simultaneous species transport equations can be solved if necessary to allow the resolution of local charge distribution in a particle size distribution. To determine the modelling capabilities required to capture the physical process, results from the three-dimensional equations are compared with results from their equivalent zero-dimensional (0D) form assuming steady-state, plug flow and linear electric field and diffusion loss terms. The form of the 3D and 0D numerical equations are shown in Table A.1.

4.3.1 Model properties and operating conditions

In this section, neutral particles of monodisperse size are considered at the inlet of the photoionisation chamber, therefore, particles of a single size bin, b, are considered in the particle conservation equation (Eq. 3.4a). The photoionisation process is assumed to take place as a uniform volumetric source throughout the cylinder, increasing the charges per particle. The assumption of uniform light intensity is an idealisation of a chamber without geometric effects or attenuation, such as by application of collimated light with negligible

volumetric absorption. The model parameters and operating conditions are summarised in Table 4.4. Based on a test of grid independence, the computational mesh in this section consists of 230,400 cells which are graded near walls where the highest concentration gradients occur.

Table 4.4 Model properties and operating conditions used to explore the effect of electrical field transport and capture of ions and particles.

Parameter	Symbol	Units	Value
Negative ion diffusivity [105]	D_{-1}	$m^2\ s^{-1}$	4.04×10^{-6}
Negative ion electrical mobility [105]	Z_{-1}	$m2\ V^{-1}\ s^{-1}$	1.6×10^{-4}
Mean particle diameter	d	nm	20
Particle concentration	N	cm^{-3}	10^6
Flow rate	Q	std L min^{-1}	1
Bulk velocity	U	$m\ s^{-1}$	3.45×10^{-2}
Convection time	τ_c	s	5.8
Empirical constant	m		2
Photoemission constant	K_cI	$J^{-1}\ m^{-2}\ s^{-1}$	1.9×10^{35}
Light energy	hv	eV (nm)	6.69 (185)
Work function	Φ_∞	eV	4.95

4.3.2 Analysis

Equations for photoionisation, recombination and transport of ultrafine particles are solved for continuous flow through a cylindrical chamber using 0D numerical and CFD models. For the conditions outlined in Table 4.4, with no electric field, the particles are clearly saturated with charge as $\tau_c = 5.8\ s > \tau_s = 1\ s$, and recombination is a dominant flux, as $\hat{A}_r = 10.9$. Diffusional ion wall loss is significant, as $\hat{B}_r = 1.24$ at zero bias voltage. Above around 0.25 V (0.2 V cm^{-1}), the electric field capture of ions is of the same order as the remaining ions, since at that voltage, $\hat{C}_v = 0.9$. This regime requires a numerical or CFD model to quantify the effects of ion capture on particle charging.

Figure 4.4 shows a two-dimensional (2D) slice of the computational domain where particles are flowing in the positive z-direction and a voltage of 1 V (0.8 V cm^{-1}) is applied between the top and bottom electrodes. The concentration of ions of -1 charge and total particle concentration are shown for an inlet concentration of 10^6 cm^{-3} neutral particles of 20 nm diameter. The ions generated during the photoemission process are transported and captured at the top, positive electrode and the charged particles are transported towards the bottom, negative electrode. Each remaining 2D slice shows the concentration of particles at a given mean charge, q, from 0 to 6 charges per particle. Particles are charged to higher

charge levels as the flow proceeds in the z-direction while the particles are simultaneously transported to the bottom, negative electrode. The particles near the inlet are held at lower charge levels at 1 or 2 charges per particle due to the presence of ions in those areas.

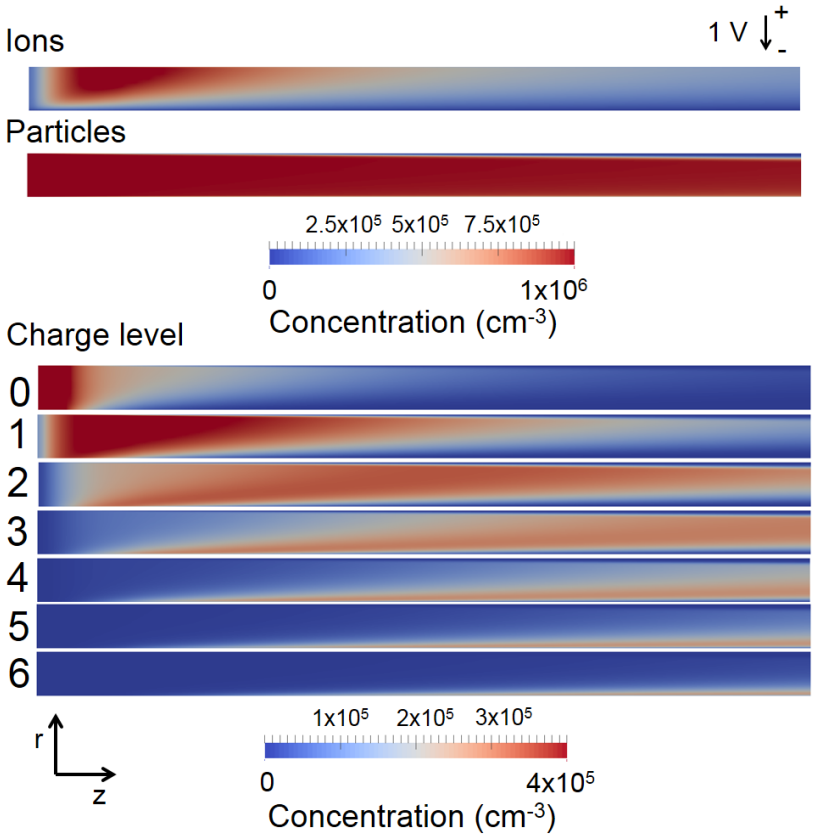

Fig. 4.4 (Top two panels) Steady-state concentration of total ions, n_{-1}, generated from photoionisation of particles, N, across half-symmetry plane for the domain. (Bottom seven panels) Corresponding number concentration of particles with charge levels from 0 to 6. Operating conditions are: inlet velocity of 0.0345 m s^{-1} in the +z direction, particle inlet concentration of $N = 10^6$ cm^{-3}, neutral particles with a monodisperse diameter of 20 nm. A voltage of 1 V is applied between the top (cylinder) and bottom (rod) electrode.

A positive bias voltage indicates that the outer cylinder has a positive potential relative to the rod, and the reverse is true for a negative bias voltage. For a range of bias voltages, the total current, i_e, is calculated from the total (diffusive) flux of ions and particles integrated at the interface of the rod and outer cylinder walls. The outlet current, i_o, is also calculated from the total (diffusive plus convective) flux of positively plus negatively charged ions passing through the outlet, multiplied by their respective charges.

The results for the 0D numerical model and 3D CFD model with positive and negative biases are shown in Fig. 4.5. At bias voltages around 1 V (0.8 V cm^{-1}), only the highly

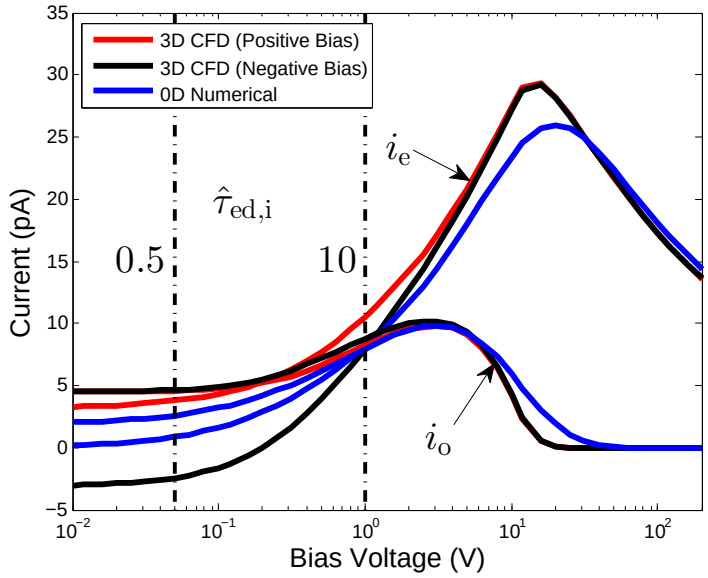

Fig. 4.5 Ion and particle current, i_e, and outlet current, i_o, as a function of applied bias voltage for numerical and CFD models. A positive bias indicates outer cylinder is at a positive voltage relative to rod, and the converse for negative bias.

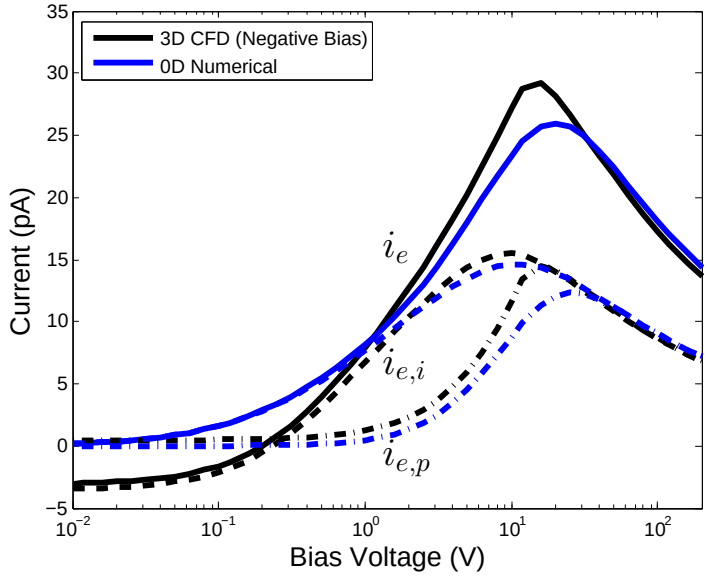

Fig. 4.6 Ion and particle current, i_e, made up of the sum of ion current, $i_{e,i}$, and particle current, $i_{e,p}$, as a function of applied bias voltage for numerical and CFD models.

mobile ions are transported to either the rod or cylinder electrodes leaving less opportunity to recombine with the charged particles, and resulting in higher currents for both i_e and i_o. Every positive charge on a particle creates an equal and opposite charge on a negative ion, therefore at voltages around 1 V (0.8 V cm^{-1}), i_e and i_o are of equal magnitude. As the bias voltage increases above approximately 2.5 V (2 V cm^{-1}), the flux of charged particles near the rod or outer cylinder begins to dominate, thereby decreasing the outlet current, i_o. The current, i_e, continues to increase as the negatively charged ions are collected at the rod and positively charged particles are collected at the outer cylinder, both contributing to current i_e as shown in Fig. 4.6. The numerical model does not capture the differences between a positive and negative bias. At low, negative bias voltage, below around 1 V (0.8 V cm^{-1}), ions preferentially diffuse to the outer cylinder rather than the centre rod due to the difference in electrode surface area creating an effective current. At low bias voltage, ion diffusion is faster than the electric field flux. At 0.05 V (0.04 V cm^{-1}), the calculated ratio of characteristic times in Eq. 4.8, $\hat{\tau}_{ed,i} = 0.5$, whereas at 1 V $\hat{\tau}_{ed,i} = 10$ and the electric field flux dominates.

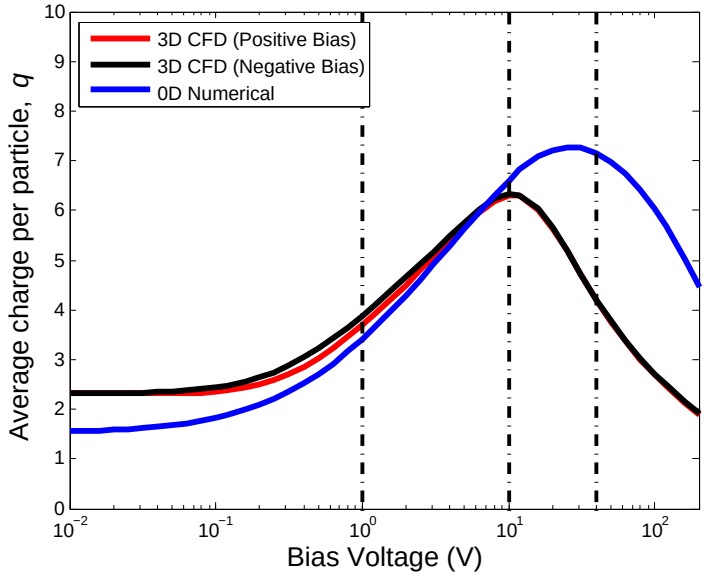

Fig. 4.7 Mean charge per particle at outlet as a function of bias voltage for numerical and CFD models. The dotted lines mark the voltages at which the charge distributions are presented in Fig. 4.8.

The mean charge per particle and charge distribution at the outlet are shown in Fig. 4.7 and Fig. 4.8, respectively, as a function of bias voltage. Particle charge levels can be controlled by changing the bias voltage, thus inducing more or less direct removal of ions from the control volume, resulting in correspondingly different opportunity for recombination. At

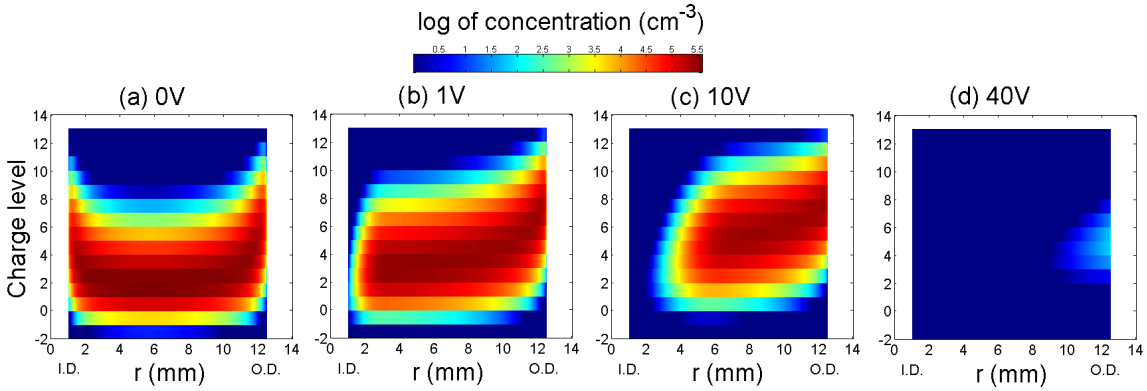

Fig. 4.8 Charge distribution of discrete particle charges at the chamber outlet as a function of radial distance from the centreline at four different voltages; (a) 0 V, (b) 1 V, (c) 10 V, and (d) 40 V between the rod (I.D., positive electrode) and cylinder (O.D., negative electrode).

high voltages, charged particles as well as ions can be removed, thereby changing the charge distribution and mean charge at the outlet. In these cases, the mean charges can be controlled between 2 and 7 charges per particle. At low bias voltages, below around 1 V (0.8 V cm^{-1}), the calculated local charge per particle using the 3D CFD model increases significantly nearest the walls where the highest diffusion loss of ions occurs as shown in Figs. 4.8a and b. As a result, the rate term of the 0D numerical model does not adequately capture the effect of diffusional ion loss on mean charge per particle at low bias voltages. At bias voltages from 1 V (0.8 V cm^{-1}) to 10 V (8 V cm^{-1}), ions are captured quickly, particles reach higher charge states and are transported towards the negative electrodes as seen in Figs. 4.8b and c. At high bias voltages, above around 10 V (8 V cm^{-1}), highly charged particles localised near the negative electrode are captured more readily by the applied electric field as seen in Fig. 4.8d, leading to a lower mean charge per particle at the outlet and higher electrode current, i_e, relative to the 0D numerical model. The latter does not solve local charge levels, but rather a rate term for the electric field capture as described in Table A.1 of Appendix B. Without a local resolution of charge levels, the 0D numerical model cannot adequately capture the current or particle charging at low and high bias voltage conditions.

4.3.3 Summary

The computational fluid dynamics (CFD) model developed in this work is the first to include equations capturing UV photoionisation and detailed ion and particle recombination theory. The 0D numerical and 3D CFD models agree well for a large range of electric field strengths for the simple geometry of concentric cylinders, but differences appear at both high (above $\approx$8 V cm^{-1}) and low (below $\approx$0.8 V cm^{-1}) electric field strengths, where the detailed spatial

resolution rather than a simple linear 0D model becomes necessary. The 0D numerical and 3D CFD results both demonstrate that the mean particle charge level, and the resulting charges at the electrodes and ends of the system can be controlled by changing the bias voltage. These features can be used in the development of a particle discrimination and measurement system, and will be explored further in subsequent chapters.

4.4 Numerical modelling of the effect of aerosol polydispersity

Low-cost ultrafine aerosol sensors are experimentally calibrated with controlled aerosol sources to provide metrics such as surface area, lung-deposited surface area, mean particle size and/or total concentration from one or more electrical current measurements. However, an aerosol with a large standard deviation in particle size provides a significantly different signal from a monodisperse aerosol with the same median particle size. Therefore, further understanding of the effect of polydispersity during unipolar charging is required to improve the accuracy of low-cost sensors.

This section quantifies the effects of aerosol particle polydispersity on electrical currents resulting from photoelectric charging and ion-particle recombination in a photoionisation measurement system. A numerical model for charging and transport is demonstrated which considers the coupling between ion concentration and particle concentrations from each of the discrete size bins which make up polydisperse particle size distributions. The results are compared with those from a model assuming a monodisperse particle distribution at a representative particle diameter. The numerical simulations are used to predict the electrical signal from photoionisation measurements for a range of input particle size distributions and operating conditions.

4.4.1 Theory

Aerosols are characterised by different geometric parameters and the method of characterisation depends on which quantities are measurable. Even controlled aerosols come in a range of particle sizes, and it is intractable to measure the geometric properties of each particle individually. It is thus often convenient to describe the mean geometric properties by the p-th moments in its marginal size probability distribution $f(d)$,

$$(d_{\bar{p}})^p = \int_0^\infty f(d)\, d^p \, \mathrm{d}d \tag{4.13}$$

$$(d_{\bar{p}})^p \approx \frac{\sum^b (N_b d_b^p)}{N} \tag{4.14}$$

$$d_{\bar{p}} \approx \left(\frac{\sum^b (N_b d_b^p)}{N} \right)^{1/p} \tag{4.15}$$

where N_b is the concentration of particles at particle size d_b, N is total concentration, and p is the exponent, or moment, of diameter. A higher moment yields a higher moment average, $d_{\bar{p}}$. The count mean diameter, $\bar{d} = d_{\bar{1}}$, is found for $p = 1$, and the diameter of the average surface, $d_{\bar{s}} = d_{\bar{2}}$, for $p = 2$, using notation from Hinds [1].

A lognormal distribution of particle concentration as a function of size applies to most single source aerosols which are dominated by collisional growth. The lognormal distribution based on particle count is commonly characterised by a count median diameter, CMD$\approx \exp(\sum^b (N_b \ln d_b)/N)$, and geometric standard deviation, $\sigma_g \approx \exp(\sum^b N_b (\ln d_b - \ln \mathrm{CMD})^2/(N-1))$. The CMD of a lognormal count distribution is the geometric mean diameter and should not be confused with the (arithmetic) count mean diameter, $\bar{d}$, where by definition, CMD $< \bar{d} < d_{\bar{s}}$. Figure 4.9 shows $d_{\bar{s}}$ for two aerosols with different σ_g, but the same CMD and total concentration. By characterizing an aerosol with only count median diameter and total concentration, the polydispersity is neglected. For a lognormal size distribution the p-th moment diameter can be reckoned from CMD and σ_g as [1]:

$$d_{\bar{p}} = \mathrm{CMD}\ \exp(\frac{p}{2} \ln^2 \sigma_g) \tag{4.16}$$

Measurements made with monodisperse aerosol sources show that the electrical current measured from photoelectric charging charging scales approximately with $i \sim Nd^2$ [101, 47, 46, 50, 49]. The relation is grounded in theory, as demonstrated analytically in Eq. 4.4 for monodisperse particles subject to assumptions such as neglecting the effects of size dependent particle losses and secondary charging and transport processes [46].

The total electrical current obtained from a polydisperse particle distribution is composed of the integral sum of the contribution from each monodisperse particle size bin. The induced current is proportional to the second moment of the size distribution determined using Eq. 4.13, for photoelectric charging. For a polydisperse aerosol made up of a number of individual, monodisperse bins, b, of particle size, d_b, this results in

$$i \sim \sum^b (N_b d_b^p) = N d_{\bar{p}}^p \tag{4.17}$$

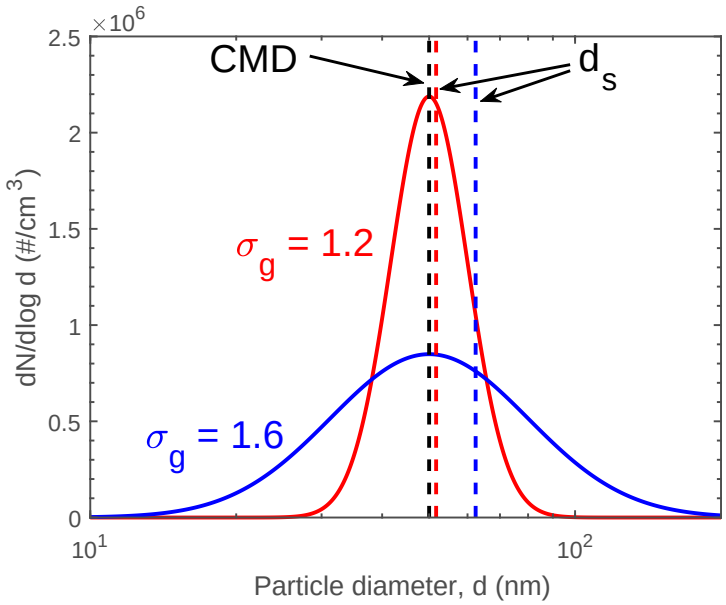

Fig. 4.9 Two particle size distributions with the same CMD (50 nm) and total concentration ($N = 10^6$ cm^{-3}) with different standard deviations, $\sigma_g = 1.2$ (red) and $\sigma_g = 1.6$ (blue). The diameter of the average surface, $d_{\bar{s}}$, is shown for each distribution.

where $p = 2$ for photoelectric charging. Considering a range of charging and transport effects, the total electrical current as a function of particle diameter and concentration may not be demonstrated analytically, therefore, in this section, a numerical model is used to show that the moment average diameter can be used to simplify the charging and transport equations for a large range of conditions.

4.4.2 Properties and operating conditions

Table 4.5 Photoelectric charger model parameters and operating conditions.

Parameter	Symbol	Units	Value
Negative ion diffusivity	D_{-1}	m^2 s^{-1}	4.3×10^{-6}
Negative ion electrical mobility	Z_{-1}	m^2 V^{-1} s^{-1}	1.7×10^{-4}
Flow rate	Q	std L min^{-1}	1.5
Bulk velocity	U	m s^{-1}	5.17×10^{-2}
Residence time	t	s	3.86
Empirical constant	m		2
Light energy	$h\nu$	eV (nm)	6.69 (185)
Work function	Φ_∞	eV	4.95

The 3D CFD model used in this section is described in Section 3.2. In this section, the non-collimated light intensity decreases with the inverse square law in the flow direction and the product $K_c I$ is fixed at the inlet, 2 cm from the light source. The particle's work function, Φ_∞, for carbon particles was extracted from Michaelson [82]. A summary of the properties is given in Table 4.5 and operating conditions in Table 4.6.

4.4.3 Variation of parameters

Table 4.6 Range and spacing of variable parameters for modelling typical aerosol and operating conditions.

Variable	Units	Baseline	Min.	Max.	Spacing	# Pts.
Input Aerosol						
Standard deviation, σ_g	-	1.7	1.1	1.9	Linear	5
Count median diameter, CMD	nm	50	30	200	Logarithmic	5
Particle concentration, N	cm^{-3}	10^6	10^4	10^7	Logarithmic	4
Photoelectric charging						
Photoemission constant, $K_c I$	$J^{-1}\ m^{-2}\ s^{-1}$	10^{34}	10^{33}	10^{35}	Logarithmic	5
Diameter of average surface, $d_{\bar{s}}$	nm	66	40	265	calc'd	5

Results from polydisperse particle size distributions represented by multiple size bins are compared with those using a single monodisperse size bin at a corresponding mean particle size and total concentration for each of the diffusional charging and photoelectric charging systems. Electrical current at the outlet, i_o, relevant to low-cost measurement devices is compared for parameters varied through a range of aerosol properties expected in-field: standard deviation, σ_g, count median diameter, CMD, and total particle concentration, N. The amount of charging was varied using the empirical constant, $K_c I$. The parameter variation includes a set of baseline conditions around which each parameter is varied individually. Sixteen simulations are performed at each of three size distribution resolutions (1, 8, and 16 bins) for a total of 48 simulations. Table 4.6 shows the range of input values varied either linearly or logarithmically throughout the range for each parameter.

A monodisperse particle size used to represent each evaluated polydisperse distribution is calculated at the diameter of the average surface, $d_{\bar{s}}$, using Eq. 4.16. The conditions presented here are restricted to lognormal particle size distributions assumed in each case which is generally representative of single-source aerosols, though the moment average diameter may be calculated using Eq. 4.13 for other polydisperse distributions.

4.4.4 Numerical comparison and computation times

The maximum charge state is selected as sufficiently high to ensure the concentration of particles at the highest charge state is negligible. In this section, the maximum charge state is set to +38 giving a total of 44 charge states. Solution time is a function the number of simultaneous equations to be solved, which is determined by the range of charge states and the number of particle size bins ranging from approximately one minute for monodisperse simulations to one hour for polydisperse simulations with 16 particle size bins.

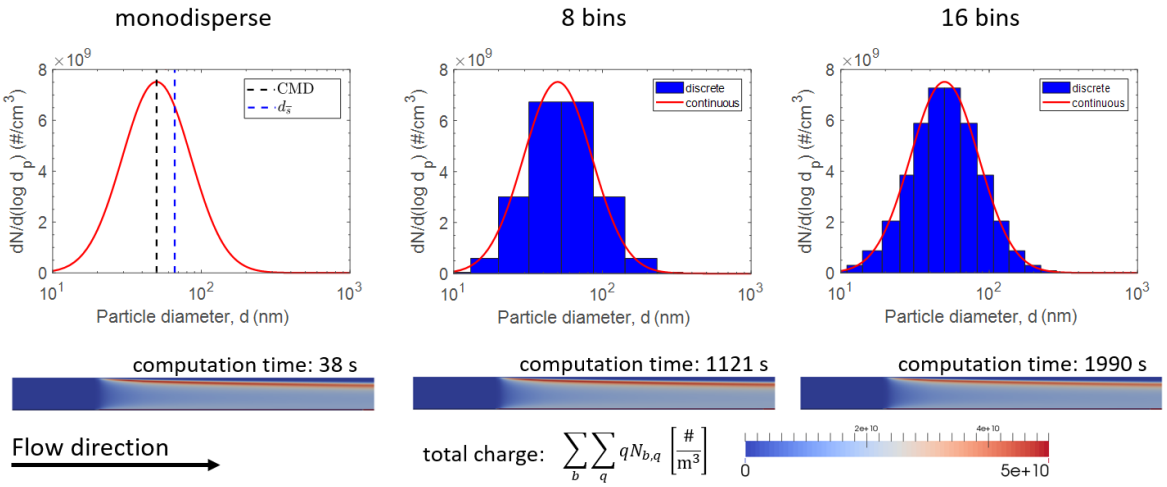

Fig. 4.10 Lognormal particle size distribution represented by a single size bin at the diameter of the average surface, $d_{\bar{s}}$, 8 size bins, and 16 size bins for baseline operating conditions of Table 4.6. The total charge, $\sum_b \sum_q N_{b,q} q$, is shown for a slice of the geometry along with computation time.

Numerical results using the baseline aerosol lognormal distribution and operating conditions of Table 4.6 are shown in Fig. 4.10[3]. The lognormal distribution is represented by a single, monodisperse size bin at the diameter of the average surface, $d_{\bar{s}}$, and 8 or 16 size bins. Visualisations of the total charge throughout a slice of the geometry are shown to be equivalent for each calculation method. For the baseline case, the calculation time for 8 bins and 16 bins is approximately 29 and 52 times that of the particle distribution represented by 1 bin. Median and mean computation times for the 16 sets of operating conditions of Table 4.6 are shown in Table 4.7. Resolving the local charge states for a polydisperse distribution made up of multiple individual size bins significantly increases the computation time over that of a single size bin. The calculation time for 8 bins and 16 bins is approximately 31 and 57 times that of the particle distribution represented by 1 bin.

[3]Figure 4.10 data gathered and formatted by Mario Schriefl (TU Graz, Austria)

Table 4.7 Comparison of simulation times which are presented as the median and mean times for the 16 different operating conditions of Table 4.6.

Polydisperse size bins	Simultaneous Conc. Eqs.	Computation time		
		Median [s]	Mean [s]	Mean increase
1	44	38	63	1×
8	352	1121	2645	31×
16	704	1990	5040	57×

The cases with 8 or 16 size bins each require approximately five times more computation time per computational cell and equation solved than that of the single size bin due to the significant coupling between the population of ions generated during photoemission and the rate of ion-particle collisions in each size bin and charge state. For photoelectric charging, the ion concentration must be considered as strongly dependent on the particle charge distributions and vice versa.

4.4.5 Count Mean Diameter vs. Count Median Diameter

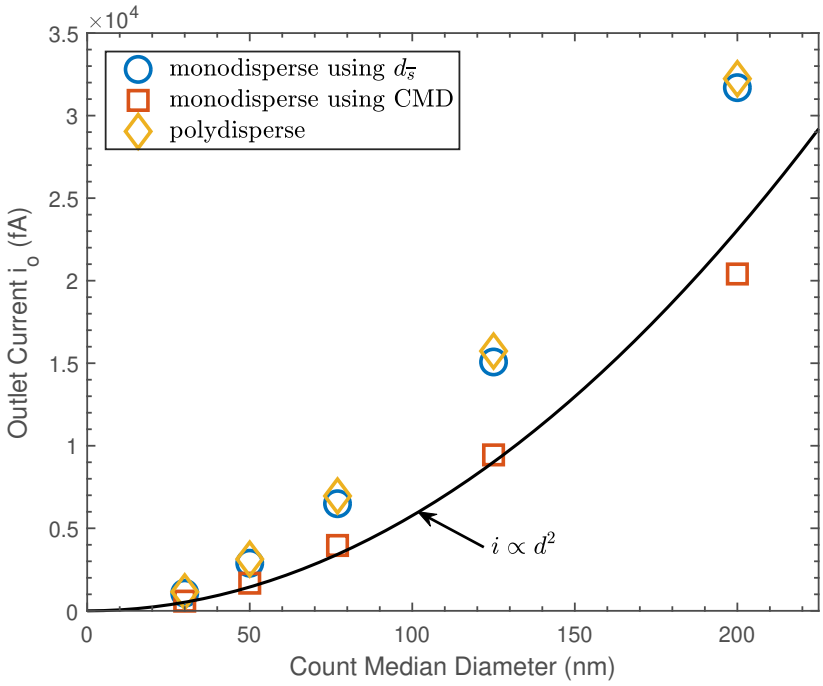

Fig. 4.11 Outlet current, i_o, as a function of the CMD for the polydisperse simulation with $N_{bin} = 8$, in comparison with monodisperse results using CMD and diameter of the average surface, $d_{\bar{s}}$, at baseline conditions.

Simulations were performed for polydisperse size distributions represented by the count median diameter, diameter of the average surface, and 8 particle size bins for 5 different count median diameters, logarithmically spaced (30, 50, 77, 125 and 200 nm). The count mean diameter was calculated according to Eq. 4.16 using the baseline conditions of Table 4.6. Results shown in Fig. 4.11 confirm the polydisperse distribution may be represented by the diameter of the average surface, $d_{\bar{s}}$, at the same total concentration to estimate electrical current, i_o, whereas the CMD is not representative. Figure 4.11 shows that the electrical current from the photoelectric charger is nearly proportional to CMD raised to the power of two. Using the CMD as a size input for the monodisperse simulation causes significant deviations from polydisperse results, showing an increasing underestimation of electrical current with particle size. The error when using CMD as the size input increases with standard deviation and the maximum relative error was found to be 45%

4.4.6 Accuracy in output current

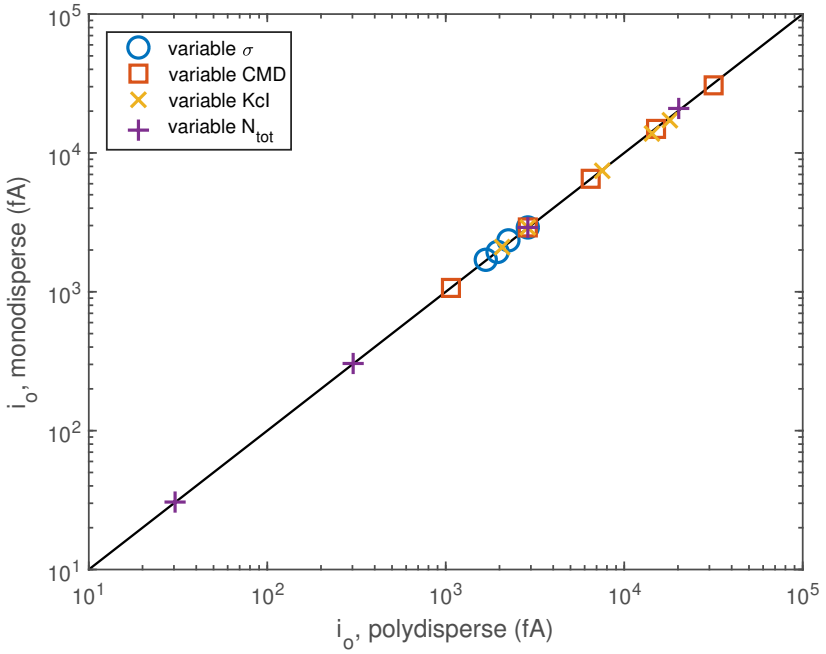

Fig. 4.12 Outlet current, i_o, from monodisperse particles with diameter, $d_{\bar{s}}$, as a function of output current from polydisperse particle distributions with $N_{\text{bin}} = 16$.

Numerical results with input aerosol parameters and operating conditions of Table 4.6 are shown in Fig. 4.12. Electrical current at the outlet, i_o, is shown for a monodisperse aerosol using the diameter of the average surface compared with i_o from the polydisperse distribution represented by 16 size bins. Simulations with 44 charge states requires 704 coupled charge

conservation equations to be computed for polydisperse cases with 16 bins, whereas only 44 charge conservation equations are required for monodisperse distributions. For the range of conditions in Table 4.6, the maximum percent difference in outlet current between the particle size distribution represented by 16 size bins and the distribution represented by one moment average diameter is 4.8%. If a significant fraction of charged particles is captured in the electric field of the ion trap, the moment average may not apply directly, since the capture is dependent on the particle electrical mobility and charge states as described in Section 4.3.2. The operation of the NanoTracer and unipolar diffusion charging devices which employ low-efficiency electrostatic precipitators rely on this principle to derive particle diameter and concentration estimates [37, 39, 115, 116]. The range of particle size demonstrated in this section (30-200 nm CMD) is representative of those measured using low-cost ultrafine measurement devices whereas particles below 30 nm are less likely to charge or have a significant effect on the measured outlet currents.

4.4.7 Summary

This section analyses the effects of aerosol particle polydispersity on electrical currents resulting from photoelectric charging. A model for charging polydisperse particle distributions is developed and solved numerically for the first time considering charge transfer between ions and particles from each of the discrete size bins which make up polydisperse distributions. The results were compared with those from a model assuming a monodisperse particle distribution with the same total concentration using the second moment of the particle size distribution: the diameter of the average surface, $d_{\bar{s}}$, demonstrating good agreement.

4.5 Conclusions

This chapter introduced the first analysis of simultaneous photoionisation, recombination, convection/diffusion and electrical field transport of multiply-charged particles through a steady-state control volume using analytical and numerical techniques. Analytical equations were used to define characteristic times for photoionisation, recombination, convection, diffusion, and electric field transport mechanisms allowing the formulation of a range of dimensionless parameters to understand the relative contributions to the particle flux balance. The assumptions for the analytical model were demonstrated to be valid for a range of simple conditions of interest, as well as for system dimensioning. However, a more detailed numerical model including detailed charge accounting is required for average levels of charge per particle at or below +1 charges, as well as high ion losses. The 0D numerical and 3D

CFD models agree well for a large range of electric field strengths for the simple geometry of concentric cylinders, but differences appear at both high (above ≈8 V cm^{-1}) and low (below ≈0.8 V cm^{-1}) electric field strengths, where the detailed spatial resolution rather than a simple linear 0D model becomes necessary.

The effect of particle polydispersity on particle charging and transport was then explored using a simple method for calculating the second moment of a particle size distribution. Using the detailed CFD model, it was demonstrated that for a representative range of input aerosol parameters and operating conditions, the monodisperse model (44 charge states and coupled charge conservation equations) accurately predicts the electrical current output from a polydisperse particle distribution (represented by 16 size bins $\times$ 44 charge states = 704 simultaneous, coupled charge conservation equations) to within 4.8% and an average of 57 times lower computation time. The method of analysis is useful to both users and developers of low-cost ultrafine sensors to understand to effect of particle polydispersity on measurements.

Chapter 5

Experimental Validation of Model

5.1 Introduction

In this chapter, a low-strength electric field is applied during particle photoionisation to capture charge as it is photoemitted from the particles in continuous flow, yielding a novel electrical current measurement. As in conventional photoelectric charging-based measurement devices, a distinct electrical current from the remaining photoionised particles is also measured downstream. A three dimensional numerical model for particle and ion charging and transport is evaluated by comparing simulations of integrated electric currents with those from charged soot particles and ions in an experimental photoionisation chamber. The effects of particle size, concentration and electric field field strength are analysed while demonstrating agreement between model and experiment in each case.

5.1.1 Context

Relatively recent studies have evaluated photoemission theory by measuring the capture efficiency of photoionised particles in a high voltage electrostatic precipitator [78, 58, 66, 64]. The equation for photoemission yield generally includes an empirical constant which has been used as a fitting parameter for changes in particle size, light intensity, or flow rate [58, 66]. Li and Chen [64] investigated the effect of UV light intensity on the photoionisation of silver nanoparticles for a range of light intensities. They showed no size dependence for the photoemission constant of 7-30 nm silver particles, which is in agreement with photoemission theory and calculations, yet in contrast with previous research [58, 66]. Further work on modelling and experiments of particle photoionisation included the role of particle size, light intensity, residence time and diffusion losses [97, 75, 80, 103].

Equation 1.2 shows that the probability of photoelectric charging depends directly on the photoelectrically active area, which is proportional to the square of mobility diameter, d_{m}^2. The total charged particle flow is expected to therefore be proportional to the integral of the photoelectrically active area of all particles as described in Section 4.3,

$$A_{\mathrm{m}} = \int_0^{\infty} N_{\mathrm{m}} \pi d_{\mathrm{m}}^2 \, \mathrm{d}d_{\mathrm{m}} = N \int_0^{\infty} f(d_{\mathrm{m}}) \pi d_{\mathrm{m}}^2 \, \mathrm{d}d_{\mathrm{m}}, \tag{5.1}$$

where $f(d_{\mathrm{m}})$ is the probability distribution function of the particle size, N_{m} is the concentration of particles and can be written as a function of the particle's mobility. Owing to charge conservation, the total captured currents i_{e} and i_{o} indicated in Fig. 3.1 must be identical, and proportional to the photoelectrically active surface area. However, given the different rates of recombination, transport and capture of particles and ions through the electric field, the measurable currents from the photoelectric charging process are in effect different functions of concentration, N, and particle mobility diameter, d_{m}.

Measurements of the aerosol total active surface area are of interest for emissions, environmental or exposure monitoring, particularly for materials such as elemental carbon and diesel soot. However, the dependence of particle material and morphology on photoemission must be understood. For that reason, photoemission theory [59, 89, 81, 77] must be adequately validated using combined modelling and experimental techniques [78, 58, 66, 64, 97, 75, 80, 103].

5.1.2 Outline of chapter

In this chapter, the three-dimensional aerosol charging and transport model and detailed experiments described in Chapter 3 are used to demonstrate how photoionisation and an electric field can be employed to detect and measure particles in a continuous flow. Firstly, electrical current measurements for photoionisation of polydisperse soot particles in a range of sizes and concentrations are compared with those calculated from a 3D computational fluid dynamics model, which includes equations for particle and ion flow, photoemission, recombination, diffusional wall losses and electric field transport. A single empirical constant and particle work function are used to account for photoionisation. The novel approach of using an electric field to yield two distinct electrical current measurements is demonstrated to be useful for direct measurements of total photoelectrically active surface area of a known aerosol material. Then, experimental measurements from size-resolved, monodisperse silver aerosol particles are used to evaluate the modelling and measurement techniques for a range

of electric field strengths. In each case, agreement between the model and experimental results is evaluated.

5.2 Total mobility surface area measurements

In this section, experimental results are gathered using the experimental apparatus described in Section 3.3 and compared with results from the Computational Fluid Dynamics (CFD) model described in Section 3.2.

5.2.1 Modelling details and operating conditions

The product of light intensity, I, and a constant, K_c, is adjusted only once to match experimental results, as summarised in Table 5.1 along with the remaining operating conditions which correspond to the experimental set-up described in Section 3.3. A decrease in light intensity throughout the chamber has been qualitatively demonstrated, but not quantitatively validated. In the model, the light intensity is assumed to decrease with the inverse square law in the flow direction away from from the light source corresponding to the effects from a diffuse point source for light radiation. The product K_cI is defined explicitly at the particle flow inlet in Table 5.1, 2 cm from the light source.

A fixed concentration of particles with neutral charge is prescribed at the inlet. Monodisperse particles are prescribed in the model as a first-order approximation of the polydisperse distributions produced with the experimental set-up.

Table 5.1 Modelling parameters and operating conditions used for experimental validation.

Parameter	Symbol	Units	Value
Negative ion diffusivity [105]	$D_{\text{-}1}$	$m^2\ s^{-1}$	4.3×10^{-6}
Negative ion electrical mobility [105]	$Z_{\text{-}1}$	$m^2\ V^{-1}\ s^{-1}$	1.7×10^{-4}
Particle diameter	d	nm	20-80
Particle concentration	N	10^4-10^6	cm^{-3}
Flow rate	Q	std L min^{-1}	1.5
Bulk velocity	U	m s^{-1}	5.17×10^{-2}
Residence time	t	s	3.86
Empirical constant	m		2
Photoemission constant	K_cI	$J^{-1}\ m^{-2}\ s^{-1}$	1.15×10^{34}
Light energy	hv	eV (nm)	6.69 (185)
Work function [82]	Φ_∞	eV	4.95

5.2.2 Local current at low electric field strength

Initially neutral particles flow in the direction perpendicular to the electric field between two electrodes and away from the UV light source. The particles are photoionised, yielding ions and charged particles, which are simultaneously transported to the electrodes and measured as electrical current. Modelling results for the components of the electrode current density, i''_e, as a function of distance from the light source are shown in Fig. 5.1. The electrode current arises largely from capture of negatively charged ions nearest the light source; the rate of capture of ions decreases with distance from the light source. A much smaller fraction of the current is contributed by particles at each charge level as the flow proceeds away from the light source. The particles are photoionised to gain +1 charges which are further ionised to +2 charges and so on. The positively charged particles are captured at the electrode as the flow moves away from the light source, also contributing to the electrode current, i_e. The rate of capture depends on the charge level and particle transport in the electric field. Although particles of higher charge levels such as +4 and +5 charges are more likely to be captured due to their higher electrical mobility compared to particles with +2 or +3 charges, their concentrations are lower, as there is insufficient irradiation time or light intensity to reach the higher charge levels.

The components of the integrated electrode current are shown as a function of distance from the light source along the electrodes in Fig. 5.2 for applied voltages of 25 V (20 V cm^{-1}) and 150 V (120 V cm^{-1}). As ions are captured at the electrode near the light source, the total current increases to nearly its maximum value in the first half of the chamber. The capture of particles occurs further along the chamber after sufficient time for the electric field to transport the particles to an electrode. In the 150 V (120 V cm^{-1}) case, the contribution to electrode current from particle capture is significantly higher than the 25 V (20 V cm^{-1}) case. The captured particles in the 150 V (120 V cm^{-1}) case cannot contribute to the outlet current i_o, and therefore reduce the total outlet current. In the 25 V (20 V cm^{-1}) case, the electrode current, i_e, arises largely due to the cross transport of negative ions, whereas the outlet current, i_o, has equal magnitude and opposite sign, largely due to positively charged particles. After testing a range of electric field strengths over 0-150 V cm^{-1} (6 points logarithmically spaced) for the given flow rates and particle sizes, the field level corresponding to 25 V (20 V cm^{-1}) is nearly optimum to yield maximum outlet current, i_o, and directly measure the total effect of particle photoionisation. Applied voltages lower than $\approx$10 V (8 V cm^{-1}) provide insufficient ion capture and so allow more particle-ion recombination and reduce the electrical current at the outlet, i_o. For applied voltages higher than $\approx$25 V (20 V cm^{-1}), the capture of charged particles becomes significant as demonstrated by the analysis for 150 V (120 V cm^{-1}).

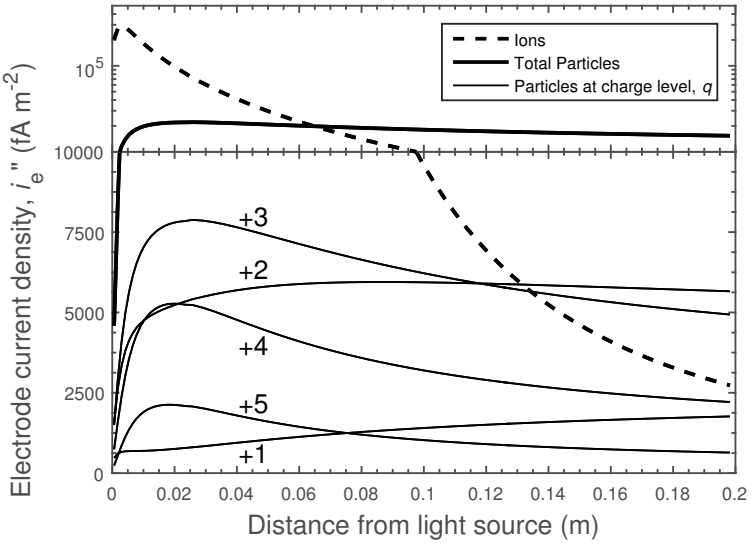

Fig. 5.1 Contributions to electrode current density, i''_e, as a function of distance from the light source for ions, particles from charge level, q = 1 $\rightarrow$ 5, and the sum total of all charged particles ($d = 80$ nm, $N = 10^5$ cm^{-3}) at an applied voltage 25 V (20 V cm^{-1}). Note: y-axis scale changes to log scale at 1×10^4 fA m^{-2}.

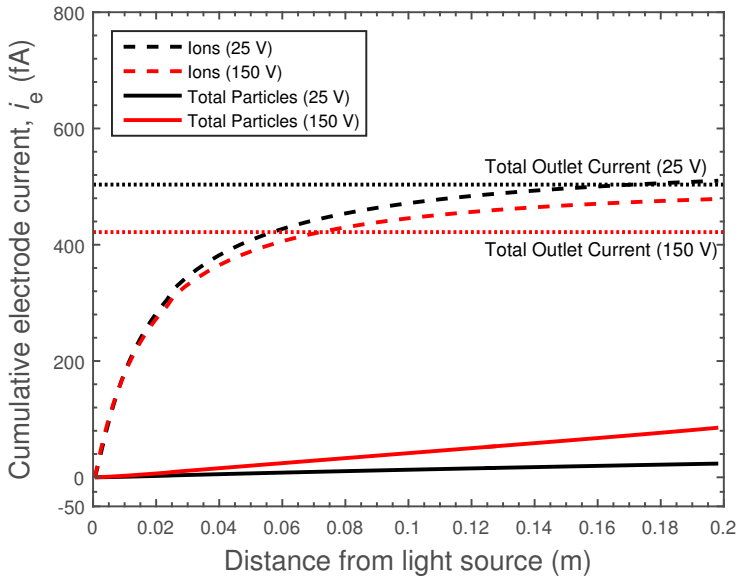

Fig. 5.2 Contributions to total cumulative current at the electrode, i_e, as a function of distance from the light source for ions and particles ($d = 80$ nm, $N = 10^5$ cm^{-3}) at applied voltages of 25 V (20 V cm^{-1}) and 150 V (120 V cm^{-1}).

The effect of electric field strength on output electrical current will be discussed in the next section. For particle sizes smaller than 80 nm diameter, the capture of particles at the electrode becomes more significant, and can affect the electrode current, as discussed below.

5.2.3 Total mobility surface area

The electrode current, i_e, and outlet current, i_o, were measured for the photoionisation of fractal-like, agglomerate soot particles (characterised in Stettler et al. [109]) over a range of count median (mobility) diameters, CMD (25-80 nm), and total concentrations, N (9×10^4 - 1.1×10^6 cm^{-3}) as measured by SMPS. Numerical calculations for the geometry and operating conditions considered were performed, in which a single empirical parameter corresponding to the product, $K_c I$, was adjusted to fit the model to the experiment for a single measurement. Figure 5.3 compares the results of the CFD model with the measurements, shown in the surface plot of the outlet current.

The outlet current, i_o, increases with both increasing particle concentration and diameter. The experimental and modelling results agree well for a range of particle mobility diameters (25-65 nm) with agreement up to 80 nm and concentrations (9×10^4 - 1.1×10^6 cm^{-3}) using a single value for $K_c I$. The results show that the mobility diameter can be used as the characteristic particle diameter, d, in Eq. 1.2 even for agglomerates [51, 48, 98], agreeing with previous research for the range of soot morphology measured in this work [109]. For this reason, the CMD for mobility diameter is represented by d in the remaining discussion.

The form of the dependence of current on diameter and concentration suggests a power law of the form:

$$i = \gamma N^{\delta} d^{\varepsilon} \tag{5.2}$$

with power fit coefficients δ and ε. Any current independent of the particle photoionisation process, e.g. photoemission from housing walls is represented in the intercept coefficient, γ, and the absolute values of the remaining coefficients, $\ln i = \ln \gamma + \delta \ln N + \varepsilon \ln d$, as long as it remains constant between measurements. The relative effect of particle concentration and size on electrical current remains independent of background current, therefore the ratio ε/δ remains constant. Fitting parameters for both Figs. 5.4 and 5.5 can be obtained from either the CFD model or directly from the experiments, and are shown in Table 5.2 for an applied voltage of 25 V (20 V cm^{-1}). Once the fitted powers in Eq. 5.2 have been obtained, it is possible to obtain the expected particle concentration for a given measured diameter and current. Figure 5.4 shows the expected concentration, $<N> = \left(i\gamma^{-1}d^{-\varepsilon}\right)^{1/\delta}$, obtained using the parameters of Eq. 5.2 fitted to the CFD model. The experimentally measured currents, i_o and i_e, are plotted against measured concentrations for an applied voltage of 25 V (20 V cm^{-1}).

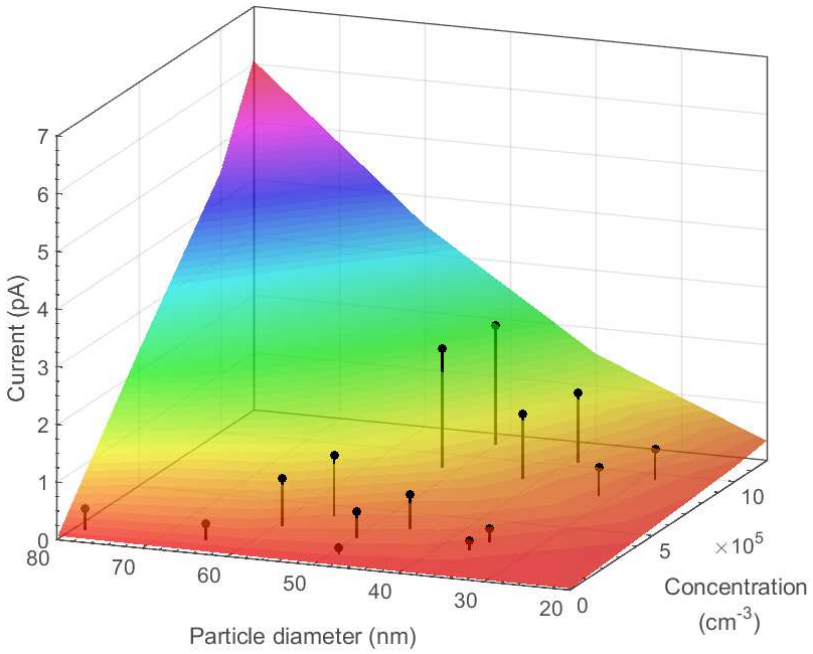

Fig. 5.3 Outlet current, i_o, as a function of particle concentration and diameter for applied voltage of 25 V (20 V cm^{-1}) from model (coloured surface) and experiment (black).

Likewise, Figure 5.5 shows the expected diameter, $<d>= \left(i\gamma^{-1}N^{-\delta}\right)^{1/\varepsilon}$, derived from the parameters of Eq. 5.2 fitted to the CFD model and measured currents, and concentrations for an applied voltage of 25 V (20 V cm^{-1}). Experimental values of currents were measured with lognormal particle size distributions of soot featuring $25 \leq d \leq 80$ nm and geometric standard deviations between 1.54 and 1.75. These results for polydisperse measurements agree well with modelling results for monodisperse particle diameters of 40-80 nm and concentrations of 1×10^4 - 1.2×10^6 cm^{-3} as shown by the correlation plot in Figs. 5.4 and 5.5. Modelling results for monodisperse particles outside of this range cannot capture the current from a small concentration of larger particles that are present in polydisperse distributions. The uncertainties in the mean particle diameter and total concentration from the SMPS are 1% and 10%, respectively, consistent with published values [111, 113]. The error bars represent the standard error in i_o and i_e current measurements which average less than 1 fA and 70 fA, respectively, for 30 seconds of measurements per data point at a rate of 1 second per measurement. The outlet current is more adequately shielded from electronic noise yielding more accurate measurements. Both Figures 5.4 and 5.5 show the CFD model agrees well with the experiment for measurements of concentration and diameter for a single K_cI fitting parameter of 1.15×10^{34} J^{-1} m^{-2} s^{-1}.

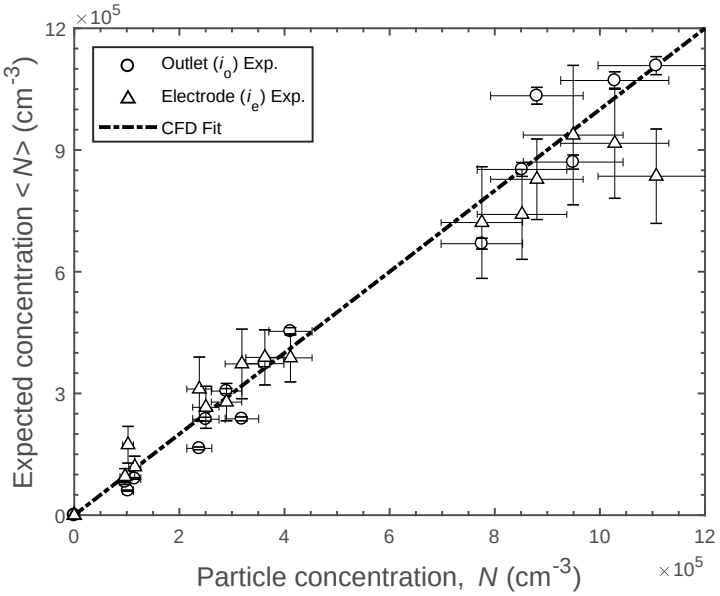

Fig. 5.4 Expected concentration from measured currents, i_o and i_e, as a function of measured concentration using linear regression fitting parameters from CFD model results: $\langle N \rangle = \left(i\gamma^{-1}d^{-\varepsilon}\right)^{1/\delta}$ at 25 V (20 V cm^{-1}). The coefficients of determination are 0.97 and 0.90 for i_o and i_e respectively.

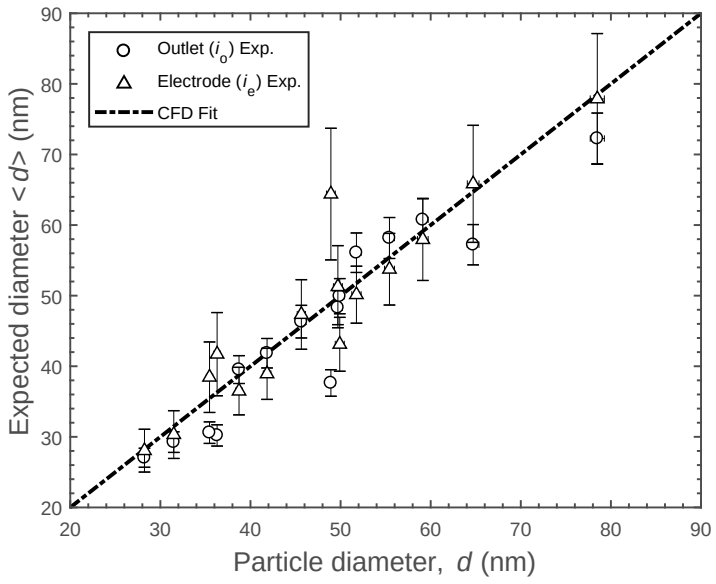

Fig. 5.5 Expected diameter from measured currents, i_o and i_e, as a function of measured diameter using linear regression fitting parameters from CFD model results: $\langle d \rangle = \left(i\gamma^{-1}N^{-\delta}\right)^{1/\varepsilon}$ at 25 V (20 V cm^{-1}). The coefficients of determination are 0.88 and 0.87 for i_o and i_e, respectively.

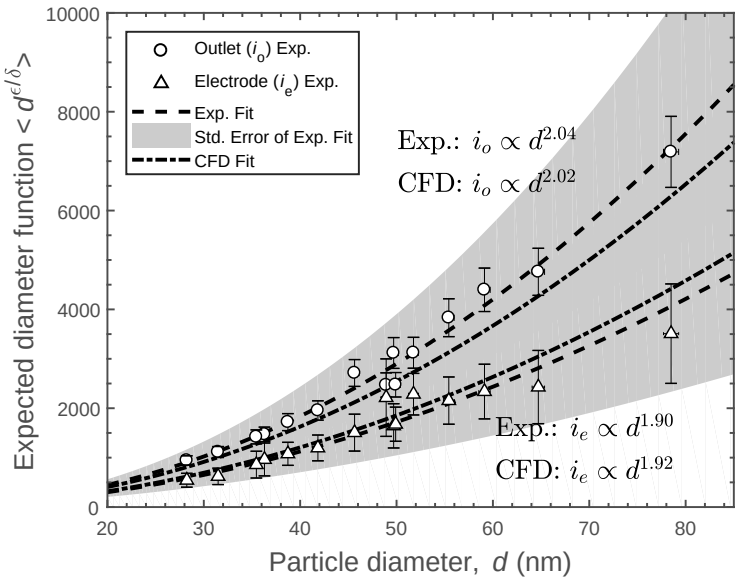

Fig. 5.6 Expected particle diameter function from measured currents, i_{o} and i_{e}, as a function of measured particle diameter using independent linear regression fitting parameters from experiment and CFD model results: $<d^{\varepsilon/\delta}>= \left(i\gamma^{-1}N^{-\delta}\right)^{1/\delta}$ at 25 V (20 V cm^{-1}).

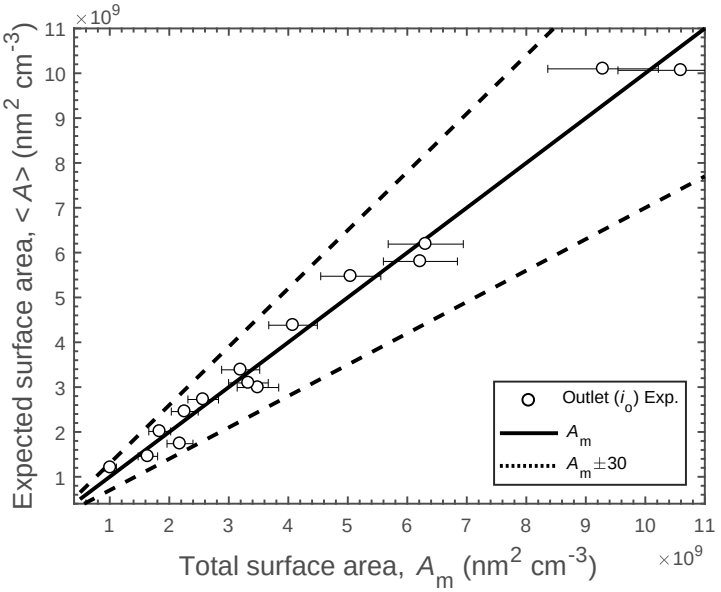

Fig. 5.7 Expected photoelectrically active surface area from measured current, i_{o}, as a function of total measured (mobility) surface area using linear regression fitting parameters from experiment: $<A_{\mathrm{m}}>= \dfrac{i_{\mathrm{o}} - b}{C}$ at 25 V (20 V cm^{-1}). (C = 2.2×10^{-7}, b = 151 fA, R^2 = 0.98).

Table 5.2 Power law regression fitting parameters for an applied voltage of 25 V (20 V cm^{-1}). Uncertainty is quantified by standard error in brackets.

	γ	δ	ε	ε/δ	R^2
Outlet (i_o) Exp.	6.75×10^{-9} ($\pm5.40\times10^{-9}$)	1.22 (±0.036)	2.48 (±0.11)	**2.04** (±0.076)	0.99
Outlet (i_o) Mod.	9.16×10^{-7}	0.99	1.99	**2.02**	1
Electrode (i_e) Exp.	1.83×10^{-4} ($\pm1.46\times10^{-4}$)	0.75 (±0.038)	1.44 (±0.12)	**1.90** (±0.13)	0.97
Electrode (i_e) Mod.	1.49×10^{-6}	0.99	1.89	**1.92**	1

The independent power regression fits for results from experiment and CFD modelling show that the outlet current, i_o, depends on the particle diameter according to $i_o \propto d^{2.04}$ and $i_o \propto d^{2.02}$ for experimental and modelling results, respectively, as shown in Fig. 5.6. The electrode current shows $i_e \propto d^{1.90}$ and $i_e \propto d^{1.92}$ from experimental and modelling results, respectively. The capture of a fraction of the positively charged particles as well as the negative ions at 25 V (20 V cm^{-1}) increases the ratio of coefficients from the value of 2 in Eq. 1.2 for the outlet current and decreases it for the electrode current.

For an applied voltage of 25 V, the outlet current, i_o, is linearly proportional to concentration and nearly proportional to the square of diameter, i.e. $i_o \approx CNd^2 + b$. This convenient relationship gives a direct measure of total expected particle mobility surface area, $<A_m>$, defined in Eq. 5.1. The total photoelectric surface area estimates generated using i_o at 25 V (20 V cm^{-1}) are plotted as a function of the total measured surface area from the SMPS in Fig. 5.7. All the estimates generated by the photoionisation device are within 30% of the SMPS values for A_m, demonstrating that under these conditions, the total photoelectrically active surface area is proportional to the total mobility surface area as measured by SMPS.

The photoemission response of soot particles from a propane flame subject to an applied electric field are analysed in the present work. Real world aerosols contain mixtures of photo-emitting and some weakly photo-emitting materials. For example, photoemission from NaCl aerosols was below the detection limits of the present set-up. However, with further understanding, the photoionisation may provide the opportunity for material selective measurements in real-world aerosols.

5.3 Conclusions

The novel charging and measurement method of this work has been demonstrated by applying an electric field to allow the direct measurement of photoemitted charge from particles captured in the electric field in continuous flow. The 3D computational fluid dynamics model was used to demonstrate an applied voltage of 25 V (20 V cm^{-1}) is nearly optimal for capturing ions at the electrode without largely capturing charged particles for the particular geometry and particle range. The model shows good agreement for measurements of two distinct electrical currents (electrode, i_e, and outlet, i_o) with those from experimental photoelectric charging of soot particles in a range of sizes and concentrations, for a single fitting parameter for all cases, to account for light intensity. This demonstrates that the physics of the problem is suitably captured by the model and that the method can be used to estimate material dependent fitting parameters such as $K_c I$. At a low applied voltage of 25 V (20 V cm^{-1}), for which $\varepsilon/\delta \approx 2$, a direct measurement of total mobility surface area, A_m, of soot particles becomes possible, with an accuracy of within 30% of SMPS measurements. Mobility diameter is confirmed as a suitable characteristic diameter used in photoionisation equations, agreeing with previous research.

Chapter 6

Aerosol Active Surface Area

6.1 Introduction

The purpose of this chapter is to evaluate the effects of the material and morphology of an aerosol particle on its ultraviolet photoemission. Particle photoemission theory is refined to include explicit definitions of photoelectrically active area to account for the photoemission yield from particles with different morphologies. The revised definitions of photoelectrically active area are evaluated with experimental results.

6.1.1 Context

Direct ultraviolet (UV) photoionisation is an electrical charging mechanism distinct from diffusion charging; the process is material- and surface-dependent [70, 117, 46, 49, 40, 48, 57, 63, 50, 19, 99, 65, 22, 98]. The material-dependent charging mechanism and increased charging efficiency, particularly at low particle sizes ($d < 50$ nm), is of interest environmental and emissions measurements [65, 40], particle classification [66], capture [58, 67, 68], controlled deposition [69], and fundamental studies of the properties of nanoparticles and their surfaces [70–73].

The photoemission quantum yield can be measured from the slope of a plot of total photoelectric yield versus the photoelectrically active surface area, σ_{ph}, of an ionised particle. The latter is not explicitly defined, though it is proportional to total (mobility) surface area, A_{m}, as demonstrated and discussed in Chapter 5. Quantum yields are found to be a strong function of material, with relatively large values for silver, polycyclic aromatic hydrocarbons (PAHs) and elemental carbon, whereas aerosols such as NaCl [40], di-octyl sebacate (DOS), and secondary organic aerosols are weak photoemitters in the UV spectrum. The photoelectric quantum yield has also been found to vary between different morphologies of the same pure

material. Three studies which discuss morphology effects on aerosol photoemission in detail seemingly contradict one another [51, 48, 101]. Zhou et al. [51] found the overall charging efficiency of silver aggregates to be 0.4-0.8 times that of silver spheres of the same mobility diameter. This result disagrees with an existing photoemission theory which suggests that particles of the same material and mobility should have the same photoelectric charging efficiency regardless of their morphology [48]. Further, Schmidt-Ott [101] demonstrated that sintering reduced the photoelectric charging efficiency of silver agglomerates, though the effects of changes in particle mobility and morphology were treated together as a function of sintering temperature.

Any practical measurement device or diagnostic technique must be accompanied by sufficient understanding and interpretation of measurements using validated particle photoemission theory. The photoelectrically active surface area, while defined as proportional to mobility surface area, has not yet been explicitly defined in the photoionisation equations.

6.1.2 Outline of chapter

In this chapter, the photoelectrically active area is defined explicitly, including its relationship to particle mobility surface area, to reflect the effect of particle morphology on total photoelectric yield. A fixed-wavelength UV light source and detection system is used to measure photoemission from silver agglomerates and direct and catalytically oxidised carbon agglomerates from a propane flame to demonstrate the effect of different particle material types and surface properties. Photoelectric yield from silver agglomerates and sintered spheres is used to demonstrate the effect of particle morphology by varying the mobility surface area of the particles. The definition of photoelectrically active area which accounts for the effect of particle morphology is then evaluated with experimental results.

6.2 Theory

There are three steps involved in photoemission from surfaces in a vacuum [74] and a fourth step is included for particles in a carrier gas [46][1]

1. absorption of a photon and excitation of an electron;
2. movement of the electron to the surface;
3. overcoming of the surface potential; and
4. removal of the electron from the vicinity of the particle.

[1]The discussion of the photoelectric emission mechanism of Section 1.2.3 is repeated here for additional context.

After photoemission, the remaining particle is positively charged which reduces the probability of further release of electrons. Step 1 requires that the photoemitting material is exposed to the photon flux and step 4 requires that photoemitting material is located externally-to rather than shielded inside the particle. Electrons emitted from a particle's interior may be reabsorbed by material within the same particle and never leave the particle [72].

6.2.1 Exposed surface shape factor

Schmidt-Ott [101] introduced an *in situ* method for measuring shape factors of particles by comparing mobility and photoelectric activity of particles in a carrier gas before and after sintering silver agglomerates into close-packed spheres. The author defined a shape factor, S, which accounts for the proportion of primary particles exposed to the gas surrounding the agglomerate, and quantified S using measurements of photoelectric activity. The method for relating the exposed surface to photoelectric activity is presented and applied here to provide context for the definition of photoelectrically active area.

For structures grown by diffusion-limited aggregation, the number of primary particles exposed to the surrounding gas molecules, $n_{\mathrm{pp,e}}$, is assumed to be proportional to the total number of primary particles, n_{pp}, raised to the power, S,

$$n_{\mathrm{pp,e}} \sim n_{\mathrm{pp}}^{S} \tag{6.1}$$

where S is defined as a shape factor. Only primary particles exposed to the surrounding gas experience collisions with gas molecules, thus acting as a shield for the interior primary particles.

The total number of primary particles, n_{pp}, in a close-packed sphere of diameter d_{cl} is given by

$$n_{\mathrm{pp}} \sim d_{\mathrm{cl}}^{3} \tag{6.2}$$

for a large ratio of $d_{\mathrm{cl}}/d_{\mathrm{pp}}$ where d_{pp} is primary particle diameter.

Following Schmidt-Ott [101], by combining Eqs. 6.1 and 6.2, and assuming that the photoelectric activity is linearly proportional to the number of exposed primary particles, $(n_{\mathrm{pp,e}})$, the photoelectric activity, ε (*i.e.* the number of electrons emitted from an agglomerate particle), is proportional to its equivalent close-packed sphere diameter after sintering, d_{cl}, raised to a power $3S$, according to:

$$\varepsilon \sim d_{\mathrm{cl}}^{3\mathrm{S}} \tag{6.3}$$

The case where all of the primary particles are exposed in an idealised straight-chain morphology leads to a shape factor limit S near unity. Conversely, the highest shielding configuration of primary particles occurs for a close-packed sphere, where S approaches 2/3 for a large ratio of $d_{\mathrm{cl}}/d_{\mathrm{pp}}$. A value of $S = 0.92$ has been found for silver agglomerates generated with an evaporation/condensation process [101].

6.2.2 Photoelectric yield

The quantum yield, Y, of Eq. 1.3 describes the conditions under which photoemission occurs *i.e.* if the specific photon energy is higher than the work function, $\Phi^{q\rightarrow q+1}$, of Eq. 1.4. The charge-dependent work function increases with each emitted charge due the resulting stronger electrostatic field until a maximum photoelectric charge state is reached. The charge-dependent work function, $\Phi^{q\rightarrow q+1}$, is a function of the particle electrical capacitance, or ability to hold charge, which is in turn a function of particle size and morphology [118]. It has been demonstrated that the effect of the particle capacitance, along with differences in geometric surface area, account for a 17-30% increase in unipolar diffusion charging efficiency of agglomerates over spheres of the same material [118–121].

The electrons released via photoemission from particles in a carrier gas collide with neutral gases, forming gaseous ions. It has been shown in Chapter 4 (Table 4.2 and Eq. 4.4) that under conditions where the rate of recombination of ions with charged particles is not dominant, the total photoelectric activity generated over the total irradiation time, t, can be measured by collecting the total current of photoemitted electrons, i_{e}, or the remaining positively charged particles, i_{o}. The electrical current measurements are a function of the quantum yield, Y, as follows

$$i = i_{\mathrm{o}} = -i_{\mathrm{e}} = cYA_{\mathrm{ph}} \tag{6.4a}$$

$$c = \frac{I}{h\nu} tQe \tag{6.4b}$$

$$A_{\mathrm{ph}} = N \int_0^{\infty} p(d)\sigma_{\mathrm{ph}}(d)\,\mathrm{d}d \tag{6.4c}$$

where c is an operation constant which depends on the volumetric flow rate of the carrier gas[2], Q, and electron charge, e. The total photoelectrically active area, A_{ph}, is the integral sum of the photoelectrically active area, σ_{ph}, for the probability density function, $p(d)$, of particle diameter, d, multiplied by the total number concentration, N. For a monodisperse particle distribution, $A_{\mathrm{ph}} = N\overline{\sigma}_{\mathrm{ph}}$ where N is total number concentration. For the sufficiently

[2]Assuming particles are entrained in the flow.

large difference between the specific photon energy, $h\nu$, and the work functions, Φ, of this work, the quantum yield, Y, of Eq. 6.4 may be considered constant; an assumption which is valid for charge states sufficiently below the photoelectric charging limit as discussed in Chapter 4 (Eq. 4.7).

6.2.3 Photoelectrically active area

The photoelectrically active area of a particle, σ_{ph}, accounts for the total area of material exposed to the photon flux as well as the particle surroundings rather than shielded inside the particle. The quantity is defined here:

$$\sigma_{\mathrm{ph}} = \pi d_{\mathrm{pp}}^2 n_{\mathrm{pp,e}} \phi \tag{6.5}$$

for primary particle diameter, d_{pp}, and number of primary particles exposed to its surroundings, $n_{\mathrm{pp,e}}$. The filling factor, ϕ, accounts for a fraction of the exposed primary particles which is not photoelectrically active. For a homogeneous material with no void space in the primary particle, $\phi = 1$.

For a spherical particle in a carrier gas, $d_{\mathrm{pp}} = d_{\mathrm{p}} = d_{\mathrm{m}}$ and $n_{\mathrm{pp,e}} = n_{\mathrm{pp}} = 1$ where d_{p} and d_{m} are particle diameter and mobility diameter, respectively. Equation 6.5 becomes

$$\sigma_{\mathrm{ph}} = \pi d_{\mathrm{m}}^2 \phi. \tag{6.6}$$

The filling factor, ϕ, is equal to one for a perfect sphere where the entire surface of the sphere is photoelectrically active, homogeneous material. A close-packed sphere, which results after agglomerate sintering, is composed of a porous structure which includes material and void space to make up the overall volume of the sphere [30]. For a close-packed sphere, where $d_{\mathrm{pp}} = d_{\mathrm{m}}$, and $n_{\mathrm{pp,e}} = n_{\mathrm{pp}} = 1$, Eq. 6.6 is used where ϕ is the volume fraction of the raw material within the close-packed sphere. Applied here, ϕ is the ratio of effective density, ρ_{eff}, and material bulk density, ρ.

For ideal aerosol agglomerates with polydisperse spherical primary particles and no sintering necks, the average size of a primary particle and average number of primary particles are represented by the volume-surface equivalent primary particle with diameter, d_{va}, and number of primary particles, n_{va}, respectively, using readily measurable quantities of mobility diameter, d_{m}, and agglomerate mass, m, by [122, 123]

$$d_{\mathrm{va}} = \frac{6v}{a} = \left(\frac{\pi k_a \rho}{6m} (d_{\mathrm{m}})^{2D_\alpha} \right)^{\frac{1}{2D_\alpha - 3}} \tag{6.7a}$$

$$n_{\mathrm{va}} = \frac{m}{\rho} \frac{6}{\pi d_{\mathrm{va}}^3} \tag{6.7b}$$

for volume, v, of agglomerated material, total surface area, a, and material of density, ρ. Combining Eqs. 6.7a and 6.7b, it may be demonstrated that $d_{\mathrm{m}}^2 = n_{\mathrm{va}} d_{\mathrm{va}}^2$ within the approximation that the empirical pre-exponential term, $k_a = 1$, and power law exponent, $D_\alpha = 1$. This definition assumes the mobility surface area is made up of the sum of the surface areas of each of the primary particles and there is no shielding of primary particles from the surrounding gas by other primary particles in the same agglomerate. Taking the diameter and number of primary particles as the total volume-surface equivalent diameter and number, respectively, and assuming every primary particle exposes an equal surface area to its surroundings, describes an idealised agglomerate with $n_{\mathrm{pp,e}} = n_{\mathrm{pp}} = n_{\mathrm{va}}$, and $d_{\mathrm{va}} = d_{\mathrm{pp}}$. For idealised agglomerates, Eq. 6.5 takes the form of Eq. 6.6 for $\phi = 1$.

Within the validity of the assumptions presented here, the photoelectrically active surface area for a sphere or idealised agglomerate is linearly proportional to its mobility surface area, πd_{m}^2, of Eq. 6.6, though the sphere and agglomerate may have different photoelectrically active surface areas for the same particle mobility. The differences in photoelectrically active area between the close-packed spheres and non-ideal agglomerates in this work arise in values of the pre-exponential and power law exponents (k_a and D_α, respectively) and the filling factor, ϕ. Eggersdorfer et al. [123] demonstrated that constant values of $k_a = 0.998$ and $D_\alpha = 1.069$ are valid for a polydisperse mix of primary particles regardless of the sintering mechanism or state of sintering which reflects the exposed surface area of the agglomerate.

The total particle mobility surface area, A_{m}, is defined as

$$A_{\mathrm{m}} = N \int_0^\infty p(d_{\mathrm{m}}) \pi d_{\mathrm{m}}^2 \, \mathrm{d}d_{\mathrm{m}} \tag{6.8}$$

where N is the concentration of particles for the mobility diameter probability distribution function, $p(d_{\mathrm{m}})$, and $A_{\mathrm{m}} = \pi N \bar{d}_{\mathrm{m}}^2$ for a monodisperse particle distribution. Assuming the quantum yield, Y, is not significantly size-dependent, the total measured current resulting from photoemission is linearly proportional to the total mobility surface area for idealised, monodisperse spheres or agglomerates by combining Eqs. 6.4, 6.6, and 6.8 to give

$$i = cYN\pi\bar{d}_{\mathrm{m}}^2 = cYA_{\mathrm{m}}. \tag{6.9}$$

Further, the projected area, a_{a}, of agglomerate particles is defined as $a_{\mathrm{a}} = \pi d_{\mathrm{m}}^2/4$ in the free molecular [124] and transition [125] regimes. Since projected area is a constant factor multiplied by mobility area, it is also linearly proportional to the current measurements defined in Eq. 6.9.

Mobility diameter and mobility surface area can be easily measured and used in the photoelectric charging equations by neglecting the effect of particle morphology. However, total photoelectric yield, as measured by electrical current in Eq. 6.4, is proportional to the photoelectrically active surface, which is easily conflated with total particle surface area or mobility surface area. In the following sections, the hypothesis is tested that total mobility surface area, A_{m}, correlates with photoelectric yield for different particle morphologies and materials, demonstrating the impact of both factors on photoelectric yield.

6.3 Results

6.3.1 Particle characterisation

The particle's aerodynamic diameter, d_{ae}, classified by the AAC in tandem with the mobility diameter, d_{m}, classified by the downstream DMA provides the ability to determine several particle geometrical parameters by applying simplifying assumptions. Volume equivalent diameter, $d_{\mathrm{ve}} = f(d_{\mathrm{ae}}, d_{\mathrm{m}})$ [28], effective density, $\rho_{\mathrm{eff}} = f(d_{\mathrm{ae}}, d_{\mathrm{m}})$, and particle mass, $m = f(\rho_{\mathrm{eff}}, d_{\mathrm{m}})$ [126] were estimated using Eq. 1.1. The relationship between particle mobility and effective density was measured and described using the mass-mobility exponent, D_{fm}, and pre-factor, k_{m} [30]. The primary particle diameter, d_{pp}, and number of primary particles, n_{pp}, were calculated as their volume surface equivalent primary particle diameter, d_{va} (Eq. 6.7a), and number, n_{va} (Eq. 6.7b), respectively, assuming an elemental soot density ($\rho = 1.9 \times 10^3$ kg m^{-3}) or silver density ($\rho = 10.5 \times 10^3$ kg m^{-3}) and constant values of $k_a = 0.998$ and $D_\alpha = 1.069$ [123, 127].

Samples of raw and sintered silver particles were mobility size selected with a DMA and deposited on a silicon substrate using an electrostatic precipitator[3]. Scanning electron microscope (SEM: LEO GEMINI 1530VP FEG-SEM) images were captured under a 10 kV acceleration voltage and are shown in Fig. 6.1. Figure 6.1a shows that the sintered

[3] SEM images gathered by Xiao Zhang (U. of Cambridge)

silver particles captured at $d_m = 40$ nm are largely sintered into spheres. Figure 6.1b shows sintered silver particles with mobility diameter $d_m = 85$ nm approximate close-packed spheres and have a significantly different morphology from the raw agglomerate silver particles at the same mobility size shown in Fig. 6.1c. The sintering process reduces the available surface area exposed to the particle surroundings. The mass-mobility exponent, D_{fm}, and pre-factor, k_m, were calculated for silver agglomerates ($D_{fm} = 2.49, k_m = 0.72$) and close-packed spheres ($D_{fm} = 2.78, k_m = 153$), respectively, further demonstrating that the particles changed morphology due to sintering.

6.3.2 Photoelectric yield as a function of particle size, concentration, and material

The electrical currents resulting from photoemission from aerodynamically monodisperse, silver and soot agglomerates were measured across a range of particle mobility CMDs (Ag, 20-110 nm, Soot, 40-200 nm), and total number concentrations (Ag, 1.8×10^4 - 3.8×10^6 cm^{-3}, Soot, 3.3×10^4 - 8×10^5 cm^{-3}). Electrical currents, i_o, produced from the charged particles collected downstream of the photoionisation chamber are shown as a function of particle mobility diameter and total number concentration for silver agglomerates and catalytically oxidised soot agglomerates in Figures 6.2a and 6.2b, respectively. A linear regression yields $i_o \sim N d_m^{2.06}$ for silver and $i_o \sim N d_m^{2.11}$ for soot, with coefficients of determination of 0.98 and 0.97, respectively. Both of these fitted exponents are approximately 2, thereby confirming that particle's mobility surface area is a suitable measurement for comparison as described in Eq. 6.9.

Figure 6.3 shows the photoelectric current plotted against the total mobility surface area, A_m, derived using Eq. 6.8. Both the raw soot and catalytically oxidised soot show similar quantum yields. The raw soot produced by the propane flame in this study likely had minimal adsorbed volatiles on the particle active surface, greatly limiting any effects due to catalytic oxidation on the resulting quantum yields. Agglomerate silver had a photoelectric yield approximately five times higher than the propane flame soot for the same mobility surface area. Carbon has a higher work function than silver (for soot, ≈4.95 eV, Ag, 4.25-4.75 eV [82]). Calculating the expected enhancement due the difference in work functions of soot and silver agglomerates (4.95 eV and 4.33 eV for soot [82] and Ag [102], respectively), using Eq. 1.3 with a constant value for K_c, results in an expected enhanced yield of approximately 1.8×. The five times enhancement in photoelectric yield of silver agglomerates over soot agglomerates is not fully explained by the difference in the work functions, and a further material or surface dependency must be considered.

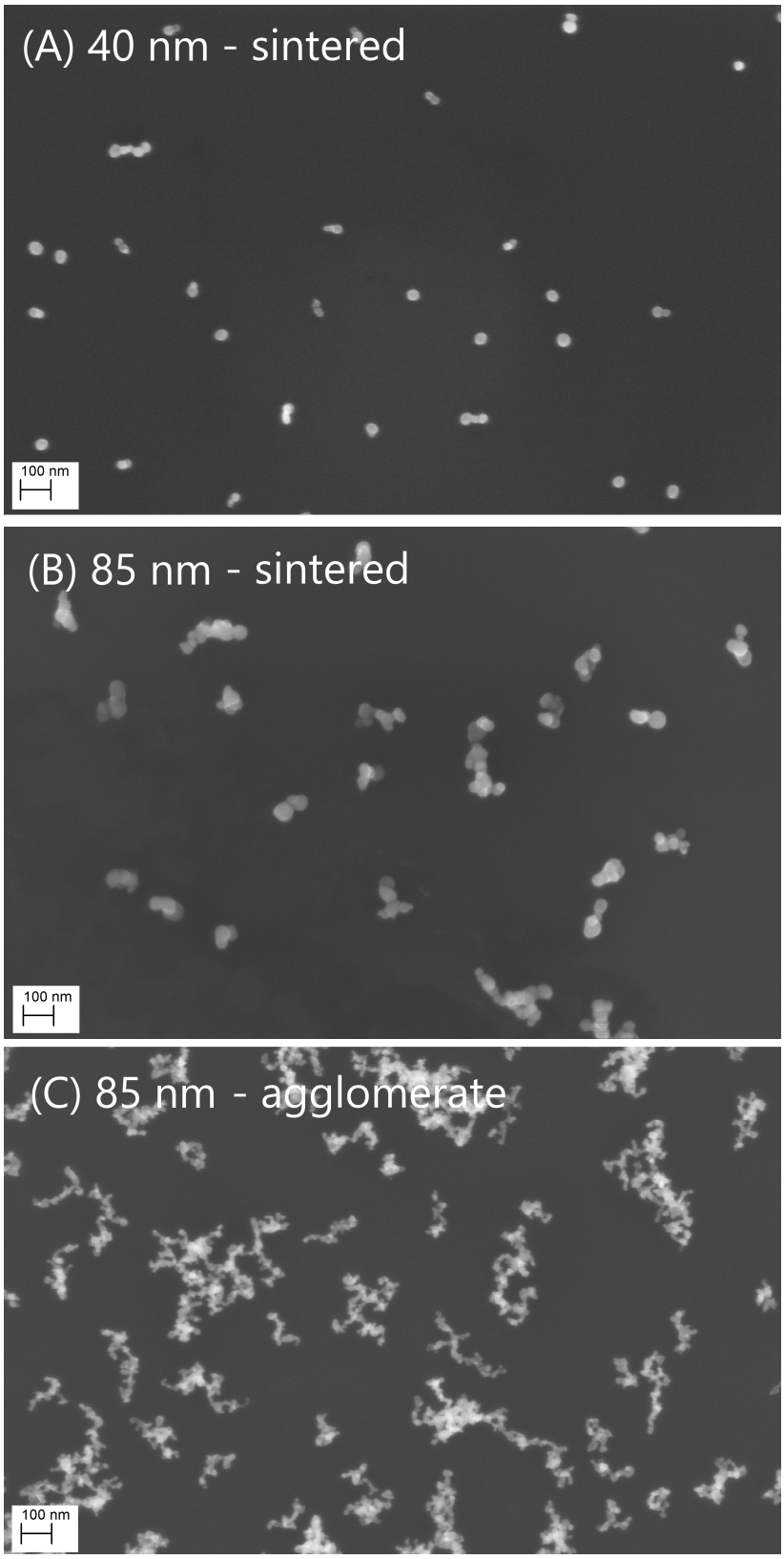

Fig. 6.1 SEM images of mobility selected silver nanoparticles: (A) sintered spheres, $d_{\mathrm{m}} = 40$ nm, (B) sintered, close-packed spheres, $d_{\mathrm{m}} = 85$ nm, (C) raw agglomerates, $d_{\mathrm{m}} = 85$ nm.

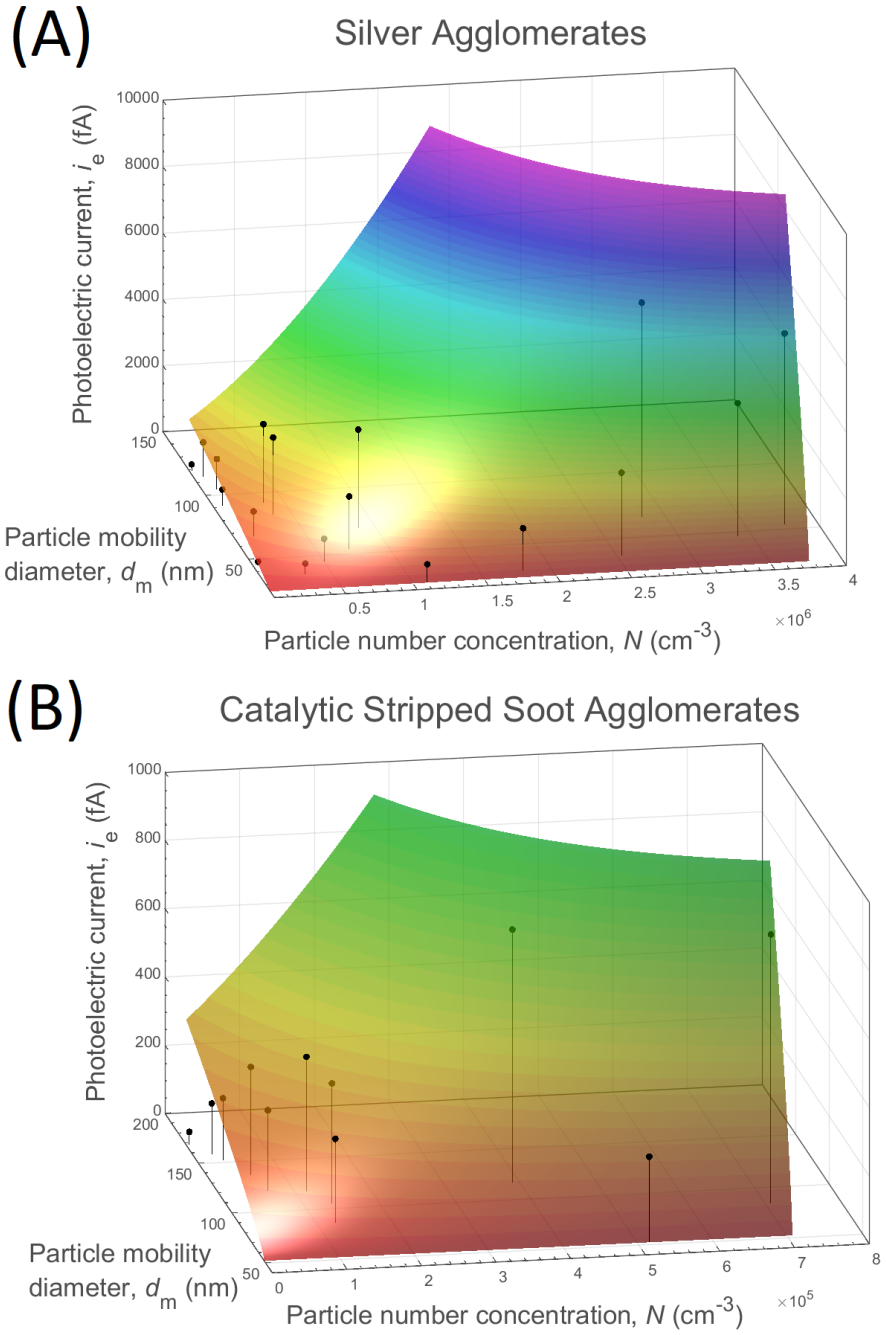

Fig. 6.2 Measured photoelectric particle current, i_o, as a function of particle number concentration and mobility diameter using a 30 V (24 V cm^{-1}) capture voltage for (A) silver agglomerates and (B) soot agglomerates after a catalytic stripper. A linear regression fit yields $i_o \sim N d_m^{2.06}$ for silver and $i_o \sim N d_m^{2.11}$ for soot, with coefficients of determination of 0.98 and 0.97, respectively.

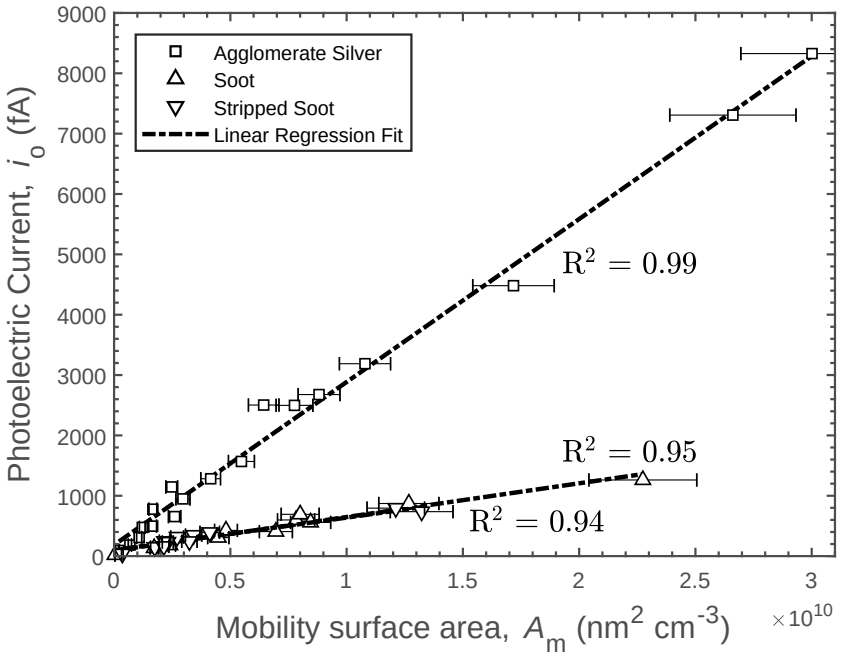

Fig. 6.3 Photoelectric current, i_o, as a function of mobility surface area, A_m (Eq. 6.8), for agglomerate silver, raw soot, and soot downstream of a catalytic stripper. Coefficients of determination for agglomerate silver, soot, and catalytic stripped soot are 0.99, 0.95, and 0.94, respectively.

6.3.3 Effects of particle morphology on photoelectric yield

Figure 6.4a shows that the measured photoelectric current, i_o, is a linear function of mobility surface area for both agglomerate and sintered silver particles corresponding to Eq. 6.9. For $A_m < 1.2 \times 10^{10}$ nm^{2}cm^{-3}, coefficients of determination for silver agglomerates and spheres are 0.96 and 0.98, respectively. Silver agglomerates have a photoelectric yield approximately 2.6 times higher than sintered silver for the same mobility surface area, A_m, or total projected area, $a_a N$. This result contradicts previous research which suggests silver agglomerates have a lower photoelectric yield than sintered silver particles of the same mobility diameter [51], or that the photoelectric yield for particles of the same material and mobility diameter should be the same regardless of their morphology [48]. For the same mobility size, agglomerated silver particles have more material exposed the photon flux and to the particles' surroundings compared with a close-packed structure that results from particle sintering [101]. In a close-packed structure, more constituent material is shielded inside the particle such that some photoemitted electrons may be reabsorbed by material within the same particle never to escape from the particle [72]. A 2.6 times increase in photoelectric charging efficiency of agglomerates over spheres of the same material and mobility diameter is significantly higher than the 17-30% demonstrated by unipolar diffusion charging [118–121]. With measurements of particle concentration, mobility diameter, and photoelectric yield, the active area multiplier of photoelectric yield may be calculated, thereby giving a measure of the state of sintering.

Figure 6.4b shows the measured photoelectric current, i_o, as a function of a photoelectrically active area, $A_{ph} = \pi N d_{cl}^{3S}$, using a shape factor, S, described in Schmidt-Ott [101] and Eq. 6.3. The shape factor, $S = 2/3$, was selected for the sintered silver particles based on the close-packed particle morphology identified by the SEM images (*i.e.* $d_{cl} = d_m$). For the agglomerated silver particles, it was assumed that the volume equivalent diameter, d_{ve}, represents the equivalent close-packed particle of Eq. 6.3, *i.e.* $d_{cl} = d_{ve}$. The shape factor which produced the lowest coefficient of determination was used. This shape factor was $S = 0.86$, which is comparable to previous values of $S = 0.92$ and $S = 0.74$, for diffusion grown agglomerates determined by experiments and simulation, respectively [101, 124]. The fitting parameter, S, is affected by, but does not explicitly consider, the area of particles exposed to the particles' surroundings. The photoelectrically active area calculated using the fitting parameter, S, requires arbitrary units; this makes physical interpretation difficult.

Using Eqs. 6.4c and 6.7, the photoelectrically active area was calculated accounting for the amount of material exposed to the particle surroundings. Figure 6.4c shows that the photoelectric current, i_o, is nearly the same linear function of photoelectrically active area (Eq. 6.4c) with coefficients of determination of 0.99 and 0.97 for agglomerated and sintered

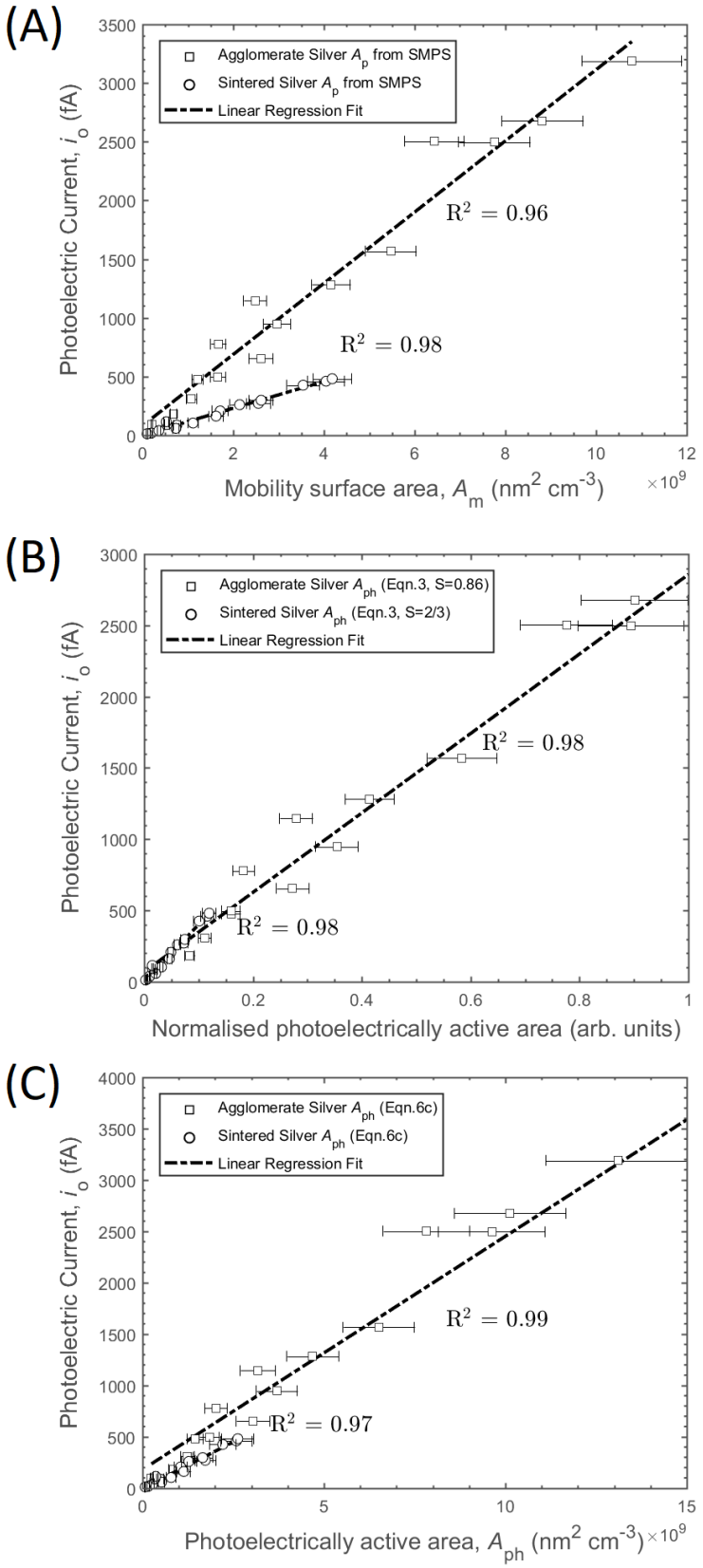

Fig. 6.4 Photoelectric current as a function of (A) mobility surface area (Eq. 6.9) for a monodisperse particle distribution where $A_{\mathrm{m}} \sim\approx \pi N \overline{d}_{\mathrm{m}}^2$, (B) photoelectrically active area ($A_{\mathrm{ph}} = \pi N d_{\mathrm{cl}}^{3S}$ using Eq. 6.3), and (C) photoelectrically active surface area (Eq. 6.4c) for silver agglomerates and close-packed spheres.

silver particles, respectively. Some differences remain between the photoelectric yield of silver agglomerates and sintered spheres for the same photoelectrically active area potentially due to differences in the effect of morphology on particle's electrical capacitance [118] or other changes in surface properties after sintering. However, investigation of these effects is outside the scope of this work. In this work, it has been demonstrated that by defining the photoelectrically active area to include a particle's total surface area exposed to its surroundings (Eq. 6.5), the dependency of photoelectric yield on particle morphology and size are explicitly distinguished.

6.4 Conclusions

Electrical currents resulting from photoemission from aerosol particles have been measured to ascertain the effects of particle size, concentration, material and morphology on photo-emission yield using a fixed-wavelength UV light source. An aerodynamic aerosol classifier was used in series with an electrostatic precipitator to select neutral, monodisperse agglomerated and sintered, close-packed silver spheres in order to determine the photoelectric yield from particles of the same material and different morphologies. Raw and catalytically oxidised carbon agglomerates from a propane flame were measured to demonstrate the effect of different materials in a particle, compared with agglomerated silver. Each of the measured electrical currents is linearly proportional to total particle (mobility) surface area for a range of particle sizes and concentrations of self-similar particle material and morphologies, where agglomerated silver particles have $5\times$ higher photoelectric yield than carbon agglomerates from a propane flame. In this work, it has been shown for the first time that agglomerate particles have a significantly higher photoelectric yield ($2.6\times$) than sintered, close-packed spheres of the same mobility diameter and material, directly contradicting the two most recent of three previous studies which discuss the subject in detail. A sintered, close-packed sphere has less material surface area located externally-to the particle than an agglomerate of the same particle mobility diameter. The mechanisms of photoemission include photon absorption and electron removal from the vicinity of the particle, both of which processes occur for photoemitting material exposed to the particle's surroundings rather than for material shielded inside each particle. Therefore, the photoelectrically active area is defined to include the effect of a particle's morphology. This definition produces good agreement with experimental results. The morphology dependency of aerosol photoemission enables measurements of the particles' active surface area and therefore the state of sintering when the particles' mobility size and concentration are known.

Chapter 7

Conclusions

The aim of this thesis was to develop understanding of the fundamental photoionisation mechanisms and particle and ion transport effects to accurately interpret measurements of ultrafine aerosols and inform low-cost sensor design decisions. The approach was first to develop, verify, and experimentally validate detailed analytical and numerical models by applying the charging and transport equations. Next, the models were applied to understand each of the possible physical mechanisms contributing to photoemission measurements such that they are not conflated with one another or implicitly neglected for a given set of conditions. Finally, photoemission theory was evaluated using experimental measurements interpreted using the understanding gained from modelling analyses.

This thesis introduces the first analysis of simultaneous photoionisation, recombination, convection/diffusion and electrical field transport of multiply-charged particles through a steady-state control volume using analytical and numerical techniques. Analytical equations are used to define characteristic times for photoionisation, recombination, convection, diffusion, and electric field transport mechanisms allowing the formulation of a range of dimensionless parameters to understand the relative contributions of each process. Dimensionless parameters are defined to determine when the effects of electric field or diffusional ion or particle loss require a more computationally expensive numerical model or when the effects may be neglected. The assumptions for the analytical model have been shown to be valid for a range of simple conditions of interest. However, a more detailed numerical model including detailed charge accounting is required for average levels of charge per particle at or below +1 charges, as well as high ion losses.

The computational fluid dynamics (CFD) model developed in this work is the first to include equations capturing UV photoionisation and detailed ion and particle recombination theory. The 0D numerical and 3D CFD models agree well for a large range of electric field strengths for the simple geometry of concentric cylinders, but differences appear at both

high (above ≈8 V cm^{-1}) and low (below ≈0.8 V cm^{-1}) electric field strengths, where the detailed spatial resolution rather than a simple linear 0D model becomes necessary. The results of the analyses using 0D numerical and 3D CFD models demonstrate that the average particle charge level, and the resulting charges at the electrodes and ends of the system can be controlled by changing the bias voltage.

A model for charging polydisperse particle distributions has been constructed. The model considers charge transfer between ions and particles from each of the discrete size bins which make up polydisperse distributions. The results were compared with those from a model assuming a monodisperse particle distribution with the same total concentration at a representative particle size: the diameter of the average surface, $d_{\bar{s}}$, for photoelectric charging. For a representative range of input aerosol parameters and operating conditions, the monodisperse model (44 charge states and coupled charge conservation equations) accurately predicts the electrical current output from a polydisperse particle distribution (represented by 16 size bins $\times$ 44 charge states = 704 simultaneous, coupled charge conservation equations) to within 4.8% and an average of 52$\times$ less computation time. The diameter of the average surface offers a convenient simplification for the conservation equations and for interpreting ultrafine measurements for low-cost devices which use photoelectric charging.

A novel charging and measurement method was introduced by applying an electric field to allow the direct measurement of photoemitted charge from particles captured in the electric field in continuous flow. An applied voltage of 25 V (20 V cm^{-1}) was shown to be nearly optimal for trapping ions at the electrode without largely capturing charged particles for the particular geometry and particle range. The model shows good agreement for measurements of two distinct electrical currents (electrode, i_{e}, and outlet, i_{o}) with those from experimental photoelectric charging of soot particles in a range of sizes and concentrations, for a single fitted parameter for all cases, to account for light intensity. This demonstrates that the physics of the problem is suitably captured by the model and that the method can be used to estimate material dependent fitting parameters such as K_c. At a low applied voltage of 25 V (20 V cm^{-1}), for which $\varepsilon/\delta \approx 2$, a direct measurement of the photoelectrically active surface area of soot particles becomes possible, with an accuracy of within 30% of total surface area, A_{m}, from a SMPS. Mobility diameter is confirmed as a suitable characteristic diameter for use in photoionisation equations, agreeing with previous research.

The charging and measurement method was applied to determine the effect of particle size, concentration and morphology on photo-emission yield using a fixed-wavelength UV light source. An AAC and electrostatic precipitator were used to select neutral, monodisperse agglomerated and sintered, close-packed silver spheres in order to determine the photoelectric yield from particles of the same material and different morphologies. Raw and catalytically

oxidised carbon agglomerates from a propane flame were measured to demonstrate the effect of different materials in a particle, when compared with agglomerated silver. Each of the measured photoelectric currents is linearly proportional to the total (mobility) surface area for a range of particle sizes and concentrations of self-similar particle material and morphologies. It was shown for the first time that agglomerated particles have a significantly higher photoelectric yield (2.6×) than sintered, close-packed spheres of the same mobility diameter and material, contradicting two of the three previous studies. Sintered, close-packed spheres have less material exposed to the UV light and carrier gas than an agglomerate of the same particle mobility diameter. Therefore, the photoelectrically active area is defined to include the number of primary particles exposed to the UV light and carrier gas surrounding the particle. This definition produced good agreement with experimental results. Photoelectric current measurements of aerosols with known particle size and concentration may be used to measure the state of sintering by measuring the photoelectrically active area.

References

[1] William C Hinds. *Aerosol technology: properties, behavior, and measurement of airborne particles, 2nd Ed.* John Wiley & Sons, 1999.

[2] Thomas F Stocker, D Qin, G K Plattner, M Tignor, S K Allen, J Boschung, A Nauels, Y Xia, V Bex, and P M Midgley. Climate change 2013: the physical science basis. intergovernmental panel on climate change, working group I contribution to the IPCC fifth assessment report (AR5). *New York*, 2013.

[3] David Y H Pui, Sheng-Chieh Chen, and Zhili Zuo. PM2.5 in China: Measurements, sources, visibility and health effects, and mitigation. *Particuology*, 13:1–26, 2014.

[4] World Health Organization. Ambient air pollution: A global assessment of exposure and burden of disease. 2016.

[5] Reto Strobel and Sotiris E Pratsinis. Flame aerosol synthesis of smart nanostructured materials. *Journal of Materials Chemistry*, 17(45):4743–4756, 2007.

[6] Pramod Kulkarni, Paul A Baron, and Klaus Willeke. *Aerosol measurement: principles, techniques, and applications*. John Wiley & Sons, 2011.

[7] Rob Beelen, Ole Raaschou-Nielsen, Massimo Stafoggia, Zorana Jovanovic Andersen, Gudrun Weinmayr, Barbara Hoffmann, Kathrin Wolf, Evangelia Samoli, Paul Fischer, Mark Nieuwenhuijsen, et al. Effects of long-term exposure to air pollution on natural-cause mortality: an analysis of 22 European cohorts within the multicentre escape project. *The Lancet*, 383(9919):785–795, 2014.

[8] J Lelieveld, J S Evans, M Fnais, D Giannadaki, and A Pozzer. The contribution of outdoor air pollution sources to premature mortality on a global scale. *Nature*, 525 (7569):367–371, 2015.

[9] Dana Loomis, Yann Grosse, Béatrice Lauby-Secretan, Fatiha El Ghissassi, Véronique Bouvard, Lamia Benbrahim-Tallaa, Neela Guha, Robert Baan, Heidi Mattock, and Kurt Straif. The carcinogenicity of outdoor air pollution. *The Lancet Oncology*, 14 (13):1262–1263, 2013.

[10] U.S. EPA. Integrated Science Assessment for Particulate Matter. (December 2009): 1071, 2009.

[11] Günter Oberdörster, Eva Oberdörster, and Jan Oberdörster. Nanotoxicology: an emerging discipline evolving from studies of ultrafine particles. *Environmental Health Perspectives*, 113(7):823, 2005.

[12] European Commission. COMMISSION REGULATION (EU) No 582/2011 of 25 May 2011 - Heavy Duty. *Official Journal of the European Union*, L 167:1, 2011.

[13] ICAO. Annex 16 Environmental Protection - Volume II: Aircraft Engine Emissions. II(July):99, 2008.

[14] Council of the European Union European Parliament. Directive 2008/50/EC of the European Parliament and of the Council of 21 May 2008 on ambient air quality and cleaner air for Europe. *Official Journal of the European*, 152:1–43, 2008.

[15] World Health Organization. WHO guidelines for indoor air quality: selected pollutants. 2010.

[16] Richard W. Baldauf, Robert B. Devlin, Peter Gehr, Robert Giannelli, Beth Hassett-Sipple, Heejung Jung, Giorgio Martini, Joseph McDonald, Jason D. Sacks, and Katherine Walker. Ultrafine particle metrics and research considerations: Review of the 2015 UFP workshop. *International Journal of Environmental Research and Public Health*, 13(11):1–21, 2016.

[17] S Bau, B Zimmermann, R Payet, and O Witschger. A laboratory study of the performance of the handheld diffusion size classifier (DiSCmini) for various aerosols in the 15–400 nm range. *Environmental Science: Processes & Impacts*, 17(2):261–269, 2015.

[18] M I Mead, O A M Popoola, G B Stewart, P Landshoff, M Calleja, M Hayes, J J Baldovi, M W McLeod, T F Hodgson, J Dicks, et al. The use of electrochemical sensors for monitoring urban air quality in low-cost, high-density networks. *Atmospheric Environment*, 70:186–203, 2013.

[19] Wayne R Ott and Hans C Siegmann. Using multiple continuous fine particle monitors to characterize tobacco, incense, candle, cooking, wood burning, and vehicular sources in indoor, outdoor, and in-transit settings. *Atmospheric Environment*, 40(5):821–843, 2006.

[20] Prashant Kumar, Lidia Morawska, Claudio Martani, George Biskos, Marina Neophytou, Silvana Di Sabatino, Margaret Bell, Leslie Norford, and Rex Britter. The rise of low-cost sensing for managing air pollution in cities. *Environment International*, 75: 199–205, 2015.

[21] Derk H. Brouwer, José H.J. Gijsbers, and Marc W.M. Lurvink. Personal exposure to ultrafine particles in the workplace: Exploring sampling techniques and strategies. *Annals of Occupational Hygiene*, 48(5):439–453, 2004.

[22] D B Kittelson, W F Watts, J C Savstrom, and J P Johnson. Influence of a catalytic stripper on the response of real time aerosol instruments to diesel exhaust aerosol. *Journal of Aerosol Science*, 36(9):1089–1107, 2005.

[23] Shih Chen Wang and Richard C Flagan. Scanning electrical mobility spectrometer. *Aerosol Science and Technology*, 13(2):230–240, 1990.

[24] ISO. BS ISO 15900: 2009 (E) Determination of particle size distribution–differential electrical mobility analysis for aerosol particles, 2009.

[25] N A Fuchs. On the stationary charge distribution on aerosol particles in a bipolar ionic atmosphere. *Geofisica Pura E Applicata*, 56(1):185–193, 1963.

[26] A Wiedensohler. An approximation of the bipolar charge distribution for particles in the submicron size range. *Journal of Aerosol Science*, 19(3):387–389, 1988.

[27] Benjamin Y H Liu and David Y H Pui. A submicron aerosol standard and the primary, absolute calibration of the condensation nuclei counter. *Journal of Colloid And Interface Science*, 47(1):155–171, 1974.

[28] Farzan Tavakoli, Jonathan P R Symonds, and Jason S Olfert. Generation of a monodisperse size-classified aerosol independent of particle charge. *Aerosol Science and Technology*, 48(3):i–iv, 2014.

[29] Tyler J Johnson, Martin Irwin, Jonathan PR Symonds, Jason S Olfert, and Adam M Boies. Measuring aerosol size distributions with the aerodynamic aerosol classifier. *Aerosol Science and Technology*, 52(6):655–665, 2018.

[30] Peter F DeCarlo, Jay G Slowik, Douglas R Worsnop, Paul Davidovits, and Jose L Jimenez. Particle morphology and density characterization by combined mobility and aerodynamic diameter measurements. Part 1: Theory. *Aerosol Science and Technology*, 38(12):1185–1205, 2004.

[31] Tim Johnson, Robert Caldow, Arndt Poecher, Aadu Mirme, and David Kittelson. A new electrical mobility particle sizer spectrometer for engine exhaust particle measurements. Technical report, SAE Technical Paper, 2004.

[32] Kingsley Reavell, Tim Hands, and Nick Collings. A fast response particulate spectrometer for combustion aerosols. Technical report, SAE Technical Paper, 2002.

[33] J. Keskinen, K. Pietarinen, and M. Lehtimäki. Electrical low pressure impactor. *Journal of Aerosol Science*, 23(4):353–360, 1992.

[34] Virgil A Marple, Kenneth L Rubow, and Steven M Behm. A microorifice uniform deposit impactor (MOUDI): Description, calibration, and use. *Aerosol Science and Technology*, 14(4):434–436, 1991.

[35] J S Olfert and N Collings. New method for particle mass classification—the couette centrifugal particle mass analyzer. *Journal of Aerosol Science*, 36(11):1338–1352, 2005.

[36] Kensei Ehara, Charles Hagwood, and Kevin J Coakley. Novel method to classify aerosol particles according to their mass-to-charge ratio—aerosol particle mass analyser. *Journal of Aerosol Science*, 27(2):217–234, 1996.

[37] Christof Asbach, Heinz Kaminski, Daniel Von Barany, Thomas A J Kuhlbusch, Christian Monz, Nico Dziurowitz, Johannes Pelzer, Katja Vossen, Knut Berlin, Silvio Dietrich, et al. Comparability of portable nanoparticle exposure monitors. *Annals of Occupational Hygiene*, 56(5):606–621, 2012.

[38] Harry J White. Particle charging in electrostatic precipitation. *Transactions of the American Institute of Electrical Engineers*, 70(2):1186–1191, 1951.

[39] Johan Marra, Matthias Voetz, and Heinz-Jürgen Kiesling. Monitor for detecting and assessing exposure to airborne nanoparticles. *Journal of Nanoparticle Research*, 12 (1):21–37, 2010.

[40] Heejung Jung and David B Kittelson. Characterization of aerosol surface instruments in transition regime. *Aerosol Science and Technology*, 39(9):902–911, 2005.

[41] M Fierz, C Houle, P Steigmeier, and H Burtscher. Design, calibration, and field performance of a miniature diffusion size classifier. *Aerosol Science and Technology*, 45(1):1–10, 2011.

[42] Ana Maria Todea, Stefanie Beckmann, Heinz Kaminski, and Christof Asbach. Accuracy of electrical aerosol sensors measuring lung deposited surface area concentrations. *Journal of Aerosol Science*, 89:96–109, 2015.

[43] H Smith. Human respiratory tract model for radiological protection. *ICRP publication 66*, 1994.

[44] H Burtscher and H C Siegmann. Monitoring PAH-emissions from combustion processes by photoelectric charging. *Combustion Science and Technology*, 101(1-6): 327–332, 1994.

[45] D Dahmann, T Mosimann, and U Matter. Validation of online sensors for monitoring occupational exposures from diesel engines. *Journal of Aerosol Science*, (31):21–22, 2000.

[46] Heinz Burtscher. Measurement and characteristics of combustion aerosols with special consideration of photoelectric charging and charging by flame ions. *Journal of Aerosol Science*, 23(6):549–595, 1992.

[47] A Schmidt-Ott, U Baltensperger, H W Gäggeler, and D T Jost. Scaling behaviour of physical parameters describing agglomerates. *Journal of Aerosol Science*, 21(6): 711–717, 1990.

[48] A Keller, M Fierz, K Siegmann, H C Siegmann, and A Filippov. Surface science with nanosized particles in a carrier gas. *Journal of Vacuum Science & Technology A: Vacuum, Surfaces, and Films*, 19(1):1–8, 2001.

[49] Heinz Burtscher, Stefan Künzel, and Christoph Hüglin. Characterization of particles in combustion engine exhaust. *Journal of Aerosol Science*, 29(4):389–396, 1998.

[50] R Niessner. The chemical response of the photo-electric aerosol sensor (PAS) to different aerosol systems. *Journal of Aerosol Science*, 17(4):705–714, 1986.

[51] Lei Zhou, Rian You, Jiaojie Tan, and Michael R Zachariah. Wavelength-resolved UV photoelectric charging dynamics of nanoparticles: comparison of spheres and aggregates. *Aerosol Science and Technology*, 47(6):672–680, 2013.

[52] Peter Kallinger, Gerhard Steiner, and Wladyslaw W Szymanski. Characterization of four different bipolar charging devices for nanoparticle charge conditioning. *Journal of Nanoparticle Research*, 14(6):944, 2012.

[53] Panich Intra and Nakorn Tippayawong. An overview of unipolar charger developments for nanoparticle charging. *Aerosol and Air Quality Research*, 11:187–209, 2011.

[54] Heinz Kaminski, Thomas A J Kuhlbusch, Heinz Fissan, Lavanya Ravi, Hans-Georg Horn, Hee-Siew Han, Rob Caldow, and Christof Asbach. Mathematical description of experimentally determined charge distributions of a unipolar diffusion charger. *Aerosol Science and Technology*, 46(6):708–716, 2012.

[55] G Biskos, K Reavell, and N Collings. Description and theoretical analysis of a differential mobility spectrometer. *Aerosol Science and Technology*, 39(6):527–541, 2005.

[56] B Grob, H Burtscher, and R Niessner. Charging of ultra-fine aerosol particles by an ozone-free indirect uv photo-charger. *Aerosol Science and Technology*, 47(12): 1325–1333, 2013.

[57] D Matter, M Mohr, W Fendel, A Schmidt-Ott, and H Burtscher. Multiple wavelength aerosol photoemission by excimer lamps. *Journal of Aerosol Science*, 26(7):1101–1115, 1995.

[58] Jingkun Jiang, Myong-Hwa Lee, and Pratim Biswas. Model for nanoparticle charging by diffusion, direct photoionization, and thermionization mechanisms. *Journal of electrostatics*, 65(4):209–220, 2007.

[59] Manuel Cardona and Lothar Ley. *Photoemission in Solids I: General Principles*. Springer-Verlag, 1978.

[60] A Einstein. On a heuristic point of view concerning the production and transformation of light. *Annalen der Physik*, 17:132–148, 1905.

[61] A Schmidt-Ott and H C Siegmann. Photoelectron emission from small particles suspended in air. *Applied Physics Letters*, 32(11):710–713, 1978.

[62] Th Jung, H Burtscher, and A Schmidt-Ott. Multiple charging of ultrafine aerosol particles by aerosol photoemission (APE). *Journal of Aerosol Science*, 19(4):485–490, 1988.

[63] Martin Mohr, Daniel Matter, and Heinz Burtscher. Efficient multiple charging of diesel particles by photoemission. *Aerosol science and technology*, 24(1):14–20, 1996.

[64] Lin Li and Da-Ren Chen. Aerosol charging using pen-type UV lamps. *Aerosol and Air Quality Research*, 11(7):791–801, 2011.

[65] N Bukowiecki, D B Kittelson, W F Watts, H Burtscher, E Weingartner, and U Baltensperger. Real-time characterization of ultrafine and accumulation mode particles in ambient combustion aerosols. *Journal of Aerosol Science*, 33(8):1139–1154, 2002.

[66] Esther Hontañón and F Einar Kruis. Single charging of nanoparticles by uv photoionization at high flow rates. *Aerosol Science and Technology*, 42(4):310–323, 2008.

[67] Pramod Kulkarni, Norikazu Namiki, Yoshio Otani, and Pratim Biswas. Charging of particles in unipolar coronas irradiated by in-situ soft X-rays: enhancement of capture efficiency of ultrafine particles. *Journal of Aerosol Science*, 33(9):1279–1296, 2002.

[68] Christopher J Hogan, Myong-Hwa Lee, and Pratim Biswas. Capture of viral particles in soft X-ray–enhanced corona systems: charge distribution and transport characteristics. *Aerosol Science and Technology*, 38(5):475–486, 2004.

[69] Jeong Hoon Byeon and Jeffrey T Roberts. Photoionization of nanosized aerosol gold agglomerates and their deposition to form nanoscale islands on substrates. *Langmuir*, 30(29):8770–8775, 2014.

[70] H Burtscher, L Scherrer, H C Siegmann, A Schmidt-Ott, and B Federer. Probing aerosols by photoelectric charging. *Journal of Applied Physics*, 53(5):3787–3791, 1982.

[71] Alfred P Weber, Martin Seipenbusch, and Gerhard Kasper. Application of aerosol techniques to study the catalytic formation of methane on gasborne nickel nanoparticles. *The Journal of Physical Chemistry A*, 105(39):8958–8963, 2001.

[72] Alfred P Weber, Martin Seipenbusch, Christoph Thanner, and Gerhard Kasper. Aerosol catalysis on nickel nanoparticles. *Journal of Nanoparticle Research*, 1(2):253–265, 1999.

[73] Jannis Röhrbein and Alfred P Weber. A system for on-line characterization of gasborne particle surface properties based on their photoemission. *Journal of Aerosol Science*, 2018.

[74] William E Spicer. Possible non-one-electron effects in the fundamental optical excitation spectra of certain crystalline solids and their effect on photoemission. *Physical Review*, 154(2):385, 1967.

[75] Arkadi Maisels, Frank Jordan, and Heinz Fissan. Dynamics of the aerosol particle photocharging process. *Journal of applied Physics*, 91(5):3377–3383, 2002.

[76] U Müller, A Schmidt-Ott, and H Burtscher. Photoelectric quantum yield of free silver particles near threshold. *Zeitschrift für Physik B Condensed Matter*, 73(1):103–106, 1988.

[77] A Schmidt-Ott and B Federer. Photoelectron emission from small particles suspended in a gas. *Surface Science*, 106(1-3):538–543, 1981.

[78] Jingkun Jiang, Christopher J Hogan Jr, Da-Ren Chen, and Pratim Biswas. Aerosol charging and capture in the nanoparticle size range (6–15 nm) by direct photoionization and diffusion mechanisms. *Journal of Applied Physics*, 102(3):034904, 2007.

[79] Anna Leonardi. *Feinste schwebeteilchen aus dieselmotoren*. PhD thesis, ETH Zurich, 1991.

[80] Arkadi Maisels, Frank Jordan, and Heinz Fissan. On the effect of charge recombination on the aerosol charge distribution in photocharging systems. *Journal of Aerosol Science*, 34(1):117–132, 2003.

[81] David M Wood. Classical size dependence of the work function of small metallic spheres. *Physical Review Letters*, 46(11):749, 1981.

[82] Herbert B Michaelson. The work function of the elements and its periodicity. *Journal of Applied Physics*, 48(11):4729–4733, 1977.

[83] Anne Maißer, Jikku M Thomas, Carlos Larriba-Andaluz, Siqin He, and Christopher J Hogan. The mass–mobility distributions of ions produced by a Po-210 source in air. *Journal of Aerosol Science*, 90:36–50, 2015.

[84] William A Hoppel and Glendon M Frick. Ion—aerosol attachment coefficients and the steady-state charge distribution on aerosols in a bipolar ion environment. *Aerosol Science and Technology*, 5(1):1–21, 1986.

[85] Y G Stommel and Ulrich Riebel. Comment on the calculation of the steady-state charge distribution on aerosols< 100 nm by three body trapping method in a bipolar ion environment. *Aerosol Science and Technology*, 41(9):840–847, 2007.

[86] Xerxes López-Yglesias and Richard C Flagan. Ion–aerosol flux coefficients and the steady-state charge distribution of aerosols in a bipolar ion environment. *Aerosol Science and Technology*, 47(6):688–704, 2013.

[87] Ranganathan Gopalakrishnan, Mark J Meredith, Carlos Larriba-Andaluz, and Christopher J Hogan Jr. Brownian dynamics determination of the bipolar steady state charge distribution on spheres and non-spheres in the transition regime. *Journal of Aerosol Science*, 63:126–145, 2013.

[88] Georg P Reischl, J M Mäkelä, R Karch, and J Necid. Bipolar charging of ultrafine particles in the size range below 10 nm. *Journal of Aerosol Science*, 27(6):931–949, 1996.

[89] A Schmidt-Ott, P Schurtenberger, and H C Siegmann. Enormous yield of photoelectrons from small particles. *Physical Review Letters*, 45(15):1284, 1980.

[90] B Schleicher, H Burtscher, and H C Siegmann. Photoelectric quantum yield of nanometer metal particles. *Applied Physics Letters*, 63(9):1191–1193, 1993.

[91] H Burtscher, R. Niessner, and A. Schmidt-Ott. In situ detection by photoelectron emission of PAH enriched on particles surfaces. In *Aerosols, Science, Technology and Industrial Applications of Airborne Particles*, pages pp. 443–446. Elsevier New York, 1984.

[92] Reinhard Niessner and Peter Wilbring. Ultrafine particles as trace catchers for polycyclic aromatic hydrocarbons: the photoelectric aerosol sensor as a tool for in situ sorption and desorption studies. *Analytical Chemistry*, 61(7):708–714, 1989.

[93] Stephen R McDow, Walter Giger, Heinz Burtscher, Andreas Schmidt-Ott, and Hans C Siegmann. Polycyclic aromatic hydrocarbons and combustion aerosol photoemission. *Atmospheric Environment. Part A. General Topics*, 24(12):2911–2916, 1990.

[94] M Rosatzin and H Burtscher. Improved aerosol-photoemission sensor for detection of particulate emissions from combustions. *Journal of Aerosol Science*, 19(5):633–637, 1988.

[95] H Burtscher, A Schmidt-Ott, and H C Siegmann. Monitoring particulate emissions from combustions by photoemission. *Aerosol Science and Technology*, 8(2):125–132, 1988.

[96] U Müller, H Burtscher, and A Schmidt-Ott. Photoemission from small metal spheres: A model calculation using an enhanced three-step model. *Physical Review B*, 38(11): 7814, 1988.

[97] Martin Mohr and Heinz Burtscher. Photoelectric aerosol charging at high particle concentrations. *Journal of Aerosol Science*, 28(4):613–621, 1997.

[98] H Burtscher. Physical characterization of particulate emissions from diesel engines: a review. *Journal of Aerosol Science*, 36(7):896–932, 2005.

[99] U Matter, H C Siegmann, and H Burtscher. Dynamic field measurements of submicron particles from diesel engines. *Environmental science & technology*, 33(11):1946–1952, 1999.

[100] Qian Zhiqiang, Konstantin Siegmann, Alejandro Keller, Ulrich Matter, Leo Scherrer, and H C Siegmann. Nanoparticle air pollution in major cities and its origin. *Atmospheric Environment*, 34(3):443–451, 2000.

[101] A Schmidt-Ott. New approaches to in situ characterization of ultrafine agglomerates. *Journal of Aerosol Science*, 19(5):553–563, 1988.

[102] Lei Zhou and Michael R Zachariah. Size resolved particle work function measurement of free nanoparticles: Aggregates vs. spheres. *Chemical Physics Letters*, 525:77–81, 2012.

[103] T Van der Zwaag, S Haep, and K G Schmidt. Simulation of electrical effects with respect to fine particle separation at conditions of pressurized pulverized coal combustion. *Powder Technology*, 180(1-2):97–101, 2008.

[104] G Kasper. Electrostatic dispersion of homopolar charged aerosols. *Journal of Colloid and Interface Science*, 81(1):32–40, 1981.

[105] A Wiedensohler, E Lütkemeier, M Feldpausch, and C Helsper. Investigation of the bipolar charge distribution at various gas conditions. *Journal of Aerosol Science*, 17 (3):413–416, 1986.

[106] Gerhard Steiner, Tuija Jokinen, Heikki Junninen, Mikko Sipilä, Tuukka Petäjä, Douglas Worsnop, Georg P Reischl, and Markku Kulmala. High-resolution mobility and mass spectrometry of negative ions produced in a 241am aerosol charger. *Aerosol Science and Technology*, 48(3):261–270, 2014.

[107] Keithley Instruments, Inc. *Model 6517B Reference Manual, Revision B*. 2009.

[108] TSI Inc. *Model 3068B Aerosol Electrometer, User's Manual, Revision A*. 2006.

[109] Marc E J Stettler, Jacob J Swanson, Steven R H Barrett, and Adam M Boies. Updated correlation between aircraft smoke number and black carbon concentration. *Aerosol Science and Technology*, 47(11):1205–1214, 2013.

[110] Tyler Johnson, Robert Nishida, Martin Irwin, Jonathan Symonds, Jason S. Olfert, and Adam Boies. Uniformity of Particle Concentration after Mixing Aerosol Flows. In *Cambridge Particle Meeting*, Cambridge, UK. June 15, 2018., 2018.

[111] George W Mulholland, Michelle K Donnelly, Charles R Hagwood, Scott R Kukuck, Vincent A Hackley, and David Y H Pui. Measurement of 100 nm and 60 nm particle standards by differential mobility analysis. *Journal of Research of the National Institute of Standards and Technology*, 111(4):257, 2006.

[112] TSI Inc. *Model 3776 Ultrafine Condensation Particle Counter: Operation and Service Manual, Revision B*. 2006.

[113] A Wiedensohler, W Birmili, A Nowak, A Sonntag, K Weinhold, M Merkel, B Wehner, T Tuch, S Pfeifer, Markus Fiebig, et al. Mobility particle size spectrometers: harmonization of technical standards and data structure to facilitate high quality long-term observations of atmospheric particle number size distributions. *Atmospheric Measurement Techniques*, 5:657–685, 2012.

[114] R B Bird, W E Stewart, and E N Lightfoot. *Transport Phenomena*. John Wiley & Sons, Inc., New York, 1960.

[115] Leo N Y Cao, Sheng-Chieh Chen, Heinz Fissan, Christof Asbach, and David Y H Pui. Development of a geometric surface area monitor (GSAM) for aerosol nanoparticles. *Journal of Aerosol Science*, 114:118–129, 2017.

[116] Leo N Y Cao and David Y H Pui. A novel weighted sum method to measure particle geometric surface area in real-time. *Journal of Aerosol Science*, 117:11–23, 2018.

[117] H Burtscher, A Schmidt-Ott, and H C Siegmann. Photoelectron yield of small silver and gold particles suspended in gas up to a photon energy of 10 eV. *Zeitschrift für Physik B Condensed Matter*, 56(3):197–199, 1984.

[118] Leo N Y Cao, Jing Wang, Heinz Fissan, Sotiris E Pratsinis, Max L Eggersdorfer, and David YH Pui. The capacitance and charge of agglomerated nanoparticles during sintering. *Journal of Aerosol Science*, 83:1–11, 2015.

[119] Weon Gyu Shin, Jing Wang, Michael Mertler, Bernd Sachweh, Heinz Fissan, and David Y H Pui. The effect of particle morphology on unipolar diffusion charging of nanoparticle agglomerates in the transition regime. *Journal of Aerosol Science*, 41 (11):975–986, 2010.

[120] J Wang, W G Shin, M Mertler, B Sachweh, H Fissan, and D Y H Pui. Measurement of nanoparticle agglomerates by combined measurement of electrical mobility and unipolar charging properties. *Aerosol Science and Technology*, 44(2):97–108, 2010.

[121] Hyuncheol Oh, Hyungho Park, and Sangsoo Kim. Effects of particle shape on the unipolar diffusion charging of nonspherical particles. *Aerosol Science and Technology*, 38(11):1045–1053, 2004.

[122] F Einar Kruis, Karl A Kusters, Sotiris E Pratsinis, and Brian Scarlett. A simple model for the evolution of the characteristics of aggregate particles undergoing coagulation and sintering. *Aerosol Science and Technology*, 19(4):514–526, 1993.

[123] Max L Eggersdorfer, Dirk Kadau, Hans J Herrmann, and Sotiris E Pratsinis. Aggregate morphology evolution by sintering: number and diameter of primary particles. *Journal of Aerosol Science*, 46:7–19, 2012.

[124] Paul Meakin and T A Witten Jr. Growing interface in diffusion-limited aggregation. *Physical Review A*, 28(5):2985, 1983.

[125] Steven N Rogak, Richard C Flagan, and Hung V Nguyen. The mobility and structure of aerosol agglomerates. *Aerosol Science and Technology*, 18(1):25–47, 1993.

[126] Peter H McMurry, Xin Wang, Kihong Park, and Kensei Ehara. The relationship between mass and mobility for atmospheric particles: A new technique for measuring particle density. *Aerosol Science & Technology*, 36(2):227–238, 2002.

[127] Adam M Boies, Marc E J Stettler, Jacob J Swanson, Tyler J Johnson, Jason S Olfert, Mark Johnson, Max L Eggersdorfer, Theo Rindlisbacher, Jing Wang, Kevin Thomson, et al. Particle emission characteristics of a gas turbine with a double annular combustor. *Aerosol Science and Technology*, 49(9):842–855, 2015.

[128] W A Hoppel and G M Frick. The nonequilibrium character of the aerosol charge distributions produced by neutralizes. *Aerosol Science and Technology*, 12(3):471–496, 1990.

Appendix A

Governing Equations

A.1 General governing equations

The following are the particle (Eq. A.1a) and ion (Eqs. A.1b and A.1c) charging and conservation equations general to bipolar and unipolar diffusion chargers and photoelectric chargers where the polydisperse particles are of a single material type and ions of each polarity are assumed to be of monodisperse mobility. The net current measurement of Eq. A.1d is relevant to low-cost unipolar diffusion charging devices where electrical current measurements are proportional sum of the charge carried with the particles.

$$\begin{aligned}\nabla\cdot\left(\vec{u}N_{b,q}\right) &= \nabla\cdot\left(D_{b,q}\nabla N_{b,q}\right)+\nabla\cdot\left(Z_{b,q}\vec{E}N_{b,q}\right)\\ &\quad+\alpha_b^{q-1\to q}N_{b,q-1}-\alpha_b^{q\to q+1}N_{b,q}\\ &\quad+\beta_b^{q+1\to q}N_{b,q+1}n_{-1}-\beta_b^{q\to q-1}N_{b,q}n_{-1}\\ &\quad+\beta_b^{q-1\to q}N_{b,q-1}n_{+1}-\beta_b^{q\to q+1}N_{b,q}n_{+1}\end{aligned} \tag{A.1a}$$

$$\begin{aligned}\nabla\cdot\left(\vec{u}n_{-1}\right) &= \nabla\cdot\left(D_{\mathrm{i,-1}}\nabla n_{-1}\right)+\nabla\cdot\left(Z_{\mathrm{i,-1}}\vec{E}n_{-1}\right)\\ &\quad+\sum_{b=1}^{M}\sum_{q=q_{\min}}^{q_{\max}}\left(\alpha_b^{q\to q+1}N_{b,q}-\beta_b^{q\to q-1}N_{b,q}n_{-1}\right)-an_{+1}n_{-1}\end{aligned} \tag{A.1b}$$

$$\begin{aligned}\nabla\cdot\left(\vec{u}n_{+1}\right) &= \nabla\cdot\left(D_{\mathrm{i,+1}}\nabla n_{+1}\right)+\nabla\cdot\left(Z_{\mathrm{i,+1}}\vec{E}n_{+1}\right)\\ &\quad-\sum_{b=1}^{M}\sum_{q=q_{\min}}^{q_{\max}}\left(\beta_b^{q\to q+1}N_{b,q}n_{+1}\right)-an_{-1}n_{+1}\end{aligned} \tag{A.1c}$$

$$\begin{aligned}i &= \int_A\sum_{b=1}^{M}\sum_{q=q_{\min}}^{q_{\max}}\left(qe\vec{u}N_{b,q}+qeD_{b,q}\nabla N_{b,q}+qeZ_{b,q}\vec{E}N_{b,q}\right)\cdot\mathrm{d}A\\ &\quad-\int_A\left(e\vec{u}n_{-1}+eD_{\mathrm{i,-1}}\nabla n_{-1}+eZ_{\mathrm{i,-1}}\vec{E}n_{-1}\right)\cdot\mathrm{d}A\\ &\quad+\int_A\left(e\vec{u}n_{+1}+eD_{\mathrm{i,+1}}\nabla n_{+1}+eZ_{\mathrm{i,+1}}\vec{E}n_{+1}\right)\ \mathrm{d}A\end{aligned} \tag{A.1d}$$

Table A.1 Terms in governing equations for monodisperse, polydisperse, and 0D numerical models of photoelectric and diffusion charging.

		3D CFD	3D CFD	0D numerical
		polydisperse	monodisperse	monodisperse
Particles	Convection	$\nabla \cdot \left(\vec{u} N_{b,q}\right)$	$\nabla \cdot \left(\vec{u} N_q\right)$	$\frac{dN_q}{dt}$
	Diffusion	$\nabla \cdot \left(D_{b,q} \nabla N_{b,q}\right)$	$\nabla \cdot \left(D \nabla N_q\right)$	$-\frac{4D_p}{R^2} N_q$
	Electric Field	$\nabla \cdot \left(Z_{b,q} \vec{E} N_{b,q}\right)$	$\nabla \cdot \left(Z_q \vec{E} N_q\right)$	$-\frac{Z_p E}{R} N_q$
	Photoionisation	$\alpha_b^{q-1 \to q} N_{b,q-1}$	$\alpha^{q-1 \to q} N_{q-1}$	$\alpha^{q-1 \to q} N_{q-1}$
		$-\alpha_b^{q \to q+1} N_{b,q}$	$-\alpha^{q \to q+1} N_q$	$-\alpha^{q \to q+1} N_q$
	Recombination	$\beta_b^{q+1 \to q} N_{b,q+1} n_{-1}$	$\beta^{q+1 \to q} N_{q+1} n_{-1}$	$\beta^{q+1 \to q} N_{q+1} n_{-1}$
		$-\beta_b^{q \to q-1} N_{b,q} n_{-1}$	$-\beta^{q \to q-1} N_q n_{-1}$	$-\beta^{q \to q-1} N_q n_{-1}$
Ions	Convection	$\nabla \cdot (\vec{u} n_{-1})$	$\nabla \cdot (\vec{u} n_{-1})$	$\frac{dn_{-1}}{dt}$
	Diffusion	$\nabla \cdot (D_i \nabla n_{-1})$	$\nabla \cdot (D_i \nabla n_{-1})$	$-\frac{4D_i}{R^2} n_{-1}$
	Electric Field	$\nabla \cdot \left(Z_{-1} \vec{E} n_{-1}\right)$	$\nabla \cdot \left(Z_{-1} \vec{E} n_{-1}\right)$	$-\frac{Z_{-1} E}{R} n_{-1}$
	Photoionisation	$\sum_{b=1}^{M} \sum_{q=q_{\min}}^{q_{\max}} \alpha_b^{q \to q+1} N_{b,q}$	$\sum_{q=q_{\min}}^{q_{\max}} \alpha^{q \to q+1} N_q$	$\sum_{q=q_{\min}}^{q_{\max}} \alpha^{q \to q+1} N_q$
	Recombination	$-\sum_{b=1}^{M} \sum_{q=q_{\min}}^{q_{\max}} \beta_b^{q \to q-1} N_{b,q} n_{-1}$	$-\sum_{q=q_{\min}}^{q_{\max}} \beta^{q \to q-1} N_q n_{-1}$	$-\sum_{q=q_{\min}}^{q_{\max}} \beta^{q \to q-1} N_q n_{-1}$

Appendix B

Model Verification

The 0D numerical model is verified against existing numerical models from Hoppel and Frick [128], and Maisels et al. [75]. In the 0D numerical model, the divergence terms for advection, diffusion and electric field transport are replaced by rate terms as shown in Table A.1.

B.1 0D numerical model

The 0D numerical model is compared against a numerical model from Hoppel and Frick [128] for the concentration of ions and charged particles over time and shown in Fig. A.1. There is a constant generation rate of positive (n_+) and negative ions (n_-) in a 0D case. The ions transfer charge to the particles through a diffusion charging process. The differences in results at the steady-state values relate to the assumptions made in the collision kernels of Hoppel and Frick [128]. The 0D numerical model contains a more detailed calculation of mean free path (Reischl et al. [88]) and other properties.

An analytical equation from Wiedensohler [26] estimates the Fuchs distribution found after the recombination process reaches an equilibrium. The fractions of multiply charged particles are calculated using the 0D numerical model with ion mobilities from Wiedensohler [26]. Fig. A.2 shows the 0D numerical model matches Fuchs equilibrium charge distribution after a sufficient charging time. The differences relate to the assumptions made in the analytical equation of Wiedensohler [26].

Charge level per particle is shown as a function of time for a range of concentrations in Fig A.3. The aerosol particles are irradiated with UV light which causes an increase in charges per particle. At high concentrations, recombination is more likely, thereby decreasing the charging per particle. An equilibrium state is reached in which photoionisation rate matches the recombination rate. The aerosol is no longer irradiated beyond t = 0.71 s, therefore

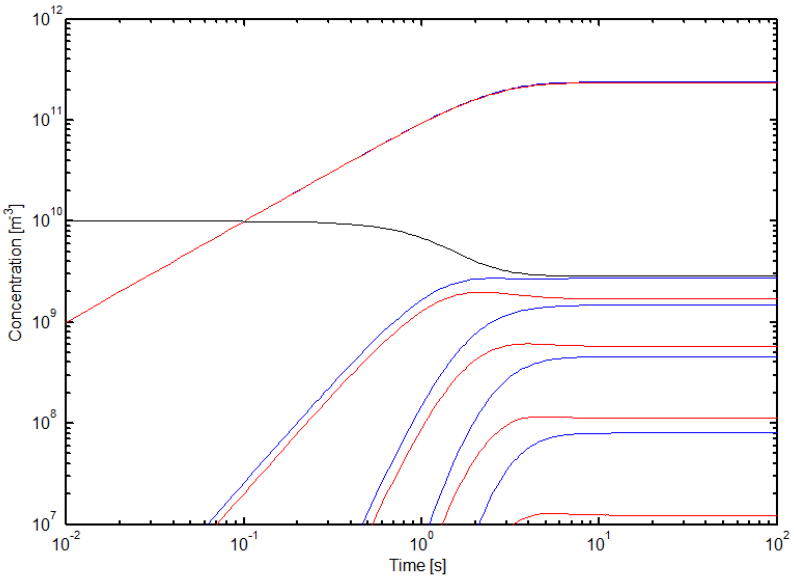

Fig. A.1 Asymmetric diffusion charging of particles (d = 200 nm) for ionisation rate 10^5 ion pairs cm^{-1} s^{-1}.

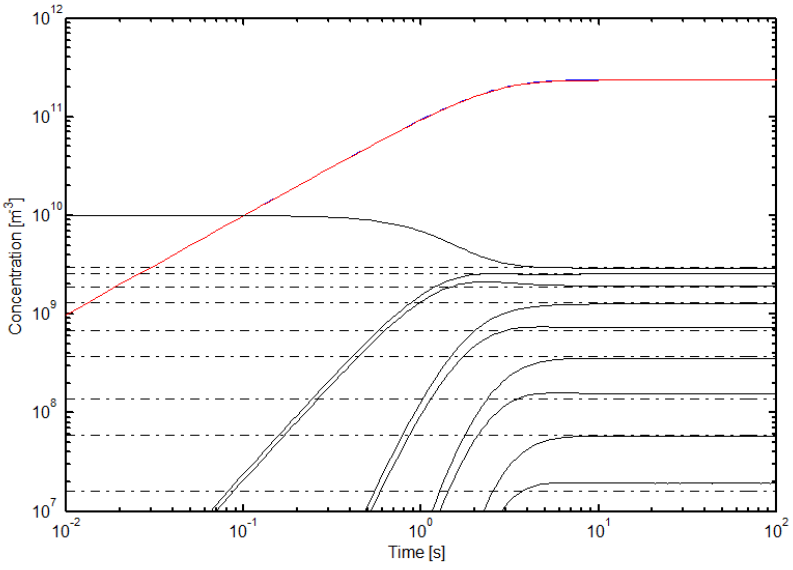

Fig. A.2 0D numerical - Asymmetric diffusion charging of particles (D_p = 200 nm) for ionisation rate 10^5 ion pairs cm^{-1} s^{-1}. Photoionisation is turned off in this case. The fraction of multiply charged particles in a Fuch's distribution are estimated using an analytical equation from Wiedensohler [26] (dotted lines).

recombination dominates. The present 0D numerical model shows excellent agreement with the numerical model and conditions of Maisels et al. [75] summarised in Table B.1.

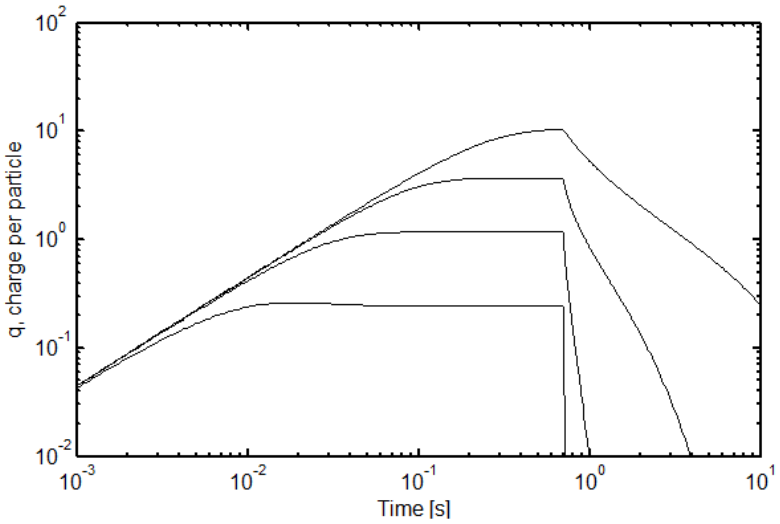

Fig. A.3 Photoionisation is combined with the diffusion charging process. The 0D numerical model corresponds to the dots of Maisels et al. [75] which represent the numerical model. The solid lines in Maisels et al. [75] represent an analytical model which is only valid for high charging levels. The aerosol flow leaves the irradiated region at t=0.71 s.

Table B.1 Model properties and operating conditions used for model verification and to explore effect of electrical field transport and capture of ions and particles.

Parameter	Symbol	Units	Value
Negative ion diffusivity	D_{-1}	$m^2\ s^{-1}$	3.41×10^{-6}
Negative ion electrical mobility	Z_{-1}	$m^2\ V^{-1}\ s^{-1}$	1.6×10^{-4}
Particle diameter	d	nm	53
Bulk velocity	U	$m\ s^{-1}$	3.45×10^{-2}
Empirical constant	m		2
Photoemission constant	K_cI	$J^{-1}\ m^{-2}\ s^{-1}$	4.38×10^{34}
Light energy	hv	eV (nm)	7.203 (172)
Work function	Φ_∞	eV	2.5

B.2 Computational Fluid Dynamics model

Equations for photoionisation and recombination theory are applied in 3D CFD and verified against existing numerical models from Hoppel and Frick [128] and the 0D numerical model.

The equations were first applied in a 1D CFD model in which boundary effects were neglected for comparison.

Results from the numerical model from Hoppel and Frick [128] are compared against the CFD model for the concentration of ions and charged particles over time and shown in Figure A.4. There is a constant generation rate of positive (n_+) and negative ions (n_-) in a 1D case. The ions transfer charge to the particles through a diffusion charging process. The charging is asymmetric due to the increased mobility of the negative ions over the positive ions. Photoionisation is turned off in this case.

The 0D numerical and CFD models are compared for photoionisation and recombination processes and results are shown in Figures A.5. Negative ions and positively charged particles are produced due to photoionisation. Concentrations of particles at higher charge levels become more significant as photoelectric charging proceeds until an equilibrium state is reached. The agreement between models is excellent.

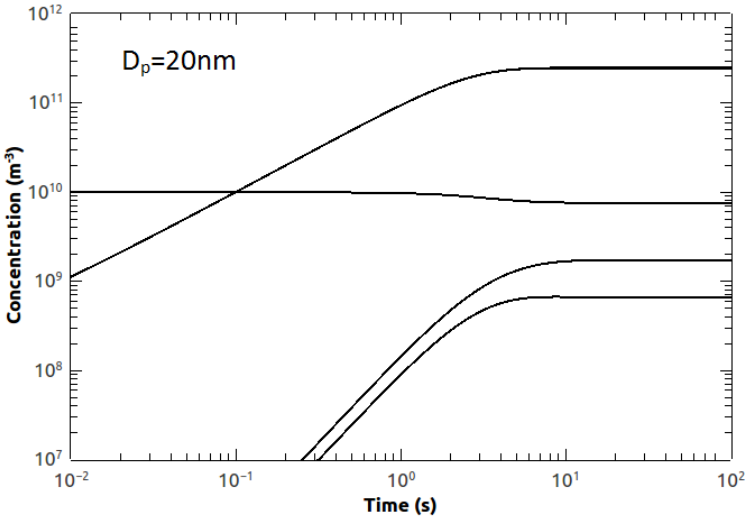

(a) 1D CFD

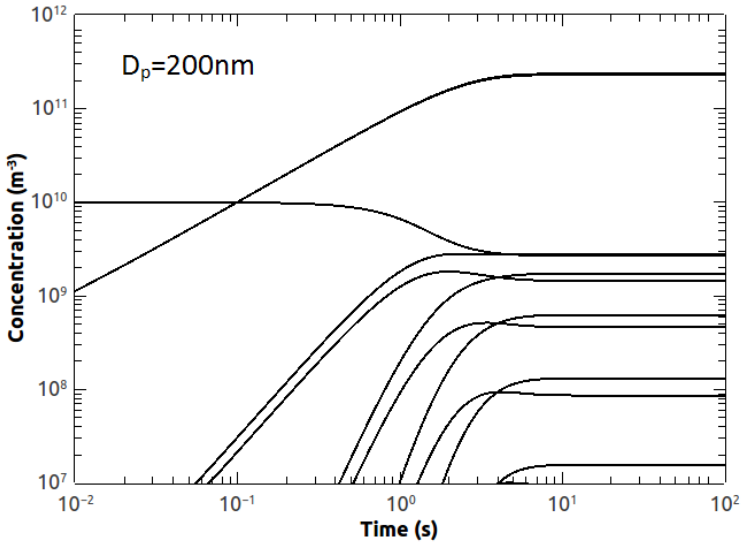

(b) 1D CFD

Fig. A.4 Asymmetric diffusion charging of particles of diameter for ionisation rate 10^5 ion pairs cm^{-1} s^{-1}. Photoionisation is turned off in this case. Results match Hoppel and Frick [128].

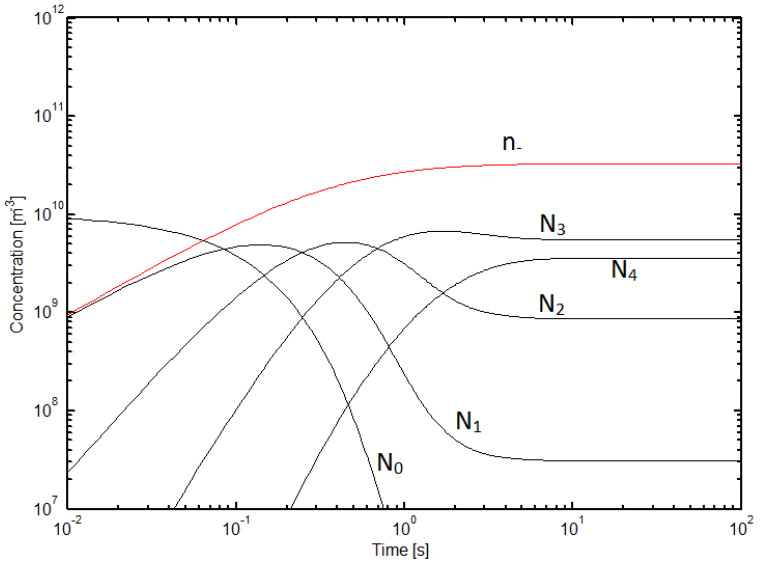

(a) 0D numerical

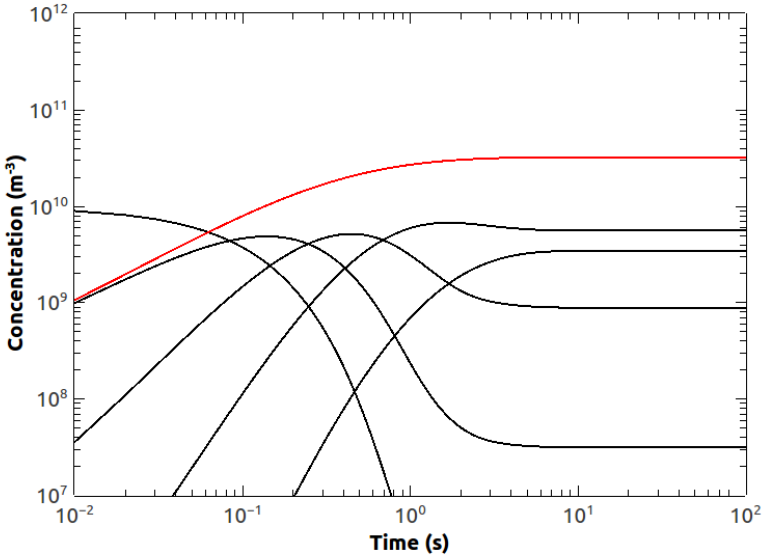

(b) 1D CFD

Fig. A.5 Photoionisation and recombination of particles (d = 10 nm).